

Cite this: DOI:00.0000/xxxxxxxxxx

Received Date
Accepted Date

DOI:00.0000/xxxxxxxxxx

Controlling Li^+ transport in ionic liquid electrolytes through salt content and anion asymmetry: A mechanistic understanding gained from molecular dynamics simulations[†]

Alina Wettstein,^a Diddo Diddens,^b and Andreas Heuer^{a,b}

In this work, we report the results from molecular dynamics simulations of lithium salt-ionic liquid electrolytes (ILEs) based either on the symmetric bis[(trifluoromethyl)sulfonyl]imide (TFSI⁻) anion or its asymmetric analog 2,2,2-(trifluoromethyl)sulfonyl-N-cyanoamide (TFSAM⁻). Relating lithium's coordination environment to anion mean residence times and diffusion constants confirms the remarkable transport behaviour of the TFSAM⁻-based ILEs that has been observed in recent experiments: For increased salt doping, the lithium ions must compete for the more attractive cyano over oxygen coordination and a fragmented landscape of solvation geometries emerges, in which lithium appears to be less strongly bound. We present a novel, yet statistically straightforward methodology to quantify the extent to which lithium and its solvation shell are dynamically coupled. By means of a Lithium Coupling Factor (LCF) we demonstrate that the shell anions do not constitute a stable lithium vehicle, which suggests for this electrolyte material the commonly termed "vehicular" lithium transport mechanism could be more aptly pictured as a correlated, flow-like motion of lithium and its neighbourhood. Our analysis elucidates two separate causes why lithium and shell dynamics progressively decouple with higher salt content: On the one hand, an increased sharing of anions between lithium limits the achievable LCF of individual lithium-anion pairs. On the other hand, weaker binding configurations naturally entail a lower dynamic stability of the lithium-anion complex, which is particularly relevant for the TFSAM⁻-containing ILEs.

1 Introduction

Ionic liquid (IL) based electrolytes have emerged as a promising option to replace the state-of-the-art liquid electrolytes relying on organic solvents¹⁻³. Offering a safer energy storage device due to increasing thermal and electrochemical stability as well as a marginal volatility and risk of flammability⁴⁻⁹, ILs are considered as a potentially tailorable material that allows a functional electrolyte design¹⁰. However, these key benefits trade-off against a rather poor charge transport performance that manifests in a low conductivity and transference number^{3,11}. One strategy to prevent such ionic systems from crystallizing at ambient temperatures lies in the implementation of asymmetric anions¹²⁻¹⁴. This approach has been pursued

experimentally, for example, on the basis of the well-known TFSI⁻ (bis[(trifluoromethyl)sulfonyl]imide) anion via replacement of the trifluoromethylsulfonyl group by a cyano amide moiety, yielding the TFSI-DCA (dicyanamide) hybrid TFSAM⁻ anion (2,2,2-(trifluoromethyl)sulfonyl-N-cyanoamide)¹⁵. The asymmetric substitution is found to improve indeed the liquid range with respect to temperature of the binary IL as well as its conductivity¹⁶. Considering the strong Coulombic interactions between the exclusively ionic constituents in IL/lithium salt electrolytes an increasing lithium salt content is generally associated with an increasing viscosity and thus a considerable reduction of the Li-ion mobility. Surprisingly, superconcentrated "IL-in-salt" electrolytes¹⁷, for which the lithium salt content outweighs that of the IL, have shown even enhanced physicochemical properties as well as improved transport kinetics in terms of the lithium transference number^{7,8,17,18}. A very recent experimental study by Nürnberg et al.¹⁹ combined these two concepts of anion asymmetry and high lithium doping for LiTFSAM_x/Pyr₁₄TFSAM_{1-x} mixtures and checked it against the symmetric anion analogue TFSI⁻. Based on an increasing ratio of the diffusion coefficients

^a Institut für physikalische Chemie, Westfälische Wilhelms-Universität Münster, Corrensstraße 28/30, D-48149 Münster, Germany. Fax: +49 (0)251 83 29159; Tel: +49 (0)251 83 29177; E-mail: andheuer@uni-muenster.de

^b Institut für Energie- und Klimaforschung, Ionics in Energy Storage, Helmholtz Institut Münster, Forschungszentrum Jülich, Corrensstraße 46, 48149 Münster, Germany.

[†] Electronic Supplementary Information (ESI) available

$D_{\text{Li}^+}/D_{\text{anion}^-}$ and Li-ion mobility overtaking that of the anion at elevated salt content, they concluded that the net mode of transport changes from vehicular to structural Li-ion diffusion. The decoupling of Li^+ from anion dynamics was found to be significantly more pronounced for the asymmetric TFSAM⁻ containing electrolytes and related to dramatic changes in the Li^+ coordination environment.

Inspired by the results by Nürnberg et al., which paint an intricate picture of the transforming Li^+ solvation sphere and the resulting changes in transport mechanics, we investigate these systems, *i.e.*, $\text{LiTFSI}_x/\text{Pyr}_{14}\text{TFSI}_{1-x}$ and $\text{LiTFSAM}_x/\text{Pyr}_{14}\text{TFSAM}_{1-x}$ mixtures for $x = 0.0-0.7$, by means of all-atomistic molecular dynamics (MD) simulations.

First, we study how the Li-ion coordination numbers are affected by salt content as well as choice of the asymmetric anion. Second, we analyse the transport dynamics via the standard parameters of diffusion coefficients and residence times between Li^+ and anion. In accordance with the experimental results, we observe concomitant with profound changes of the solvation environment a particular enhancement of the Li-ion mobility in the TFSAM⁻-based mixtures. The focus of this manuscript is a thorough characterisation of the underlying transport mechanics via the Lithium Coupling Factor (LCF) λ that measures the dynamic collectivity of Li^+ and its solvating anions. Our findings strongly suggest that the generally proposed "vehicular" concept is a deceptive description of the joint motion of a Li^+ -shell-complex and urge to be mindful of the fluid nature of ionic liquid electrolytes. Based on the observable λ , we conclude that no fundamental change of transport mechanism occurs with increasing salt concentrations but rather that incorporation of anions in more than one Li^+ solvation environment lowers the dynamic coupling of individual Li^+ -anion pairs. Comparison of the LCFs with TFSI⁻ to TFSAM⁻ shows the power of a tailored anion design where disparate binding sites effectuate low dynamic stabilities of Li-ion and its neighbourhood.

2 Simulation details

The MD simulations were conducted with the software package GROMACS (version 2018.8)²⁰⁻²³. All atomic interactions were modelled according to the widely recognised OPLS-AA-derived CL&P force field, which is developed and maintained by Canongia Lopes and Pádua particularly for the study of ionic liquids²⁴⁻²⁸. To account for polarization effects in a mean-field sense, all partial charges in the system were scaled down by a factor 0.8 according to prevalent practice²⁹⁻³³. Motivated by the experimental study of Nürnberg et al., our study of $\text{LiTFSI}_x/\text{Pyr}_{14}\text{TFSI}_{1-x}$ and $\text{LiTFSAM}_x/\text{Pyr}_{14}\text{TFSAM}_{1-x}$ electrolytes covers the lithium salt fractions $x = [\text{Li}^+]/[\text{anion}^-] = 0.0-0.7$. Since a change of the Li^+ transport mechanism is speculated to occur at $x \approx 0.5-0.65$, this transition regime is sampled in more detail with $x = 0.525, 0.5, 0.575$ and 0.6 . All systems contain in total 1000 ion pairs, *i.e.*, 1000 anions and the according number of Li^+ and Pyr_{14}^+ cations to meet the respective salt concentration. The production runs, which were used for data acquisition, are each 400 ns long and are carried out in the NPT-ensemble using a Nosé-Hoover thermo-

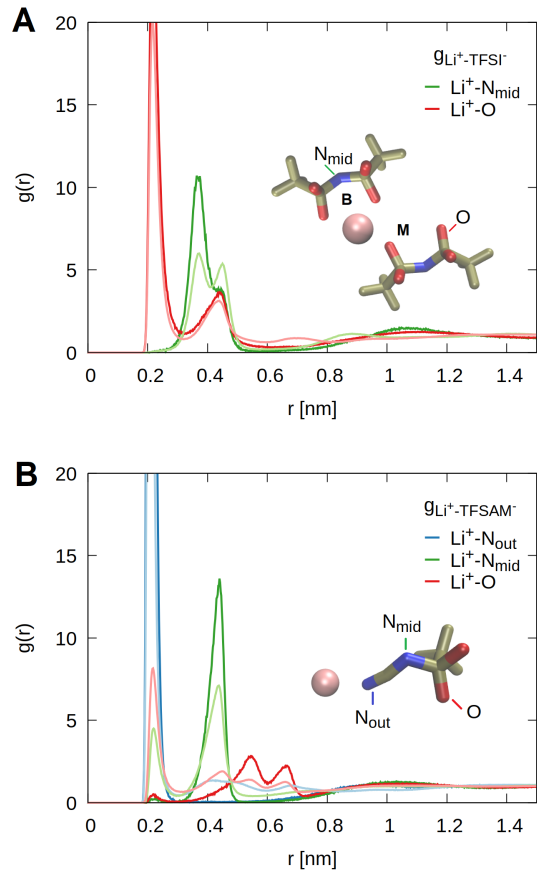


Fig. 1 Radial distribution functions $g_{\text{Li}^+-X}(r)$ between Li-ions and nitrogen / oxygen binding sites provided by TFSI⁻ (top) and TFSAM⁻ (bottom) for lithium salt fractions $x = 0.05$ (deep color) and $x = 0.5$ (light color). The schematic snapshots illustrate the possible monodentate (M) and bidentate (B) coordination of TFSI⁻ as well as the preferred monodentate TFSAM⁻ coordination.

stat³⁴⁻³⁶ to maintain the temperature at 400 K and a Parrinello-Rahman barostat³⁷ to couple the system to atmospheric pressure. The details on the system generation, equilibration procedure and overall simulation protocol are provided in the Supplementary Information section A[†].

3 Lithium coordination environment

3.1 Radial distribution functions

We study the lithium solvation structures via radial distribution functions g_{Li^+-X} (RDF) between the Li-ions and the distinct atomic species by means of which the anions form the coordination bonds. Figure 1A depicts the arrangement of O_{TFSI^-} (red) and $\text{N}_{\text{mid,TFSI}^-}$ (green) atoms around Li^+ exemplary for low and high lithium salt contents. In agreement with other experimental and theoretical studies, we find that O_{TFSI^-} accounts for the primary coordination environment with the nearest peak at 2.1 Å. The double peak structure of $g_{\text{Li}^+-\text{N}_{\text{mid,TFSI}^-}}$ between 3 and 5 Å indicates two types of $\text{Li}^+ - \text{TFSI}^-$ coordination geometries. The nearest peak can be attributed to a bidentate binding, whereas the second peak corresponds to a monodentate contact via one O_{TFSI^-} only^{14,19,38-41}. Our findings are in excellent

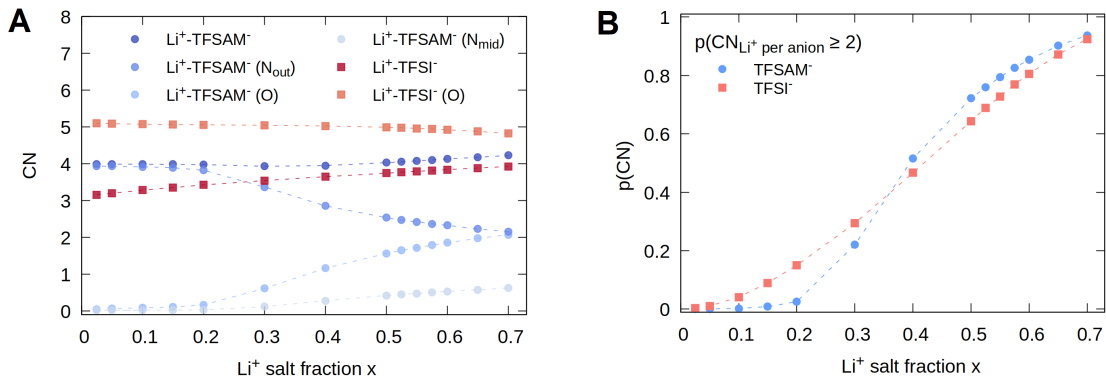


Fig. 2 Left: Coordination numbers CN of Li-ions via TFSI⁻/TFSAM⁻, including resolution regarding the particular atomic binding sites provided by the respective anion. Right: Probability distribution $p(\text{CN}_{\text{Li}^+ \text{ per anion}} \geq 2)$ of at least two Li⁺ neighbours to a single TFSI⁻/TFSAM⁻ as a function of lithium salt content x .

agreement with simulation studies³⁹ on LiTFSI _{x} /Pyr₁₃TFSI_{1- x} ($x = 0.16$) mixtures employing the most recent parametrization of the APPLE&P polarizable force field as well as a combined experimental and MD investigation⁴² of closely related electrolytes LiTFSI _{x} /BMMITFSI_{1- x} ($x = 0.24$ and 0.38). We conclude from the changing relative peak heights of $g_{\text{Li}^+ - \text{N}_{\text{mid}, \text{TFSI}^-}}$ that an increasing lithium salt concentration significantly alters the populations of bidentate and monodentate TFSI⁻ orientation in favor of the latter⁴¹⁻⁴⁴.

The TFSAM⁻ anion can coordinate to Li⁺ additionally via the cyano-group, *i.e.*, $\text{N}_{\text{out}, \text{TFSAM}^-}$ (blue). Figure 1B demonstrates that at low salt concentration Li⁺ binds almost exclusively via $\text{N}_{\text{out}, \text{TFSAM}^-}$ and vanishingly few direct $\text{O}_{\text{TFSAM}^-}$ contacts are made. From an electrostatic and steric point of view, $\text{N}_{\text{out}, \text{TFSAM}^-}$ constitutes the more attractive binding site because it carries the most negative partial charge ($q_{\text{N}_{\text{out}, \text{TFSAM}^-}} = -0.76e$, $q_{\text{N}_{\text{mid}, \text{TFSAM}^-}} = -0.71e$, $q_{\text{O}_{\text{TFSAM}^-}} = -0.53e$, $q_{\text{F}_{\text{TFSAM}^-}} = -0.16e$)²⁴ and is easily accessible for coordination. This bias in favor of Li⁺-cyano coordination has been confirmed recently by Raman measurements¹⁹ as well as observed in a Raman/MD study of a lithium salt-IL mixture containing both DCA and TFSI⁻ anions³³. For increasing salt content, we find a dramatic distortion of the initially uniform Li⁺ - $\text{N}_{\text{out}, \text{TFSAM}^-}$ environment when TFSAM⁻ additionally engages in a direct $\text{O}_{\text{TFSAM}^-}$ and $\text{N}_{\text{mid}, \text{TFSAM}^-}$ binding to Li⁺.

3.2 Coordination numbers

Since $g_{\text{Li}^+ - X}(r)$ measures the probability to find the atomic species X within a distance r away from Li⁺, the first minimum position can be employed as a structural criterion for present Li⁺ - X binding. Coordination numbers $\text{CN}_{\text{Li}^+ - X}$ are determined accordingly from integrating the respective RDF up to this cutoff distance R

$$\text{CN}_{\text{Li}^+ - X} = \rho_{X, \infty} \int_0^R 4\pi r'^2 g_{\text{Li}^+ - X}(r') dr'. \quad (1)$$

By explicit counting of the binding anions, which individually may provide Li⁺ coordination via multiple X , we further obtain a distribution of the molecular $\text{CN}_{\text{Li}^+ - \text{anion}}$. Figure 2A depicts

$\text{CN}_{\text{Li}^+ - X}$ for both electrolyte compositions as a function of salt concentration.

For the TFSI⁻ containing mixtures, we observe that the absolute number of O_{TFSI^-} contributing to the primary Li⁺ environment is barely sensitive to salt content. However, as already deduced from the inverting coordination geometry, the actual number of TFSI⁻ anions affording such a solvation shell increases with increasing salt content. While five O_{TFSI^-} are initially supplied by on average three TFSI⁻ anions, the absolute $\text{CN}_{\text{Li}^+ - \text{TFSI}^-}$ accumulates to four at the highest concentration. Figure 3 (top) shows snapshots of the Li⁺ coordination complexes depicting the coexistence of monodentate and bidentate binding geometries. Analysis of the distributions of Li⁺ - TFSI⁻ - coordination numbers that make up for the average $\text{CN}_{\text{Li}^+ - \text{TFSI}^-}(x)$ gives evidence of a non-uniform coordination landscape with contributions from Li⁺ (TFSI⁻)₃, Li⁺ (TFSI⁻)₄ and even Li⁺ (TFSI⁻)₅ complexation at elevated salt content as shown in Figure S3[†].

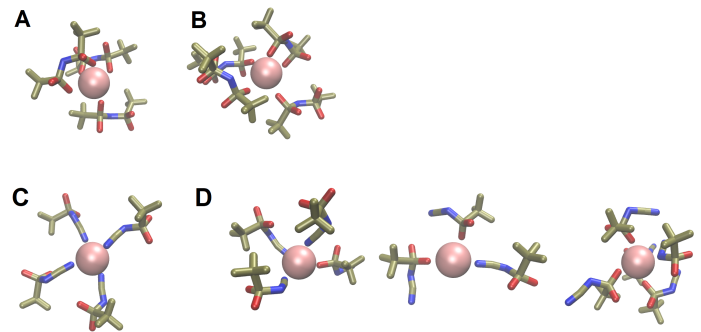


Fig. 3 Examples for Li-ion (pink) solvation shells provided by TFSI⁻ (top) and TFSAM⁻ (bottom) anions for lithium salt fractions of $x = 0.1$ (A,C) or $x = 0.5$ (B,D). Oxygen atoms are displayed in red and nitrogen atoms in blue.

For the low concentration TFSAM⁻ based electrolytes, Li⁺ is exclusively solvated by four $\text{N}_{\text{out}, \text{TFSAM}^-}$ which are naturally supplied by four anions as shown in Figure 2A and illustrated by a snapshot in Figure 3C. In accordance with recent Raman measurements by Nürnberg et al.¹⁹ our simulations indicate no pri-

primary coordination via O_{TFSAM^-} for sufficient $N_{\text{out,TFSAM}^-}$ supply. However, when the ratio of $n_{\text{Li}^+} : n_{\text{TFSAM}^-}$ exceeds 1:4, $N_{\text{out,TFSAM}^-}$ can no longer provide solely for a saturated solvation shell. We even identify direct binding to $N_{\text{mid,TFSAM}^-}$, which is yet a rare coordination motif. Overall, the Li^+ environment becomes increasingly heterogeneous both in terms of the atomic species mediating the binding and the net number of TFSAM⁻ molecules constituting the primary shell as shown in Figure S3[†]. A random selection of Li^+ environments is displayed in Figure 3D.

As a final characterisation of the Li^+ shell structure, we adopt the anion's perspective and measure the distribution of Li^+ neighbours around a single anion. Figure 2B depicts that Li^+ maintains a self-contained TFSAM⁻ solvation environment as long as the preferred $N_{\text{out,TFSAM}^-}$ binding sites are not saturated. In the low concentrated TFSI⁻-based mixtures, however, a steadily growing amount of TFSI⁻ bridges at least two Li-ions even though an excess of lithium-free anions is available for coordination. This agrees well with findings from previous MD studies^{43,45} where lithium aggregates occurred at salt fractions $x \geq 0.1$. In the regime of high concentrations, we observe that the inclination of TFSAM⁻ to lithium clustering rapidly overtakes that of TFSI⁻.

4 Ion transport properties

4.1 Diffusion constants

To discuss the Li^+ transport characteristics, we first calculated the self-diffusion coefficients of each ionic species according to the Einstein relation:

$$D_i = \lim_{t \rightarrow \infty} \frac{\langle (\bar{r}_i(t) - \bar{r}_i(0))^2 \rangle}{6t}, \quad (2)$$

where $\bar{r}_i(t)$ denotes the position of the ion belonging to species i and $\langle \dots \rangle$ indicates the ensemble average. The results are shown in Figure 4A and B for both electrolyte mixtures over the entire concentration range under study. As expected, increasing addition of lithium salt causes a slowing down of the overall dynamics, which can be attributed to an increasing electrolyte viscosity^{29,43,44}. For moderate salt concentrations up to $x = 0.3$ the diffusivities rank in both systems as $[\text{cation}]_{\text{IL}}^+ > [\text{anion}]^- > [\text{Li}]^+$, which is in agreement with MD studies investigating the TFSI⁻-based mixture as well as experiments^{19,39,43}. Whereas for the TFSI⁻-containing electrolytes the dynamics slow down continuously, D_{Li^+} and D_{TFSAM^-} achieve a plateau between $x = 0.3 - 0.5$. The bulk dynamics resume their decline, but the Li^+ diffusion overtakes that of TFSAM⁻. Similar observations have been made by Nürnberg et al.¹⁹, who reported at elevated salt content a remarkable discontinuance of till then slowing dynamics. To gain insights on the dominant mode of Li^+ transport, which may change over the broad concentration spectrum, Nürnberg et al. considered the dependence of $D_{\text{Li}^+}/D_{\text{anion}}$ on salt content as plotted in Figure 4C. Our results confirm the experimental observation that for the TFSI⁻-based electrolytes the diffusion ratio is barely sensitive on increasing lithium salt concentrations up to $x = 0.5$ with a following upward trend towards equally fast Li^+ and TFSI⁻ diffusion. In the TFSAM⁻-mixtures, on the other hand, the Li-ions display a steady acceleration relative to TFSAM⁻

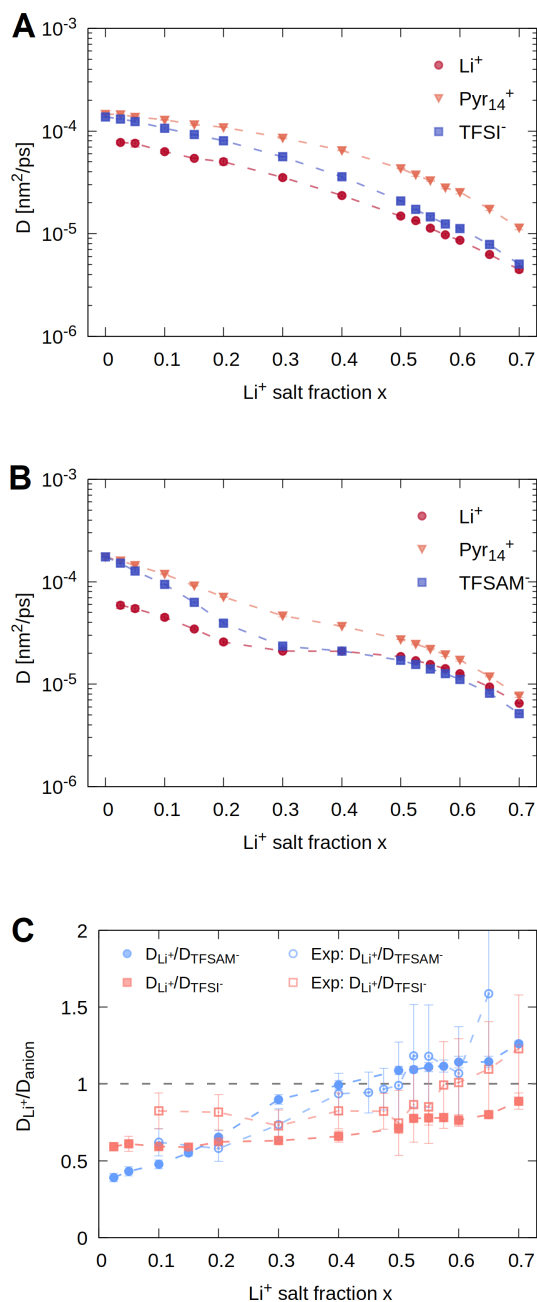


Fig. 4 Top and center: Self diffusion coefficients of all ionic species as a function of lithium salt content x . The self diffusion coefficients for the TFSI⁻ system at $x = 0.15$ match results from recent polarizable force field simulations employing a Pyr_{13}^+ cation within a factor of two³⁹. Bottom: Ratio of Li^+ and anion self diffusion coefficients as a function of lithium salt content. The full symbols show the data measured in this work and are compared to the experimental results from Nürnberg et al.¹⁹, which are depicted by the open symbols. Reprinted (adapted) with permission from P. Nürnberg, E. I. Lozinskaya, A. S. Shaplov and M. Schönhoff, *The Journal of Physical Chemistry B*, 2020, **124**, 861–870. Copyright 2021 American Chemical Society.

for increasing x with D_{Li^+} faster than D_{TFSAM^-} for $x > 0.4$. Nürnberg and coworkers put forward the hypothesis that the structural changes of the immediate Li^+ environment induce a transition from a predominantly vehicular diffusion, *i.e.*, a strongly coupled

motion of Li^+ and its primary solvation shell, to a structural diffusion mechanism where Li^+ performs hopping-like events between its neighbouring anions. The fact that the turning point of the dynamic changes coincides remarkably with the onset of these structural rearrangements is supportive of this interpretation.

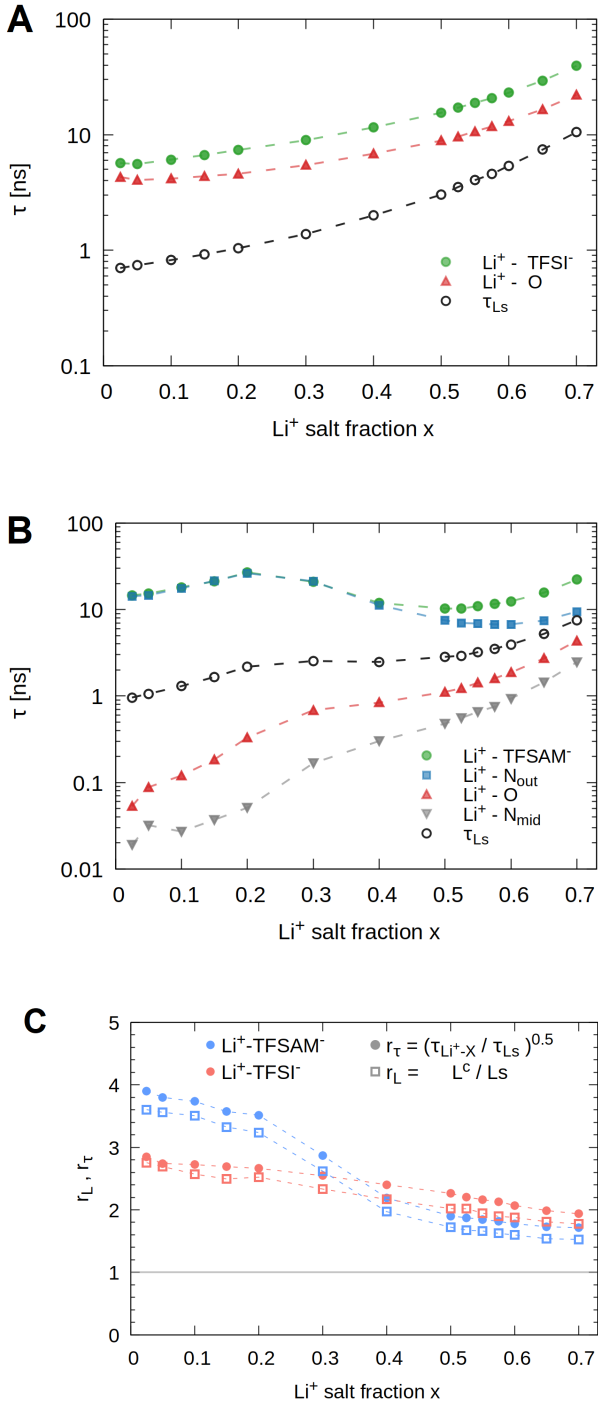


Fig. 5 Top and center: Mean residence times τ of Li^+ at various atomic binding sites provided by TFSI⁻ (top) or TFSAM⁻ (center) as a function of lithium salt content x . We note that $\tau_{\text{Li}^+-\text{TFSI}^-}$ for $x=0.15$ matches results from recent polarizable force field - simulations employing a Pyr₁₃ cation within a factor of two³⁹. Bottom: Mechanistic interpretation of mean residence times $\tau_{\text{Li}^+-\text{TFSI}^-/\text{TFSAM}^-}$ and Li^+ solvation sphere size L_s in terms of the ratio $r_\tau = \sqrt{\tau_{\text{Li}^+-\text{anion}}/\tau_{\text{LS}}}$ as well as $r_L = L^c/L_s$.

4.2 Mean residence times

One can only surmise the extent of correlated transport from the self-diffusion coefficients, which are ultimately averaged over all ionic species regardless of their binding status, and therefore, strictly speaking, do not provide specific information on the pairwise motion of Li^+ and anion. A more precise picture of the Li^+ solvation dynamics can be obtained from the mean residence times τ_{Li^+-X} , *i.e.*, the average time a Li-ion is attached to species X which is computed from the residence time autocorrelation function (see Supplementary Information section D[†]). The analysis can be performed for all atomic species to which Li^+ is inclined to bind, *e.g.*, $\text{O}_{\text{TFSI}^-/\text{TFSAM}^-}$ or $\text{N}_{\text{out,TFSAM}^-}$. We track the $\text{Li}^+ - \text{N}_{\text{mid}}$ bond to measure the average time $\tau_{\text{Li}^+-\text{TFSI}^-/\text{TFSAM}^-}$ that Li^+ spends in the direct vicinity of a distinct anion using the second minimum position in $g_{\text{Li}^+-\text{N}_{\text{mid}}}$ as a distance cutoff. It is clear from Figure 1 that all possible coordination geometries occurring at the respective salt concentration such as mono- and bidentate TFSI⁻ binding or direct binding via $\text{O}_{\text{TFSAM}^-}$, $\text{N}_{\text{out,TFSAM}^-}$ or $\text{N}_{\text{mid,TFSAM}^-}$ are thereby contained. Figure 5A shows that the exchange of the original TFSI⁻ solvation environment slows down with increased salt content, which can be deduced from the increasing Li^+ binding time to a distinct O_{TFSI^-} atom or a distinct TFSI⁻ molecule. Most commonly, slowing dynamics in terms of diffusivity in such ionic systems are found to correlate directly with increasing ion pair lifetimes^{43,46}. Surprisingly, we observe a very unique binding time behaviour for the TFSAM⁻-based electrolytes which is displayed in Figure 5B. The structural analysis has demonstrated that at low salt content the $\text{Li}^+ - \text{TFSAM}^-$ binding is solely mediated via $\text{N}_{\text{out,TFSAM}^-}$ but no direct contacts to $\text{O}_{\text{TFSAM}^-}$ or $\text{N}_{\text{mid,TFSAM}^-}$ atoms are made. Accordingly, we find corresponding mean residence times to be negligibly short-lived and up to two orders in magnitude shorter than $\tau_{\text{Li}^+-\text{N}_{\text{out,TFSAM}^-}}$. All residence times increase with increasing salt content as far as $x \leq 0.2$ when $\tau_{\text{Li}^+-\text{TFSAM}^-}$ and $\tau_{\text{Li}^+-\text{N}_{\text{out,TFSAM}^-}}$ exhibit a turning point. The average time Li^+ spends in the neighbourhood of TFSAM⁻ is reduced significantly, which suggests that Li^+ is bound in weaker configurations. Concomitant with the structural rearrangement of the primary solvation shell, $\tau_{\text{Li}^+-\text{O}/\text{N}_{\text{mid}}/\text{N}_{\text{out}}}$ approach the same time scale and thus mirror a competition of these binding sites.

5 Transport mechanism

Current literature assesses the molecular-scale mechanism of lithium transport in dimensions of either a "vehicular" or "structural" type of diffusion^{29,33,38,39,41,43,44,47,48}. The terminology is apparently borrowed from the mechanistic description of proton conduction where the conditions are somewhat similar. Due to its large charge density a proton is liable to be absorbed by its environment. If it is attached to a mobile host molecule, the proton diffusion is guided by this vehicular entity (vehicle mechanism)⁴⁹⁻⁵². This transport concept contrasts with a repeated jumping along electronegative moieties that are provided by a surrounding parent structure (hopping / Grotthus mechanism)^{49,51,53}. In the context of lithium transport, this vehicular concept is often equated with a strongly correlated motion

of Li^+ and its shell, where the latter may be constituted by several coordinating molecules. The aspect of structural diffusion is less clearly defined but commonly describes the scenario where Li^+ mobility benefits from a frequent exchange of the coordinating molecules, possibly by means of such Grotthus-like hopping events between coordination spheres.^{19,29,30,43}

Putting theory into practice, the classification of the dominating mechanism is usually made by balancing a local time or length scale, which is set by a single Li^+ -ligand pair, against those established by the diffusivities of Li^+ and ligand. In a variety of recent simulation studies on lithium salt-IL electrolytes, the importance of the vehicular mechanism is estimated by comparing $\text{MSD}_{\text{Li}^+}(\tau_{\text{Li}^+-X})$ against the size of the solvating anion X .^{38,41,43,54} Self and coworkers²⁹ systematically studied the Li^+ transport process in super-concentrated lithium salt propylene carbonate (PC) electrolytes, which differ from the IL based electrolytes investigated in this work insofar as Li^+ solvation is achieved not only through anions but also neutral PC molecules. To conclude on the predominant Li^+ transport mechanism in a spectrum from vehicular to structural diffusion, the authors proposed an intuitive comparison of two length scales. The characteristic length scale

$$L_{\text{Li}^+-X}^c = \sqrt{6D_{\text{Li}^+}\tau_{\text{Li}^+-X}} \quad (3)$$

measures the average distance that Li^+ and ligand X diffuse together and is evaluated against the size of the X -based solvation shell L_s . One proposed practical, yet contestable, estimator for L_s is the position of the first minimum of $g_{\text{Li}^+-X_{\text{com}}}$. We slightly extend this scheme by switching to a temporal perspective and relate the local length scale L_s to a characteristic "self diffusion time" τ_{L_s} according to $\text{MSD}_{\text{Li}^+}(\tau_{L_s}) = L_s^2$, *i.e.*, the time Li^+ requires to cover the area L_s^2 . Please note that we will use τ_{L_s} , whose concentrations dependence is additionally shown in Figures 5A and B, to scale the time dependence of correlative properties later. By analogy to Self et al.²⁹, the transport criterion can be formulated as

$$r_L \stackrel{\text{def}}{=} \frac{L^c}{L_s} \simeq r_\tau \stackrel{\text{def}}{=} \sqrt{\frac{\tau_{\text{Li}^+-X}}{\tau_{L_s}}} \quad \begin{cases} > 1 & \text{vehicular} \\ < 1 & \text{structural.} \end{cases} \quad (4)$$

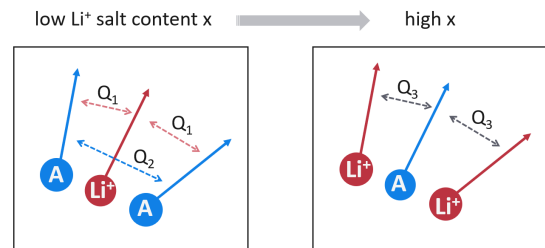
Figure 5C shows that an increasing salt content effectuates a drop in the net contribution of the vehicular mode in both electrolyte mixtures. This trend is reported in previous studies^{41,43} and it is reasoned that a relative mobility improvement of alkali metal ions may be causally linked to a concentration induced breakup of their solvation vehicle^{19,44,55}. This hypothesis of a structurally conditioned change in transport mechanism is supported by the sudden and steep decline of $r_{L/\tau}$ for the TFSAM⁻ based mixtures. When exceeding the threshold concentration $x = 0.3$, for which the primary Li^+ solvation sphere is dramatically reconfigured, the degree of collective Li^+ -TFSAM⁻ motion falls abruptly below the TFSI⁻ analogue. As already discussed on basis of the absolute mean residence times, the incipient coordination by less attractive binding sites provided by TFSAM⁻ may imply an overall lower binding energy of Li^+ to its solvation cage, which therefore pro-

motes a more efficient renewal of the latter.

Overall, the two common approaches of comparing either characteristic length/time scales or the ratio of self-diffusion coefficients attest to a decreasingly collective nature of the Li^+ -solvation complex, although their information content is quite different. On the one hand, we learn from the $r_{L/\tau}$ behaviour that the extent to which Li^+ travels with its shell decreases steadily with increasing salt content. However, a change of transport mechanism towards structural diffusion can only be deduced when $r_{L/\tau}$ falls below 1 and, naturally, undershooting this threshold is very sensitive to how one specifies L_s . The explanatory power of relative diffusivities, on the other hand, is limited to $D_{\text{Li}^+}/D_{\text{anion}} > 1$. In the highly concentrated regime Li^+ diffuses faster than the TFSAM⁻ shell anions, which is indeed not compatible with the vehicular picture of a dynamically stable Li^+ shell and strong evidence of structural Li^+ diffusion. Unlike for $r_{L/\tau}$, the trend of increasing $D_{\text{Li}^+}/D_{\text{anion}} \leq 1$ is open to different interpretations. Apart from the evolution of a new transport mechanism, a decreasing D_{anion} could effectuate an increasing diffusivity ratio as well. Referring to the discussion of coordination numbers, a higher lithium salt content correlates with a smaller fraction of Li^+ -uncoordinated, *i.e.*, 'free', anions so that D_{anion} is slowed down with more anions being integrated in retarding Li^+ solvation shells. In fact, $D_{\text{Li}^+}/D_{\text{anion}} = 1$ taken alone could be the signature of perfectly vehicular Li^+ -shell dynamics.

A key drawback of these two analysis schemes is that both spatial and temporal resolution of how the Li^+ -shell disintegrates are not accounted for. To elucidate the transport mechanism in new and complementary detail, we pose three key questions about the Li^+ -shell dynamics:

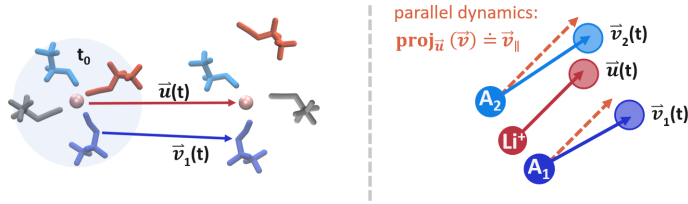
- Q₁ How do anion dynamics couple to the motion of the lithium ion?
- Q₂ Do the dynamics of anions, which are coordinated to the same Li^+ , exhibit extra positive correlations among themselves and thus stability, as implied by the picture of a vehicular transport mechanism?
- Q₃ How do anion dynamics respond to multiple lithium coordination at high salt fractions?



5.1 Collectivity of Li^+ -shell dynamics and Lithium-Coupling Factor λ

To answer these questions, we propose a very simple but systematic characterisation of the (un)coupled dynamics of Li^+ and its anionic neighbourhood. The underlying idea is sketched

in Scheme 1. We set up an anion neighbour list for every Li-ion based on the procedure that is employed to determine $\tau_{\text{Li}^+ - \text{TFSI}^- / \text{TFSAM}^-}$.



Scheme 1 Left: Sketch of a Li^+ -solvation complex which is defined at a reference time t_0 and tracked over time regarding the spatial displacements. Right: To measure the translation $\vec{v}_{\parallel j}$ (dashed orange) of the anion in direction of the Li^+ -ion to which it is initially bound, the anion displacement $\vec{v}_j(t)$ (blue) is projected on the respective Li^+ displacement $\vec{u}(t)$ (red).

The neighbour list comprises the identities j and positions $\vec{r}_j^i(t_0)$ of the anions binding to the designated Li^+ -ion i at a reference time t_0 . We then track the individual displacements of the Li^+ -ions $\vec{u}_i(t) = (\vec{r}_i(t) - \vec{r}_i(t_0))$ and the denoted anions $\vec{v}_j^i(t) = (\vec{r}_j^i(t) - \vec{r}_j^i(t_0))$ as a function of time. As a starting point for answering question Q₁, we characterise the dynamic collectivity of Li^+ and anion by means of a vector decomposition: we project the anion displacement $\vec{v}_j^i(t)$ on the displacement $\vec{u}_i(t)$ of its Li^+ -ion and compute the distance $v_{j\parallel}^i$ which the anion covered parallel to the Li^+ -ion's direction. From this, we can further deduce the change of position Δv_{\parallel} of the anion relative to Li^+ in that direction:

$$\frac{\vec{u}_i \cdot \vec{v}_j^i}{u_i} = v_{j\parallel}^i \quad \wedge \quad v_{j\parallel}^i - u_i \stackrel{\text{def}}{=} \Delta v_{\parallel}. \quad (5)$$

In the limiting case of a perfectly coupled motion, the relative displacement is conserved and thus $\Delta v_{\parallel} = 0$. Apart from a natural time dependence, *i.e.*, one expects Δv_{\parallel} to scatter increasingly with time as Li^+ and anions become detached, Δv_{\parallel} may also depend on the Li^+ displacement u . It seems plausible that the dynamic collectivity could be impeded increasingly with larger u . To test this assumption, we study the distribution $p(\Delta v_{\parallel})$ for subensembles of Li^+ -ions which covered a specific distance u . For a comparison as intuitive as possible, we choose subensembles of Li^+ -ions whose squared displacement u^2 corresponds to a multiple k of the mean squared displacement $\langle u^2 \rangle$ at time t .

Figure 6 gives an overview of $p(\Delta v_{\parallel})$ as a function of lag time t and Li^+ distance scaling factor k exemplary for the $x = 0.1$ TFSAM^- -based electrolyte. In accordance with the previously assessed indicators of strongly coupled Li^+ -anion-dynamics, *i.e.*, τ_L/τ , the distributions show a large peak that is centred closely at a relative anion- Li^+ distance $\Delta v_{\parallel} \approx 0 \text{ \AA}$. Importantly, one can directly see the disintegration with time. We interpret the developing tail of $p(\Delta v_{\parallel})$ as the superposition of a steadily growing ratio of anions having disengaged from the initial Li^+ solvation shell, whose subsequent dynamics are no longer correlated with the Li^+ reference. However, since the mean residence time $\tau_{\text{Li}^+ - \text{TFSAM}^-} = 18.1 \text{ ns}$ exceeds the longest analyzed lag time t the peak is yet present. To quantify the peak features, *i.e.*, its position μ and variance σ^2 , and thus the dynamic coupling of Li^+ -anion pairs, we empirically fit the distribution by a Gaussian function. To separate the peak from the overlapping signatures of decoupled anions, we adopt a two-step fitting procedure: First, the plain distribution is fitted by a Gaussian which provides us with an educated guess of μ and σ^2 . Then, we refit the distribution but limit the left-hand side of the value range to $-\sigma + \mu \leq \Delta v_{\parallel}$. The final Gaussian fits are

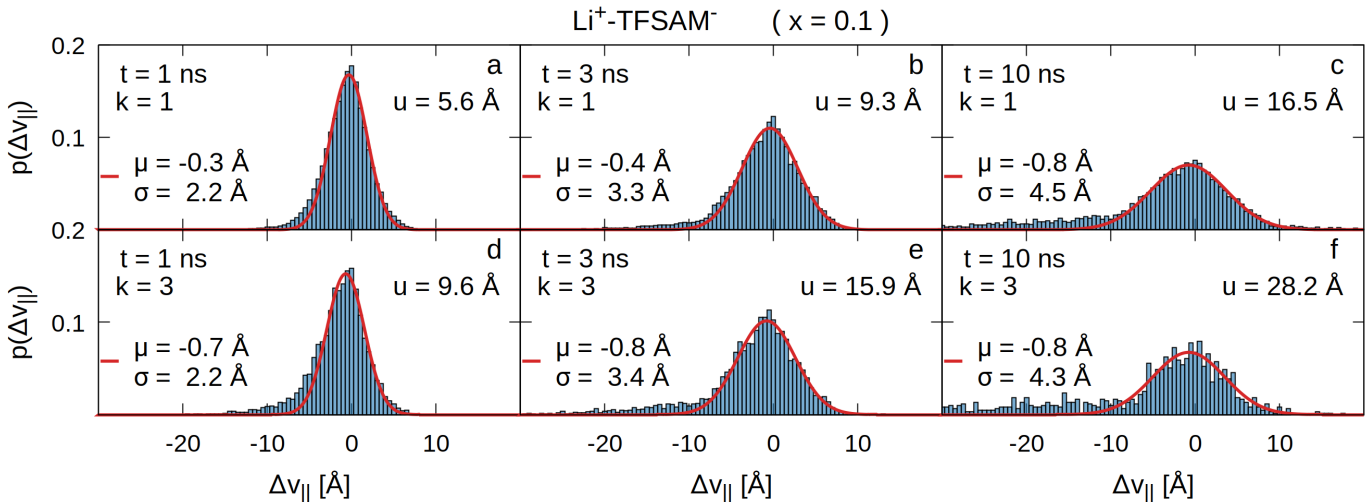


Fig. 6 Exemplary for the TFSAM^- -based mixture at a salt fraction $x = 0.1$: Distributions of the relative distance Δv_{\parallel} between anion and Li^+ , which are bound at a reference time t_0 , in direction of the Li^+ -ion for various subensembles. The upper panel shows the histograms for the subensemble of Li^+ -ions whose squared displacement u^2 matches the Li^+ mean squared displacement $\langle u^2 \rangle$ at the respective lag times $t = 1, 3$ and 10 ns (a, b and c), *i.e.*, $u^2 = k \cdot \langle u^2 \rangle$ and distance scaling factor $k = 1$. The lower panel histograms (d, e and f) belong to the subensemble of Li^+ -ions for which the distance scaling factor $k = 3$. The peaks are fitted by a Gaussian function (red) whose expected value μ and standard deviation σ^2 are given in the legends. A description of the fitting procedure is provided in the Supplementary Information section F[†]. Please note that the histograms are displayed for a bin width of 0.5 \AA for visual reasons but the Gaussian fit is obtained for 0.1 \AA binning.

plotted in red with μ and σ provided in the legend. At fixed lag time t , we find that μ is not only different to zero but also shifted towards an increasing anion-Li⁺ distance for larger k . Interestingly, neither of these two properties is intuitively expected from a vehicular transport concept. Assuming that the bound anions move with lithium as a kinetic entity, reorientations within the shell geometry would effect a maximum possible peak width σ , yet should average to $\mu = 0$ for symmetry reasons. While the peak of coupled dynamics may decrease in height for a decreasing ratio of dynamically preserved Li⁺-anion pairs, its unique signature of $\mu = 0$ and constant σ after fast local equilibration would not depend on u .

We explore the mechanistic background giving rise to this peak behaviour by means of a toy model: A Li⁺-anion pair is simplified to two particles which are coupled by a harmonic interaction. The particles' collective and relative dynamics, *i.e.*, $X = (u + v_{\parallel})/2$ and $\Gamma = (u - v_{\parallel})/2$, are both subjected to Gaussian distributions whose statistical parameters are accessible through our analysis of $p(\Delta v_{\parallel})$. As demonstrated in the Supplementary Information section G[†], this toy model predicts a connection between μ and σ :

$$\mu = -\frac{u}{2} \cdot \frac{\sigma^2}{\langle u^2 \rangle} \quad \text{for } u^2 = k \cdot \langle u^2 \rangle \quad -\frac{\sqrt{k}}{2} \cdot \frac{\sigma^2}{\sqrt{\langle u^2 \rangle}}. \quad (6)$$

The validity of this relationship with regard to the numerical data is tested in Figure 7 and we find that the scaling $\mu \propto \sqrt{k}$ as well as the universal interplay of μ, σ and $\langle u^2 \rangle$ is surprisingly well-fulfilled. From this, we can conclude that the dynamic complexity of a Li⁺-anion pair, and therefore the Li⁺ solvation shell, is approximated remarkably well by a harmonic coupling. Turning towards the time evolution of the peak properties, we

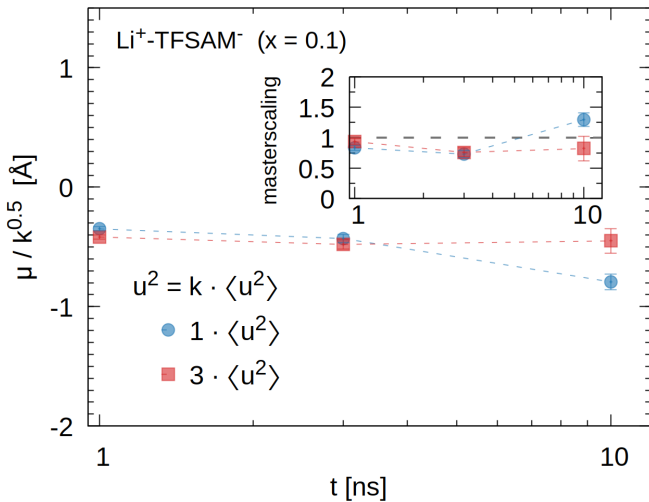
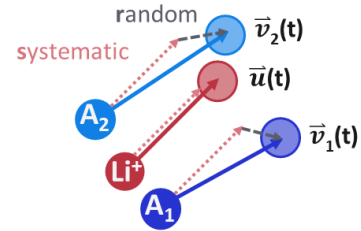


Fig. 7 Exemplary for the TFSAM⁻-based mixture at a salt fraction $x = 0.1$: Peak positions μ of Gaussian fits shown in Figure 6 divided by the square root of the Li⁺ distance scaling factor k . Inset: Masterscaling of the Gaussian peak parameters μ and σ^2 to 1 according to Equation 6 after rearrangement to $1 = -2 \cdot \mu \sqrt{\langle u^2 \rangle} / \sqrt{k} \sigma^2$.

make two observations: Firstly, we find a slight shifting of the peak position and secondly, a significant broadening of the peak over time. While the peak broadening might be partially

attributed to anions exploring the configurational space around Li⁺, the behaviour could also be interpreted qualitatively as a gradual weakening of the effective harmonic Li⁺-shell interaction. Over time, an increasing share of the initially bound anions has escaped the primary Li⁺ neighbourhood as clearly reflected in the steadily growing tail of the distribution. However, since $d \log \sigma^2 / d \log t$ is significantly smaller than 1, *i.e.* subdiffusive, even after detachment these anions will find themselves in a flow field which they share with their previous environment and thus may effectuate a loose yet measurable hydrodynamic coupling to the original Li⁺. Overall, it is remarkable that even when Li⁺ has travelled beyond the next-neighbour distance (see Figure S1[†]), the harmonic coupling in both subensembles, *e.g.*, comparing Figure 6c and f, remains equally strong.

While the residence time autocorrelation (ACF) function (see Equation S2) is a structural measure of the ratio of anions remaining in the Li⁺ solvation shell, we may quantify the percentage of dynamically dissociated shell anions from $\int d\Delta v_{\parallel} (p(\Delta v_{\parallel}) - \mathcal{N}(\mu, \sigma^2)) \doteq p_{\text{lost}}$, *i.e.*, essentially the tail of $p(\Delta v_{\parallel})$. Figure S15[†] shows that p_{lost} increases with time as well as Li⁺ displacement u , and, furthermore, systematically follows the structural decoupling probed by the ACF (see Figure S7[†]) which underscores the relevance of dynamic coupling beyond the primary solvation shell. Please note that an extended data set for both TFSI⁻ and TFSAM⁻-based electrolytes is provided in the Supplementary Information sections F-H[†]. For the sake of brevity, we discussed the common insights exemplary for the $x = 0.1$ TFSAM⁻ mixture.



Scheme 2 In the coordinate frame of a designated Li⁺, the anion displacement \vec{v}_j (blue arrow) is split into a systematic part (dotted pink arrow), which is parallel to the Li⁺ displacement \vec{u} (red arrow), and a random motion (dashed grey arrow). As graphically indicated, the lithium-coupling factor λ , *e.g.*, $\lambda = 0.85$ in this sketch, corresponds to the ratio of arrow lengths of systematic anion and Li⁺ displacement.

Building on the mechanistic understanding of the coupled Li⁺-anion dynamics, we wish to characterise the Li⁺ transport properties in their entirety, providing the foundation for a clear comparison of dynamic collectivity across different electrolytes. With this in mind, we make a conceptual switch from the dynamic coupling of distinct Li⁺-anion pairs to the ensemble of anions and their collective motion $\langle v_{\parallel} \rangle_{u^2}$ in the coordinate frame of Li⁺.

At a fixed time t , we introduce the lithium-coupling factor (LCF) λ which expresses the systematic contribution of the anion displacement $\langle v_{\parallel} \rangle_{u^2, t}$ relative to the Li⁺ displacement u . It may depend on the squared Li⁺ displacement u^2 and on the chosen time scale t . On the most detailed level, we first analyse $\lambda(u^2, t)$ conditioned

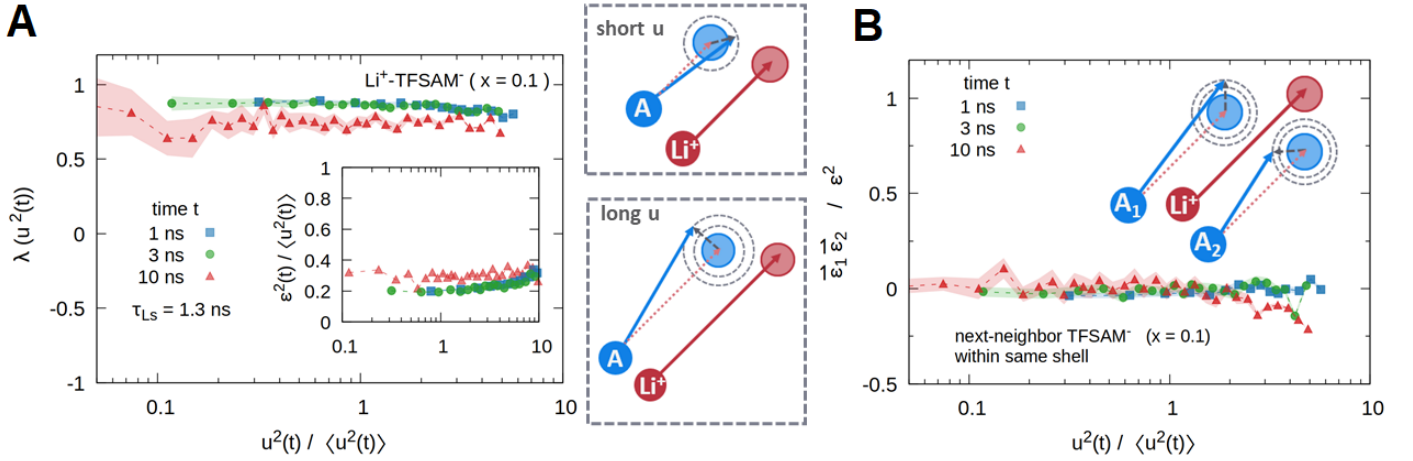


Fig. 8 Exemplary for the TFSAM⁻-based mixture at a salt fraction $x=0.1$: Left: LCF λ as a function of u^2 , which is scaled by the MSD_{Li⁺} $\langle u^2 \rangle$ at the respective lag time t . Inset: Variance ε^2 of the anion displacement relative to Li⁺ trajectory. To allow for a better comparison, ε^2 is scaled by MSD_{Li⁺} as well. Right: Correlation of the random motion of initially adjacent shell anions $\langle \bar{\varepsilon}_1 \cdot \bar{\varepsilon}_2 \rangle / \langle \bar{\varepsilon}^2 \rangle$ as a function of $u^2 / \langle u^2 \rangle$ and the consequential mechanistic picture. Due to rare statistics the fastest 1% of Li⁺ ions are not shown in the plots.

on a specific time lag t as well as the squared lithium displacement u^2 .

In a second step towards a further generalised description, we take the average over all Li⁺-anion pairs regardless of the distance covered by a specific Li⁺, giving rise to $\lambda(t)$:

$$\lambda(u^2, t) = \frac{\langle \bar{u}_i \cdot \bar{v}_j^i \rangle_{u^2, t}}{u^2} = \frac{\langle v_{\parallel} \rangle_{u^2, t}}{u} \quad \wedge \quad \lambda(t) = \frac{\langle \bar{u}_i \cdot \bar{v}_j^i \rangle_t}{\langle \bar{u}^2 \rangle_t}. \quad (7)$$

$\langle \dots \rangle$ denotes the corresponding ensemble average over all Li⁺-anion-pairs ij existing at t_0 . For reasons of simplicity, the time dependence of these observables is not explicitly mentioned in parts. Geometrically speaking, the LCF weighs the average projection of \bar{v} on \bar{u} against the Li⁺ displacement u and thereby expresses the features of Figure 6 through a number. From a physical viewpoint, the LCF behaves like a correlation coefficient: A strictly coupled motion of Li⁺ and its shell anions implies $\lambda \approx 1$ because single leads of either \bar{u} or \bar{v} due to rotational rearrangement within a shell would cancel out over time. When an initially defined neighbourhood disintegrates, the LCF decreases ultimately to zero. As visualised in Scheme 2, we may thus decompose the anion dynamics in the reference frame of Li⁺ into a systematic part (pink) and random motion (grey):

$$\bar{v}_j^i(t) = \lambda(u^2, t) \cdot \bar{u}_i(t) + \bar{\varepsilon}_j^i(u^2, t). \quad (8)$$

Knowing λ , we gain additional information on the anion's motional freedom which is measured by the variance:

$$3 \cdot \varepsilon^2 = \langle \bar{\varepsilon}^2 \rangle_{u^2, t} = \langle \bar{v}^2 \rangle_{u^2, t} - \lambda^2 \langle \bar{u}^2 \rangle_{u^2, t}. \quad (9)$$

Please note that by construction $\langle \bar{u}_i \cdot \bar{\varepsilon}_j^i \rangle = 0$.

In the subsequent analysis we are guided by the initially posed questions 1-3 and examine with increasing generalisation how the dynamic properties of the Li⁺-shell-object depend on Li⁺ displacement, time and salt concentration. For the sake of brevity, the results are discussed for the example of the TFSAM⁻-

containing electrolytes, while the complete data set is provided in the Supplementary Information sections I-M[†].

5.1.1 Displacement dependence $\lambda(u^2)$

Figure 8A shows that regardless of whether Li⁺ covered half or more than five times of MSD_{Li⁺} at the respective lag time t , the average collectivity with its environment remains the same. The finding that λ does hardly depend on u is consistent with the predictions of the harmonic toy model. In the limit of $p_{\text{lost}} = 0$, Equation 7 implies $\lambda \approx 1 + \mu/u$. As discussed for Figure 7, we find $\mu \propto u$ at fixed time t so that consequently $\lambda \approx \text{const.}$ for varying u . The observation of a strong LCF $\lambda < 1$ is thus as a direct consequence of the shifted Gaussian peak position $\mu < 0$. It is remarkable that λ maintains the independence of u even at longer lag times t when a noticeable proportion of the anions has already escaped the Li⁺-shell as discussed for the tails of $p(\Delta v_{\parallel})$ in Figure 6, which substantially effectuate the drop of the average coupling strength. On a qualitative level, we attribute the small decline of λ for large lithium displacements to the concurrently increasing p_{lost} .

As shown in the inset of Figure 8A, the independence of u is approximately true for the random dynamics ε^2 of the anions as well, which increases only slightly when the designated Li⁺ has moved appreciably further. In accordance with the strong LCF, we find that the Li⁺-independent motion is, firstly, small compared to u^2 and, secondly, scales with $\langle u^2(t) \rangle$ which further supports the conceptual extension of coupled transport by flow-like properties. Splitting $\bar{\varepsilon}$ into contributions parallel $\bar{\varepsilon}_{\parallel}$ and orthogonal $\bar{\varepsilon}_{\perp}$ to the Li⁺ path direction \bar{u} , as demonstrated in Figure S19[†], reveals that the anionic fluctuations relative to the Li⁺ trajectory are approximately isotropic with $\bar{\varepsilon}_{\perp}^2 \approx 2 \cdot \bar{\varepsilon}_{\parallel}^2$. The random displacement of the anions can therefore be illustrated schematically by spheres which add to the systematic motion in direction of the Li⁺ ion as pictured in Figure 8.

Finally, the vector decomposition into systematic and random dynamics allows us to study the Li^+ -independent collectivity of two initially adjacent shell anions by correlating their random motions \vec{e}_1 and \vec{e}_2 . As shown in Figure 8B, the anions exhibit barely a sign of interaction beyond the individual coupling to Li^+ , *i.e.*, neither negative correlations due to plausibly repulsive dynamics of likely charges, nor positive correlations that would evidence a stability of the shell environment. We complete our Li^+ transport scheme accordingly by a non-communicating anion environment and conclude that the vehicular transport description is somewhat misleading when taking it at face value. Last but not least, the absence of displacement dependencies allows us to characterise the dynamic collectivity by a single $\lambda(t)$ and provides the basis for a further simplified model description.

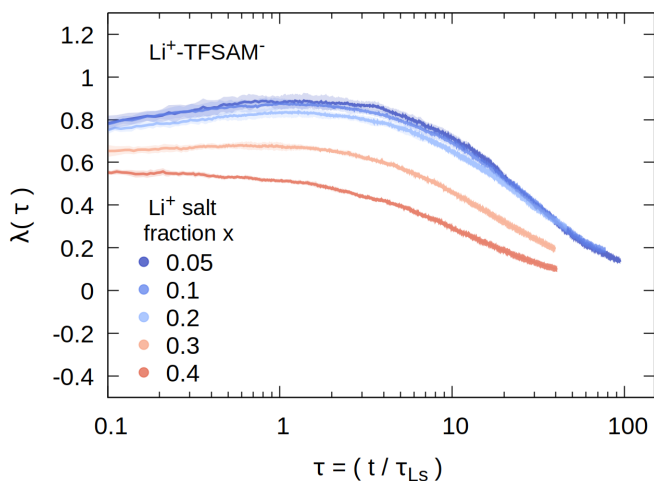


Fig. 9 Exemplary for the TFSAM⁻-based mixtures for various lithium salt concentrations x : LCF λ as a function of τ , which is the time t scaled by the self-diffusion time τ_{Ls} corresponding to concentration x .

5.1.2 Time dependence $\lambda(t)$

Figure 9 shows how the LCF behaves as a function of time. For comparability across different systems, we scale the absolute time t by the mixture-specific self-diffusion time τ_{Ls} . To begin with, we find that the temporal decay of λ is practically identical for low salt fractions. This indicates that the underlying Li^+ transport principle remains unchanged in this concentration regime. As already implied in Figure 8A, a high LCF of $\lambda \approx 0.8$ is maintained over multiple τ_{Ls} until it steadily decreases, reflecting the dissolution of the initial neighborhood. Interestingly, $\lambda(\tau)$ experiences an abrupt downshift when crossing the previously discerned threshold concentration $x=0.3$. Its decay behaviour is increasingly flattened upon the addition of lithium salt and we find for the high salt concentration regime that λ no longer sustains a plateau value as shown in Figure S22[†].

5.1.3 Concentration dependence $\lambda(x)$

On the last level of abstraction, we analyse how λ is affected by the salt content. To obtain a systematic overview, we measure λ at the characteristic self-diffusion time $t = 1 \cdot \tau_{\text{Ls}}$, which coincides closely with the onset of a diffusive Li^+ motion as shown in Figure S8[†]. We compare the concentration behaviour $\lambda(x)$ of the TFSI⁻ versus TFSAM⁻-based mixtures in Figure 10 and make, in accordance with a transport description via $r_{\text{L}/\tau}$, two key observations: Firstly, we find for both setups that the dynamic collectivity of Li^+ and its anionic environment is progressively suppressed. Secondly, the overall reduction is not only greater for the TFSAM⁻-mixtures, for which λ drops by two thirds, but again seems to be triggered when the salt content exceeds a critical threshold of $x = 0.3$. The aforementioned turning point of the Li^+ -shell structure, *e.g.*, the onset of less stable Li^+ binding to the $\text{O}_{\text{TFSAM}^-}$ atoms instead of the more attractive N_{out} cyano-group, remains a plausible explanation. The fact that $\lambda_{\text{Li}^+-\text{N}_{\text{out}}}$ is close to a perfect correlation and significantly higher than $\lambda_{\text{Li}^+-\text{O}_{\text{TFSAM}^-}}$ as depicted in Figure S22[†], further corroborates the understanding that the implementation of such weak coordination sites greatly reduces the dynamic stability of Li^+ environments. We add that for the TFSI⁻-based electrolytes, where Li^+ binding can be mediated through oxygen contacts only, the concentration-induced trend towards both monodentate coordination geometries and higher CNs could have a loosening impact on the cohesiveness of the Li^+ -shell complex as well.

An explanation for the general decrease of the LCF suggests itself from our adopted modelling perspective: We concluded from 2B that with increasing salt concentration a growing ratio of anions must be shared by multiple Li^+ . When an anion is integrated in the solvation shells of two Li^+ , how can it maintain systematic pair dynamics? It seems natural that the LCF of a distinct Li^+ -anion pair comes at the expense of another and thereby effectuates indirectly a liberation of the lithium ions.

To test this hypothesis, we specifically analyse the LCF for two different subensembles which are sketched in Figure 10: Firstly, we select the Li^+ -anion pairs where the anion is bound exclusively to a single Li^+ and compute the LCF λ_1 (red) according to Equation 7. Secondly, we choose the subset of Li^+ -anion pairs where the anions are shared by two Li^+ and evaluate their LCF λ_2 (grey) as per this basic definition. We observe for both electrolyte series that the average λ (blue) makes a clear transition between the subsets λ_1 , which is dominant at low x , and λ_2 which becomes more relevant with increasing x . It is remarkable that both LCFs λ_1 and λ_2 remain nearly constant over a broad concentration regime, except for a slight decrease of λ_1 in the highly concentrated TFSAM⁻ electrolytes. The latter could result from a complex structuring of the electrolyte that further impedes the mobility of Li^+ -anion pairs. The fact that λ_2 is considerably smaller than λ_1 underpins our afore-stated expectation that the systematic anion motion is suppressed through multiple Li^+ -binding.

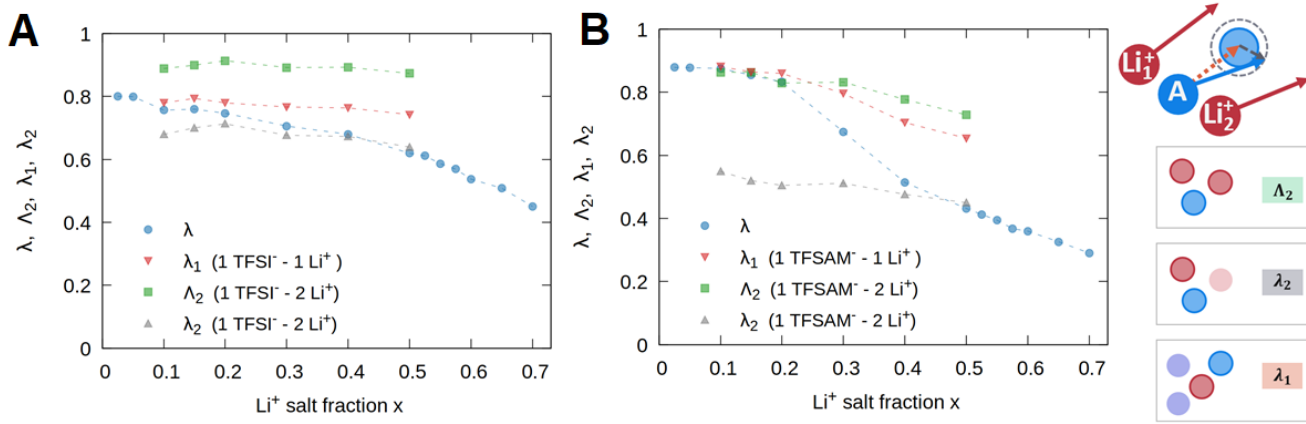


Fig. 10 Concentration dependence of LCFs evaluated at $t = 1 \cdot \tau_{L_S}$ for TFSI⁻ (left) and TFSAM⁻ (right) - based electrolytes. The blue symbols show the LCF λ averaged over all Li⁺-anion pairs. The green data points show the LCF Λ_2 of one anion to the average displacement $\vec{U} = \frac{1}{2}(\vec{u}_{Li_1^+} + \vec{u}_{Li_2^+})$ of two initially binding Li-ions as illustrated in the sketches. λ_1 (red) and λ_2 (grey) compare the coupling strengths for the subsets where the anion binds to a single Li⁺ (λ_1) or is shared between two Li⁺ (λ_2).

We challenge the strength of our transport observable and generically extend the LCF formalism for the ensemble of anions which have two Li⁺ neighbours:

$$\vec{v}_j = \Lambda_2 \cdot \vec{U}_i^j + \vec{\mathcal{E}}_j \quad \text{with} \quad \vec{U}_i^j = \frac{1}{2}(\vec{u}_{Li_1^+}^j + \vec{u}_{Li_2^+}^j) \quad (10)$$

$$\Lambda_2 = \frac{\langle \vec{U}_i^j \vec{v}_j \rangle}{\langle \vec{U}^2 \rangle} \quad \wedge \quad \langle \vec{\mathcal{E}}^2 \rangle = \langle \vec{v}^2 \rangle - \Lambda_2^2 \cdot \langle \vec{U}^2 \rangle.$$

In this this approach, we correlate the displacement \vec{v}_j of double coordinating anions with the average displacement vector of the two Li⁺ as if they merged to a quasi-lithium particle. Of course, the equal weighting of the Li⁺ displacements omits that different binding geometries and sites may entail different coupling strengths. Nevertheless, we find that Λ_2 (green) recovers the systematic transport characteristics λ_1 on this higher level of abstraction surprisingly well in terms of concentration dependence and for the TFSAM⁻-based mixtures also regarding the absolute value. This means that although the anion motion decreasingly follows that of distinct Li⁺, it is coupled in a good approximation to their mean displacement vector. It therefore appears that the Li⁺-transport behaviour at high salt concentrations bears significant similarity to the transport mechanism characterised for diluted electrolytes.

The introduced LCFs are observables that are presently only accessible through simulation but not experimentally measurable. However, returning to the ratio of Li⁺ and anion diffusion coefficients, whose concentration dependence was the experimentally found indication to postulate a change of Li⁺ transport mechanism¹⁹, we can use our formalism to elucidate why D_{Li^+}/D_{anion} increases with salt content.

After squaring and rearranging the anion dynamics' decomposition for the different subensembles according to Equations 8 and 10, the inverse ratio D_{anion}/D_{Li^+} can be expressed through the

observables of systematic and random motion:

$$\text{subensemble of } \lambda_1 : \frac{\langle \vec{v}^2 \rangle}{\langle \vec{u}^2 \rangle} = \lambda_1^2 + \frac{\langle \vec{\mathcal{E}}^2 \rangle}{\langle \vec{u}^2 \rangle}$$

$$\text{subensemble of } \Lambda_2 : \frac{\langle \vec{v}^2 \rangle}{\langle \vec{u}^2 \rangle} = \Lambda_2^2 \cdot \underbrace{\frac{1}{2} \left(1 + \frac{\langle \vec{u}_1 \vec{u}_2 \rangle}{\langle \vec{u}^2 \rangle} \right)}_{<1} + \frac{\langle \vec{\mathcal{E}}^2 \rangle}{\langle \vec{u}^2 \rangle}. \quad (11)$$

Please note the special term including the Li₁⁺ - Li₂⁺ interaction which occurs for the subensemble of Λ_2 . While we found that the coupling strengths $\lambda_1 \lesssim \Lambda_2$ depend only marginally on salt content, it is a priori not known how the terms $\langle \vec{\mathcal{E}}^2 \rangle / \langle \vec{u}^2 \rangle$, $\langle \vec{\mathcal{E}}^2 \rangle / \langle \vec{u}^2 \rangle$, and $\langle \vec{u}_1 \vec{u}_2 \rangle / \langle \vec{u}^2 \rangle$, as well as $\langle \vec{u}^2 \rangle$ for the two subensembles behave as a function of x . As presented in Figures S26[†]-S29[†], analysis shows, firstly, that $\langle \vec{u}^2 \rangle$ is almost identical for all subensembles and, secondly, that the random motion is even slightly reduced for the double Li⁺-bound anions $\langle \vec{\mathcal{E}}^2 \rangle / \langle \vec{u}^2 \rangle \lesssim \langle \vec{\mathcal{E}}^2 \rangle / \langle \vec{u}^2 \rangle$. Thirdly, we find that $\langle \vec{\mathcal{E}}^2 \rangle / \langle \vec{u}^2 \rangle$, $\langle \vec{\mathcal{E}}^2 \rangle / \langle \vec{u}^2 \rangle$, and $\langle \vec{u}_1 \vec{u}_2 \rangle / \langle \vec{u}^2 \rangle$ are constant within 15% with respect to x in the regime of moderate salt concentration. The explanatory power of these empirical observations with regard to D_{anion}/D_{Li^+} lies in the Li₁⁺ - Li₂⁺ interaction: As to be expected for their cross correlation, we find $\langle \vec{u}_1 \vec{u}_2 \rangle / \langle \vec{u}^2 \rangle < 1$, e.g., $\langle \vec{u}_1 \vec{u}_2 \rangle / \langle \vec{u}^2 \rangle \approx 0.3$ in the TFSAM⁻-based electrolytes which is shown in Figure S27[†]. Given the quantitative similarity of the remaining terms and factors stated in Equation 11 for both subensembles, the reluctance of Li₁⁺ - Li₂⁺ to collective motion effectuates a lower $\langle \vec{v}^2 \rangle / \langle \vec{u}^2 \rangle$ for the anions coordinating two Li⁺. Since the share of the latter increases with salt concentration, the overall D_{anion}/D_{Li^+} is reduced systematically. Consequently, the emergence of a fundamentally different Li⁺ transport mechanism such as hopping is yet a possible but not a necessary explanation for the increasing D_{Li^+}/D_{anion} ratio.

5.1.4 Dynamic heterogeneity

Even though our preceding analysis does not suggest systematic hopping diffusion of Li^+ in the IL-matrix at elevated salt concentration, its possibility cannot be ruled out so far. A typical signature of such hopping events is the occurrence of humps or additional peaks in the self-part of lithium's van Hove function $G_s(r,t)$, which probes the displacement distribution within time t ^{56–58}. Figure S30[†] reveals the absence of such secondary peaks in all electrolyte mixtures despite their strong local structuring which is reflected in $g_{\text{Li}^+ - \text{Li}^+}$ at high salt concentrations (see Figure S1[†]). Furthermore, we find an increasing deviation from an ideal Gaussian behaviour $G_{0,s}$. Such dynamic heterogeneities are commonly observed in IL-based materials^{56–58} and generally quantified via the non-Gaussian parameter $\alpha_2(t)$. We find that the maximum heterogeneity $\alpha_2(t)$ approximately coincides for Li^+ , Pyr_{14}^+ and respective anion (see Figure S31[†]), which suggests that their heterogeneous dynamics are coupled and possibly located altogether in faster moving regions.

6 Conclusions

In this work, we explored the structural and dynamic properties of lithium salt/binary IL mixtures over a broad range of salt content, employing the intensively studied TFSI⁻ anion and the asymmetric analogue TFSAM⁻. Our results confirmed the distinctive structural and dynamic characteristics of the TFSAM⁻-based electrolytes which were observed in a recent experimental study. At small salt fractions TFSAM⁻ coordinated to Li^+ exclusively via the cyano-nitrogen, but when exceeding a threshold concentration of $x=0.3$ the Li^+ environment became increasingly diverse. The shorter mean residence times $\tau_{\text{Li}^+ - \text{TFSAM}^-}$ were a strong indicator that Li^+ was weaker bound in the emerging configurations.

We further studied the dynamic properties of the Li^+ -solvation complex in the framework of generally adopted analysis procedures, e.g., discussion of D_{Li^+} relative to D_{anion} or $\tau_{\text{Li}^+ - \text{anion}}$. The results gave consistent evidence of strongly collective Li^+ -shell motion at small salt fractions in both electrolyte mixtures and showed that the extent of joint Li^+ -anion dynamics declines systematically with increasing salt content.

We developed a novel approach that measures the extent to which the dynamics of an initially Li^+ -bound anion remain coupled to the respective Li^+ , and could analyse key features of the solvation shell which is commonly interpreted as a vehicle guiding Li^+ diffusion. Our findings showed that the solvation shell by no means behaved like a stable vehicle. Thus, we suggest to reconsider the description of Li^+ transport in terms of a vehicular mechanism. Instead, our observations highlighted a flow-like motion of Li^+ and its anionic environment and we propose a "coupled diffusion"-conception to be more suitable.

We could discern two different causes of the decreasingly coupled diffusion for the concentrated electrolytes: On the one hand, an increased anion-sharing between Li-ions weakened the dynamic coupling strength of an individual Li^+ -anion pair. On the other hand, the novel TFSAM⁻ anion demonstrated how the incorporation of different binding sites, among which Li^+ showed

clear interaction preferences, had a further loosening effect in the emerging ion network. In the light of the structure-dynamics relationship elucidated in this work, tuning the Li^+ coordination environment appears to be a promising path for a tailored electrolyte design.

We believe that our methodology to characterise the collective dynamics of a central particle and its environment can easily be applied to similar research areas where transport phenomena are studied.

Conflicts of interest

There are no conflicts to declare.

Acknowledgements

Analysis and simulations have been performed on the computing cluster PALMA2 at the University of Münster. We thankfully acknowledge the financial support from MWIDE NRW as part of the "GrEEen" project (funding code: 313-W044A).

Notes and references

- 1 A. Eftekhari, Y. Liu and P. Chen, *Journal of Power Sources*, 2016, **334**, 221–239.
- 2 K. Ghandi, *Green and Sustainable Chemistry*, 2014, **2014**, 44–53.
- 3 M. Galiński, A. Lewandowski and I. Stępnia, *Electrochimica acta*, 2006, **51**, 5567–5580.
- 4 M. Armand, F. Endres, D. R. MacFarlane, H. Ohno and B. Scrosati, in *Materials For Sustainable Energy: A Collection of Peer-Reviewed Research and Review Articles from Nature Publishing Group*, World Scientific, 2011, pp. 129–137.
- 5 D. R. MacFarlane, N. Tachikawa, M. Forsyth, J. M. Pringle, P. C. Howlett, G. D. Elliott, J. H. Davis, M. Watanabe, P. Simon and C. A. Angell, *Energy & Environmental Science*, 2014, **7**, 232–250.
- 6 G. A. Elia, U. Ulissi, S. Jeong, S. Passerini and J. Hassoun, *Energy & Environmental Science*, 2016, **9**, 3210–3220.
- 7 H. Yoon, P. Howlett, A. S. Best, M. Forsyth and D. R. Macfarlane, *Journal of the Electrochemical Society*, 2013, **160**, A1629.
- 8 S. Wilken, S. Xiong, J. Scheers, P. Jacobsson and P. Johansson, *Journal of Power Sources*, 2015, **275**, 935–942.
- 9 A. Lewandowski and A. Świdarska-Mocek, *Journal of Power Sources*, 2009, **194**, 601–609.
- 10 R. D. Rogers and K. R. Seddon, *Science*, 2003, **302**, 792–793.
- 11 Q. Zhou, P. D. Boyle, L. Malpezzi, A. Mele, J.-H. Shin, S. Passerini and W. A. Henderson, *Chemistry of Materials*, 2011, **23**, 4331–4337.
- 12 M. Brinkötter, E. I. Lozinskaya, D. O. Ponkratov, P. S. Vlasov, M. P. Rosenwinkel, I. A. Malyshkina, Y. Vygodskii, A. S. Shaplov and M. Schönhoff, *Electrochimica Acta*, 2017, **237**, 237–247.
- 13 G. A. Giffin, A. Moretti, S. Jeong and S. Passerini, *Journal of Power Sources*, 2017, **342**, 335–341.
- 14 D. Reber, N. Takenaka, R.-S. Kühnel, A. Yamada and

- C. Battaglia, *The Journal of Physical Chemistry Letters*, 2020, **11**, 4720–4725.
- 15 A. S. Shaplov, E. I. Lozinskaya, P. S. Vlasov, S. M. Morozova, D. Y. Antonov, P.-H. Aubert, M. Armand and Y. S. Vygodskii, *Electrochimica Acta*, 2015, **175**, 254–260.
- 16 J.-P. Hoffknecht, M. Drews, X. He and E. Paillard, *Electrochimica Acta*, 2017, **250**, 25–34.
- 17 M. J. Marczewski, B. Stanje, I. Hanzu, M. Wilkening and P. Johansson, *Physical Chemistry Chemical Physics*, 2014, **16**, 12341–12349.
- 18 G. M. Girard, M. Hilder, H. Zhu, D. Nucciarone, K. Whitbread, S. Zavorine, M. Moser, M. Forsyth, D. R. Macfarlane and P. C. Howlett, *Physical Chemistry Chemical Physics*, 2015, **17**, 8706–8713.
- 19 P. Nürnberg, E. I. Lozinskaya, A. S. Shaplov and M. Schönhoff, *The Journal of Physical Chemistry B*, 2020, **124**, 861–870.
- 20 D. Van Der Spoel, E. Lindahl, B. Hess, G. Groenhof, A. E. Mark and H. J. Berendsen, *Journal of Computational Chemistry*, 2005, **26**, 1701–1718.
- 21 S. Páll, M. J. Abraham, C. Kutzner, B. Hess and E. Lindahl, *Solving Software Challenges for Exascale*, Cham, 2015, pp. 3–27.
- 22 M. J. Abraham, T. Murtola, R. Schulz, S. Páll, J. C. Smith, B. Hess and E. Lindahl, *SoftwareX*, 2015, **1-2**, 19–25.
- 23 H. J. Berendsen, D. van der Spoel and R. van Drunen, *Computer Physics Communications*, 1995, **91**, 43–56.
- 24 A. S. Gouveia, C. E. Bernardes, L. C. Tomé, E. I. Lozinskaya, Y. S. Vygodskii, A. S. Shaplov, J. N. C. Lopes and I. M. Marrucho, *Physical Chemistry Chemical Physics*, 2017, **19**, 29617–29624.
- 25 J. N. Canongia Lopes and A. A. Pádua, *Theoretical Chemistry Accounts*, 2012, **131**, 1–11.
- 26 J. N. Canongia Lopes, J. Deschamps and A. A. H. Pádua, *The Journal of Physical Chemistry B*, 2004, **108**, 2038–2047.
- 27 J. N. Lopes and A. A. Pádua, *Journal of Physical Chemistry B*, 2004, **108**, 16893–16898.
- 28 K. Shimizu, D. Almantariotis, M. F. Costa Gomes, A. A. Pádua and J. N. Canongia Lopes, *Journal of Physical Chemistry B*, 2010, **114**, 3592–3600.
- 29 J. Self, K. D. Fong and K. A. Persson, *ACS Energy Letters*, 2019, **4**, 2843–2849.
- 30 N. Molinari, J. P. Mailoa and B. Kozinsky, *The journal of physical chemistry letters*, 2019, **10**, 2313–2319.
- 31 N. Molinari and B. Kozinsky, *The Journal of Physical Chemistry B*, 2020, **124**, 2676–2684.
- 32 A. Thum, A. Heuer, K. Shimizu and J. N. C. Lopes, *Physical Chemistry Chemical Physics*, 2020, **22**, 525–535.
- 33 Q. Huang, T. C. Lourenço, L. T. Costa, Y. Zhang, E. J. Maginn and B. Gurkan, *The Journal of Physical Chemistry B*, 2018, **123**, 516–527.
- 34 S. Nosé and M. Klein, *Molecular Physics*, 1983, **50**, 1055–1076.
- 35 S. Nosé, *Molecular Physics*, 1984, **52**, 255–268.
- 36 W. G. Hoover, *Physical Review A*, 1985, **31**, 1695–1697.
- 37 M. Parrinello and A. Rahman, *Journal of Applied Physics*, 1981, **52**, 7182–7190.
- 38 O. Borodin, G. A. Giffin, A. Moretti, J. B. Haskins, J. W. Lawson, W. A. Henderson and S. Passerini, *The Journal of Physical Chemistry C*, 2018, **122**, 20108–20121.
- 39 Z. Li, O. Borodin, G. D. Smith and D. Bedrov, *The Journal of Physical Chemistry B*, 2015, **119**, 3085–3096.
- 40 P. Kubisiak, P. Wróbel and A. Eilmes, *The Journal of Physical Chemistry B*, 2019, **124**, 413–421.
- 41 Z. Li, G. D. Smith and D. Bedrov, *The Journal of Physical Chemistry B*, 2012, **116**, 12801–12809.
- 42 M. J. Monteiro, F. F. Bazito, L. J. Siqueira, M. C. Ribeiro and R. M. Torresi, *The Journal of Physical Chemistry B*, 2008, **112**, 2102–2109.
- 43 J. B. Haskins, W. R. Bennett, J. J. Wu, D. M. Hernandez, O. Borodin, J. D. Monk, C. W. Bauschlicher Jr and J. W. Lawson, *The Journal of Physical Chemistry B*, 2014, **118**, 11295–11309.
- 44 F. Chen, P. Howlett and M. Forsyth, *The Journal of Physical Chemistry C*, 2018, **122**, 105–114.
- 45 V. Lesch, S. Jeremias, A. Moretti, S. Passerini, A. Heuer and O. Borodin, *The Journal of Physical Chemistry B*, 2014, **118**, 7367–7375.
- 46 Y. Zhang and E. J. Maginn, *The Journal of Physical Chemistry Letters*, 2015, **6**, 700–705.
- 47 K. D. Fong, J. Self, K. M. Diederichsen, B. M. Wood, B. D. McCloskey and K. A. Persson, *ACS central science*, 2019, **5**, 1250–1260.
- 48 D. Dong and D. Bedrov, *The Journal of Physical Chemistry B*, 2018, **122**, 9994–10004.
- 49 K.-D. Kreuer, *Chemistry of materials*, 1996, **8**, 610–641.
- 50 T. Norbya, *Solid State Ionics*, 1990, **40**, 857–862.
- 51 Q. Li, Q. Yin, Y.-S. Zheng, Z.-J. Sui, X.-G. Zhou, D. Chen and Y.-A. Zhu, *Langmuir*, 2019, **35**, 9962–9969.
- 52 K. Kreuer, *Angew. Chem. Int. Ed. Eng*, 1982, **21**, 208–211.
- 53 N. Agmon, *Chemical Physics Letters*, 1995, **244**, 456–462.
- 54 O. Borodin, G. D. Smith and W. Henderson, *The Journal of Physical Chemistry B*, 2006, **110**, 16879–16886.
- 55 M. Forsyth, H. Yoon, F. Chen, H. Zhu, D. R. MacFarlane, M. Armand and P. C. Howlett, *The Journal of Physical Chemistry C*, 2016, **120**, 4276–4286.
- 56 H. Liu and E. Maginn, *The Journal of Chemical Physics*, 2011, **135**, 124507.
- 57 H. Liu, X. Luo, A. P. Sokolov and S. J. Paddison, *The Journal of Physical Chemistry B*, 2021, **125**, 372–381.
- 58 S. Mukherji, N. V. Avula, R. Kumar and S. Balasubramanian, *The Journal of Physical Chemistry Letters*, 2020, **11**, 9613–9620.

ELECTRONIC SUPPLEMENTARY INFORMATION

Controlling Li^+ transport in ionic liquid electrolytes through salt content and anion asymmetry: A mechanistic understanding gained from molecular dynamics simulations

Alina Wettstein,^{*,†} Diddo Diddens,[‡] and Andreas Heuer^{*,‡,†}

[†]*Institut für physikalische Chemie, Westfälische Wilhelms-Universität Münster, Corrensstraße 28/30, D-48149 Münster, Germany*

[‡]*Institut für Energie- und Klimaforschung, Ionics in Energy Storage, Helmholtz Institut Münster, Forschungszentrum Jülich, Corrensstraße 46, 48149 Münster, Germany*

E-mail: alina.wettstein@gmail.com; andheuer@wwu.de

A: Simulation protocol

All-atomistic molecular dynamics (MD) simulations of lithium salt-ionic liquid (IL) mixtures were performed using the software package GROMACS (version 2018.8).¹⁻⁴ The atomic interactions were parameterized according to well-established OPLS-AA⁵-derived CL&P force field developed by Canongia Lopes and Padua specifically for modeling ILs.⁶⁻¹⁰ Electronic polarization and charge transfer effects were accounted for in a mean field sense via rescaling the atomic point charges, which is the prevalent practice when relying on non-polarizable force fields to study ionic liquids,¹¹⁻²⁰ because a more accurate treatment of the electronic polarizability by means of Drude oscillators²¹ or induced point dipoles²² comes at a great computational cost. Very recent studies on lithium salt-ionic liquid mixtures¹⁷⁻²⁰ and a variety of lithium salt containing electrolytes^{14,15,23} have demonstrated successfully the ability of non-polarizable force fields, employing scaled partial charges, to capture and confirm experimental observations. In this work the the atomic point charges of all species were uniformly scaled down by a factor of 0.8.^{11,17-20} We study structural and dynamical properties of the $\text{Li}_x^+ - \text{Pyr}_{14,(1-x)}^+ - \text{TFSI}^-$ and $\text{Li}_x^+ - \text{Pyr}_{14,(1-x)}^+ - \text{TFSAM}^-$ electrolytes in the

same concentration range from $x = 0.0$ (neat IL) to $x = 0.7$ as experimentally reported in.²⁴

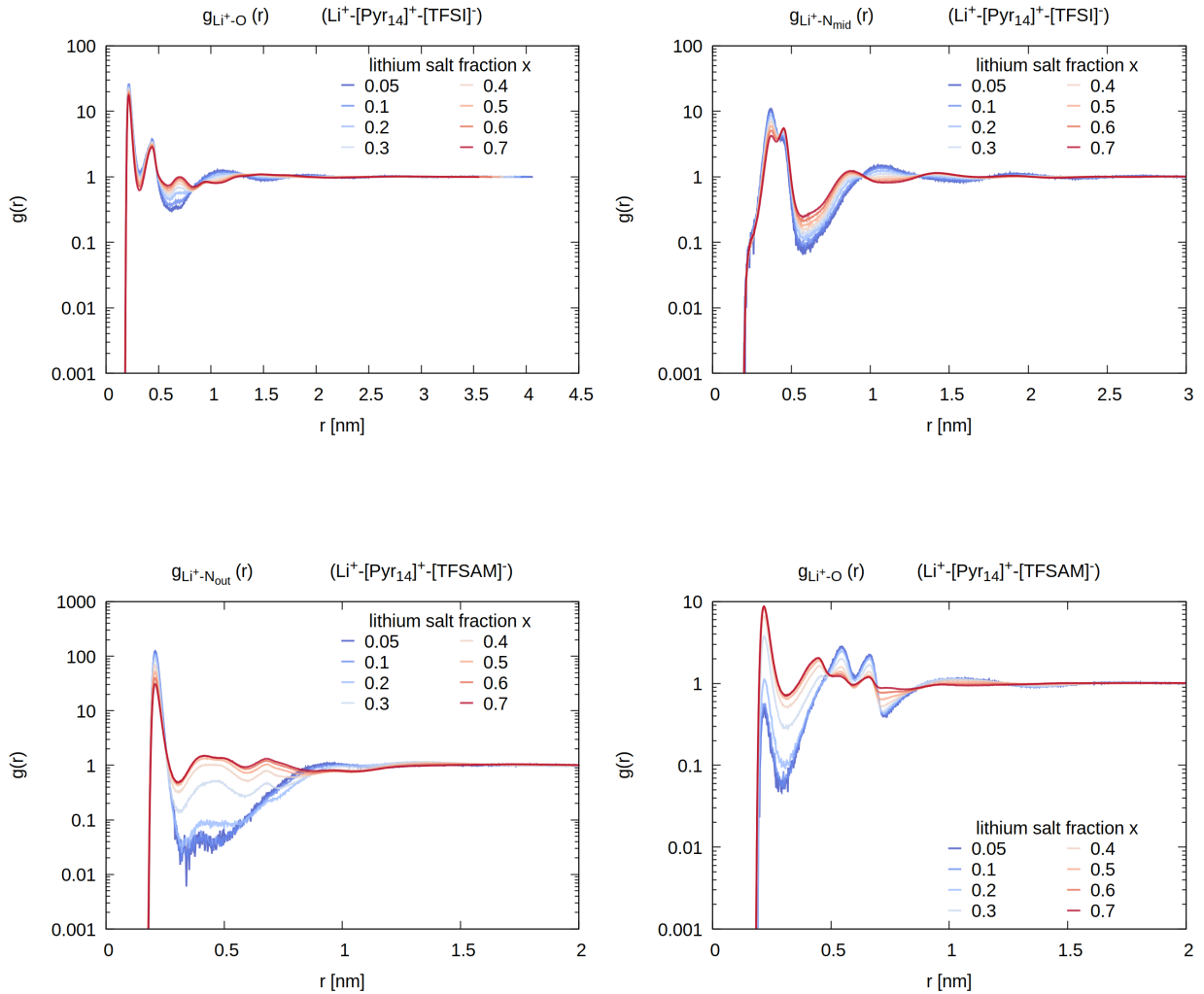
The initial configurations were created with the PACKMOL software²⁵ which randomly distributed 1000 ion pairs, corresponding to the respective lithium salt to ionic liquid ratio, in a cubic box. The systems were first exposed to an energy minimization and then pre-equilibrated under NPT conditions for 40 ns at a high temperature of 500 K controlling pressure via a Berendsen barostat (relaxation time constant $\tau_P = 5.0$ ps, compressibility of 4.5×10^{-5} bar) coupled to a reference pressure of 1 bar and temperature via a velocity-rescale thermostat (relaxation time constant $\tau_T = 1.0$ ps).^{26,27} Then the systems were cooled down to 400 K and equilibrated for another 100 ns. In the subsequent production run of 400 ns duration, that was used for data acquisition, pressure and temperature were coupled to an extended Parrinello-Rahman and Nosé-Hoover ensemble using the same relaxation time constants as before.²⁸⁻³¹ The equations of motion were solved via the leap-frog algorithm at a time step of 2 fs. The center of mass of the system was repositioned every simulation step. Furthermore, cutoffs for the long range electrostatic and the van der Waals interactions were both set to 1.4 nm and the linear constraint solver (LINCS) was employed to constrain the hydrogen bonds.^{32,33} The simulation trajectories were analyzed with custom scripts supported by the Python library MDAnalysis.^{34,35}

B: Structural properties

The radial distribution functions $g_{\text{Li}^+-\text{X}}$ are computed according to

$$g_{ab}(r) = \frac{V}{4\pi r^2 N_a N_b} \sum_{i=1}^{N_a} \sum_{j=1}^{N_b} \langle \delta(|\vec{r}_i - \vec{r}_j| - r) \rangle, \quad (1)$$

where N_a/V and N_b/V denotes the average number density of species a and species b with V being the volume of the simulation box. The brackets $\langle \cdot \rangle$ indicate the ensemble average.



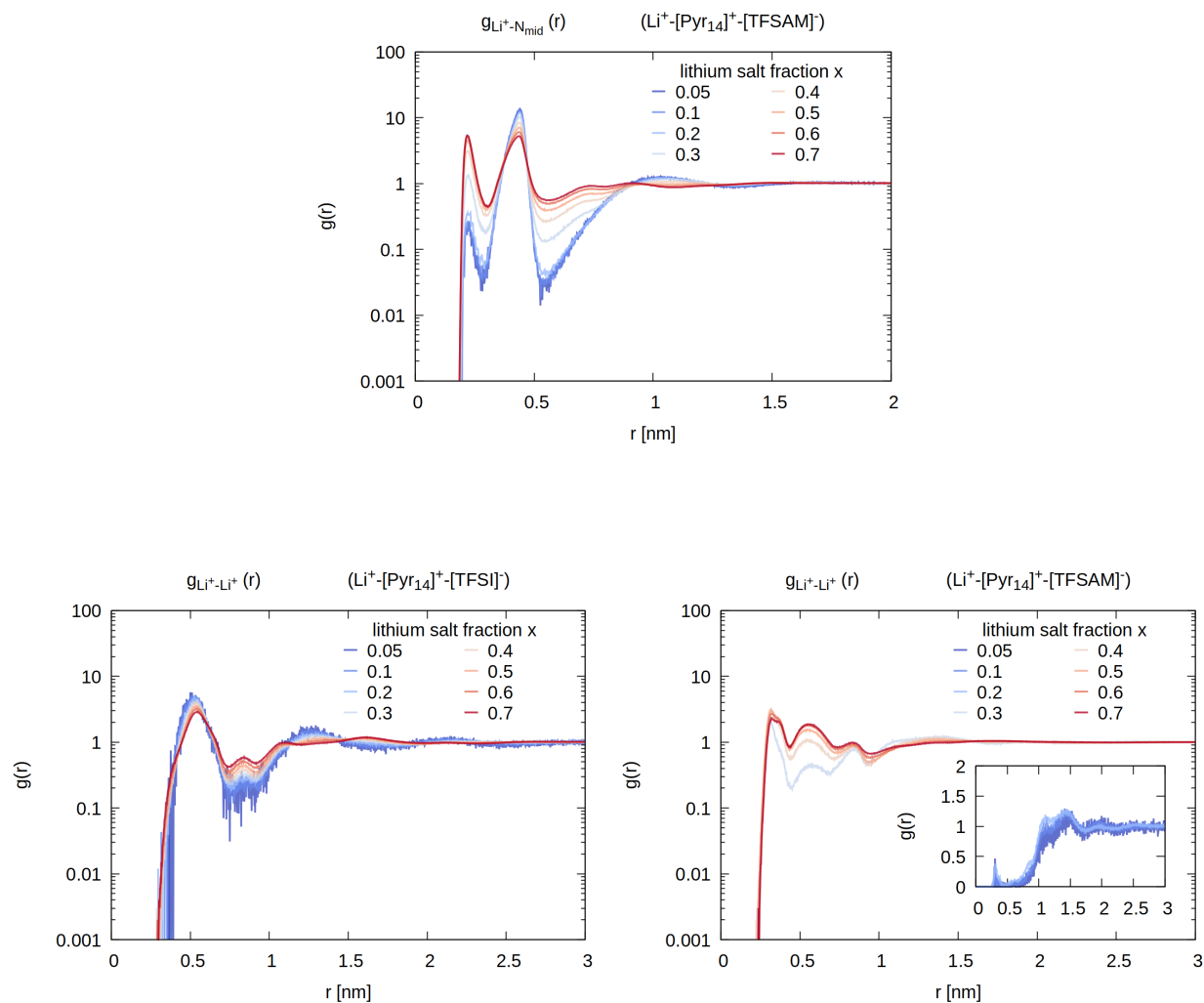


Figure S1: Overview of radial distribution functions $g_{\text{Li}^+-X}(r)$ between Li^+ ions and nitrogen / oxygen binding sites provided by TFSI^- and TFSAM^- as well as $g_{\text{Li}^+-\text{Li}^+}(r)$ in both electrolyte series on a log scale.

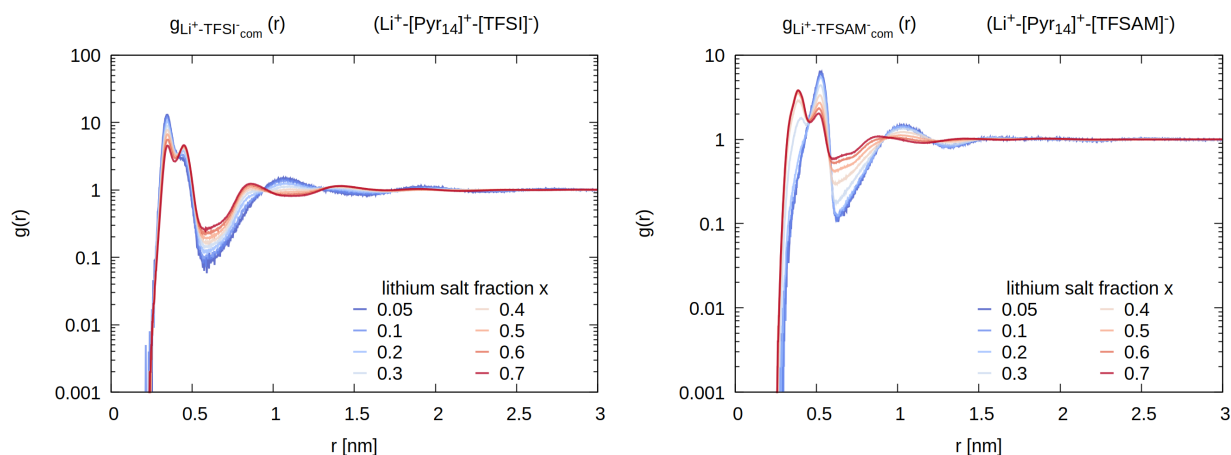


Figure S2: Overview of lithium - anion(com) radial distribution functions $g_{\text{Li}^+-\text{anion}_{\text{com}}}(\mathbf{r})$ on a log scale. The global minimum position is employed as the solvation shell size L_s in analogy to the procedure introduced by Self et al.¹⁴

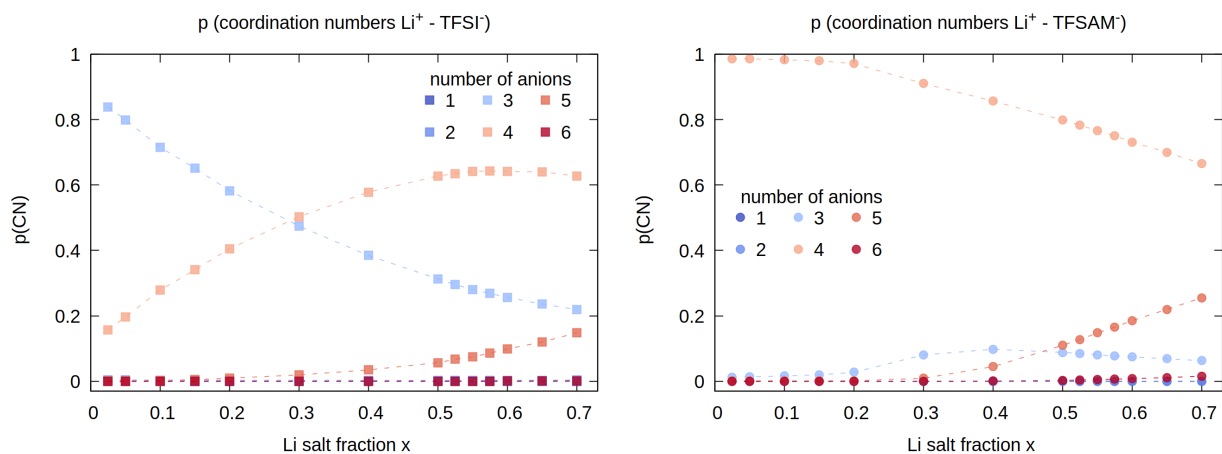


Figure S3: Probability distribution of Li^+ -anion coordination numbers in the TFSI^- (left) and TFSAM^- (right) -based electrolytes as a function of lithium salt content x .

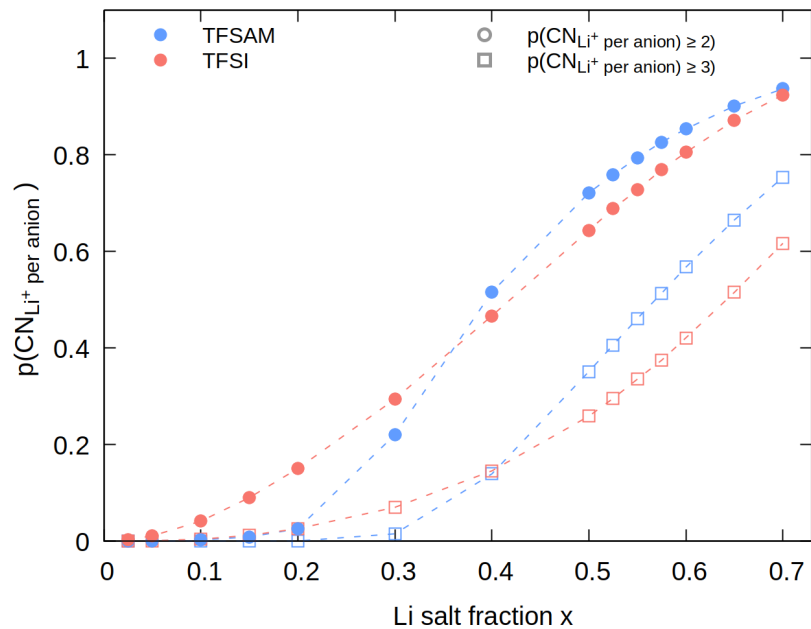


Figure S4: Probability distribution of lithium neighbors per TFSI⁻/TFSAM⁻ p(CN_{Li⁺ per anion}) as a function of lithium salt content x.

C: Mean squared displacements

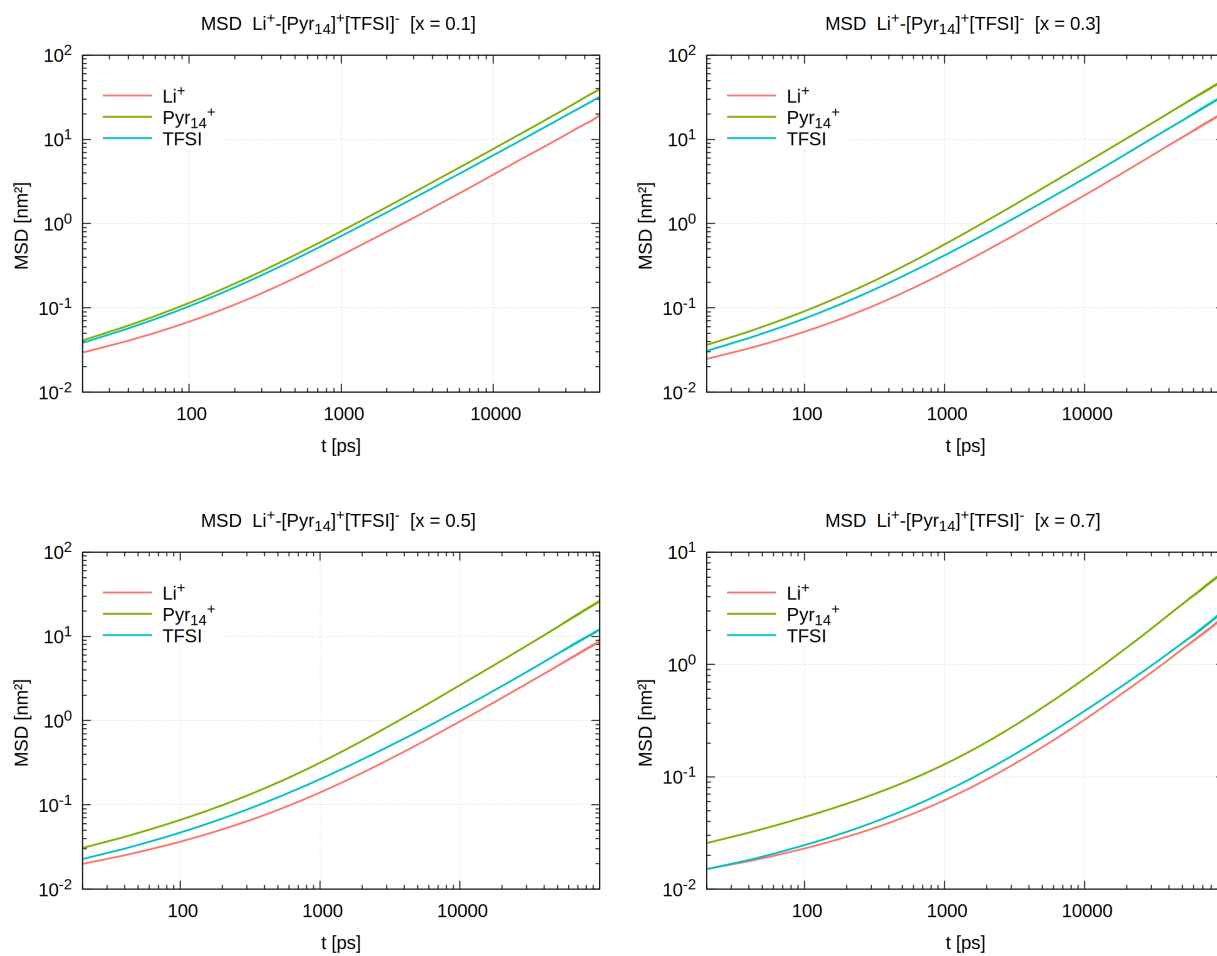


Figure S5: Example mean squared displacements of Li^+ , Pyr_{14}^+ and TFSI^- as a function of time for lithium salt contents $x=0.1$ and $x=0.3$ (top) as well as $x=0.5$ and $x=0.7$ (bottom).

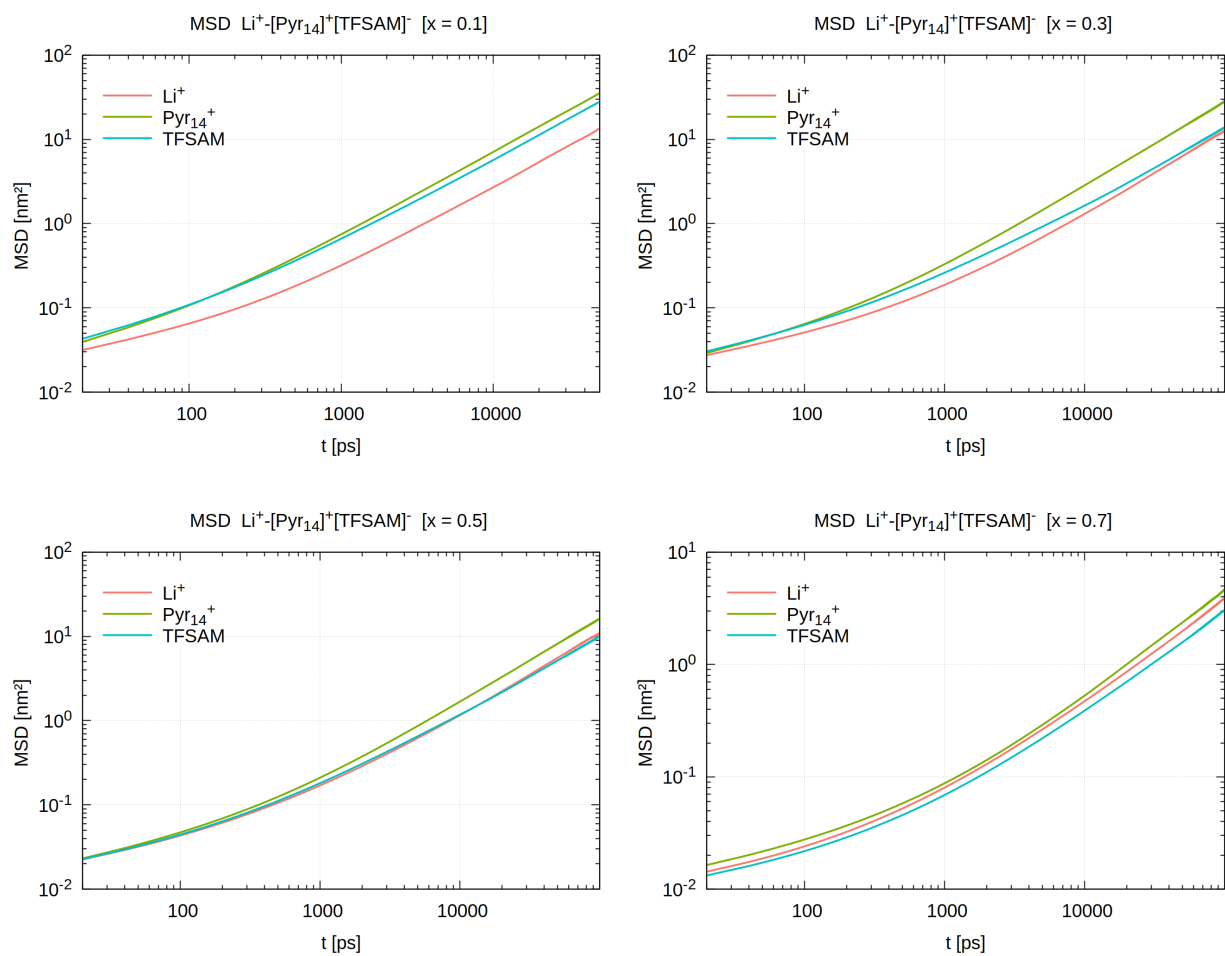


Figure S6: Example mean squared displacements of Li^+ , Pyr_{14}^+ and TFSAM^- as a function of time for lithium salt contents $x=0.1$ and $x=0.3$ (top) as well as $x=0.5$ and $x=0.7$ (bottom).

D: Mean residence times

The mean residence times shown in the main part of the manuscript are computed from the residence time autocorrelation function (ACF) as in reference³⁶ :

$$\text{ACF}_{ij}(t) = \frac{\left\langle H_{ij}(t')H_{ij}(t'+t) \right\rangle}{\left\langle H_{ij}(t')H_{ij}(t) \right\rangle}, \quad (2)$$

where H_{ij} evaluates to 1 when species j is found within the assigned cutoff to species i and otherwise set to 0. If not mentioned otherwise, the first minimum position of the radial distribution function $g_{\text{Li}^+-X}(r)$ is employed as the cutoff distance to determine present $\text{Li}^+ - X$ binding. The brackets $\langle \dots \rangle$ denote the ensemble average over all pairs ij and time origins t' . The ACF is then fitted by a stretched exponential $f(t)$:

$$f(t) = \exp \left(-(t/\tau')^\beta \right), \quad (3)$$

where β and τ' are the fitting parameters. The mean residence time $\langle \tau \rangle$ is obtained from the integral:

$$\langle \tau \rangle = \int_0^\infty dt \exp \left(-(t/\tau')^\beta \right) = \frac{\tau'}{\beta} \Gamma(1/\beta) \quad (4)$$

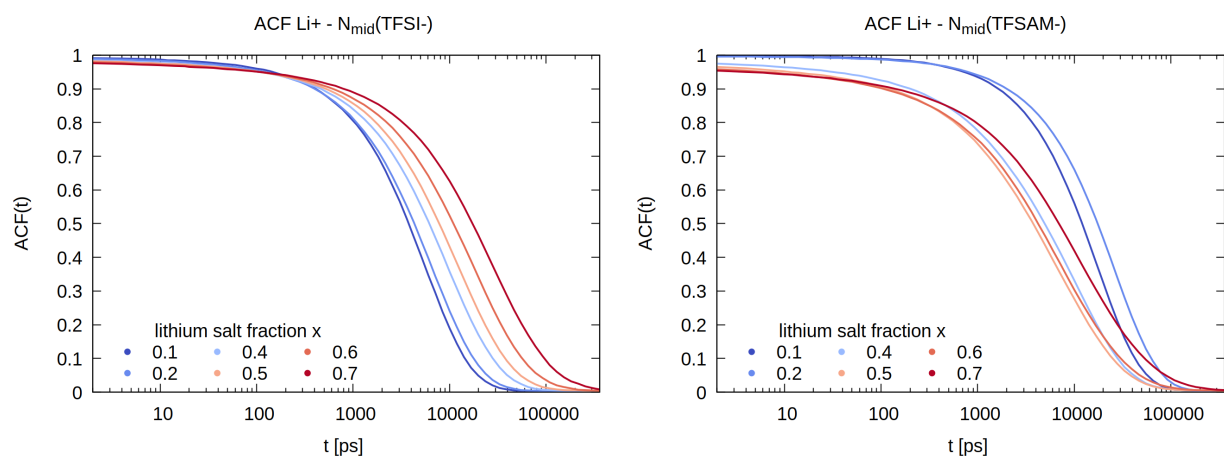


Figure S7: Exemplary overview of the concentration dependence of the autocorrelation functions of $\text{Li}^+ - \text{TFSI}^-$ and $\text{Li}^+ - \text{TFSAM}^-$ measured via N_{mid} employing cutoffs of 5.5 \AA .

E: Deviation of $\text{MSD}_{\text{Li}^+}(\tau_{\text{LS}})$ from diffusive dynamics

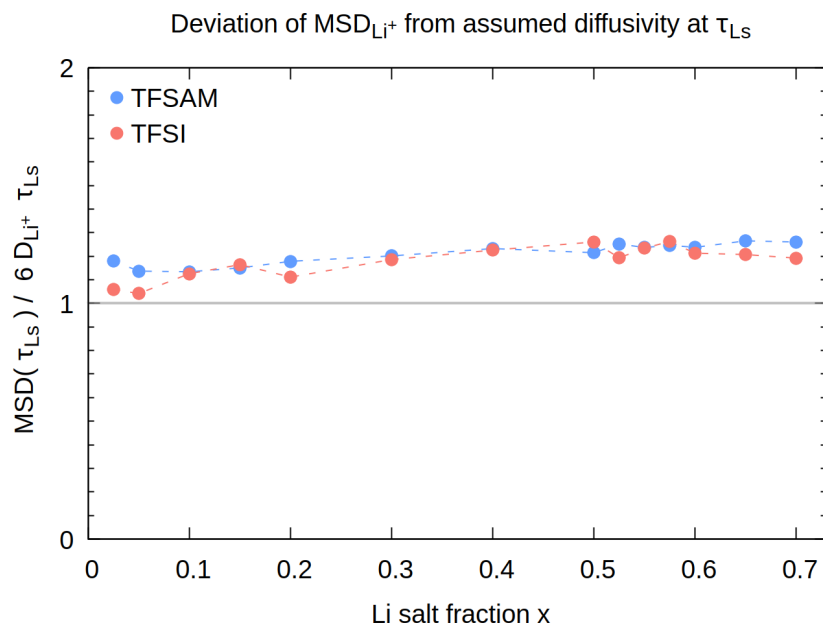


Figure S8: Evaluating the deviation from purely diffusive lithium dynamics at critical time scale τ_{LS} , i.e. $\text{MSD}_{\text{Li}^+}(t) = 6D_{\text{Li}^+}t$ at times τ_{LS} .

F: $p(\Delta v_{\parallel})$ for various lag times and lithium subensembles

The panels in Figure S9 show the distributions $p(\Delta v_{\parallel})$ of TFSI⁻ and TFSAM⁻ relative distances in direction of the lithium displacement for salt concentrations $x = 0.05, 0.1, 0.2$ and 0.5 . The upper panels (a, b and c) display the histograms obtained for the anions whose designated lithium ions exhibit a squared displacement equal to the lithium mean squared displacement at the corresponding time t , i.e. $u^2 = 1 \cdot \langle u^2 \rangle$. The lower panels (d, e and f) measure $p(\Delta v_{\parallel})$ for the subensemble of lithium ions which achieved a squared displacement $u^2 = 3 \cdot \langle u^2 \rangle$.

In order to extend the statistical analysis of the subensembles to a larger data set, we introduce a tolerance interval $\{u_1^2 \leq u^2 \leq u_r^2\}$, whose upper and lower boundaries u_1^2 and u_r^2 are set in such a way that the sampled average u^2 of the subensemble corresponds to the target $k \cdot \langle u^2 \rangle$ (see Table S1). Because the lithium ions' individual squared displacements are normally distributed the threshold boundaries cannot be chosen symmetrically.

To characterize the peak positions and widths, we proceed according to the following protocol:

1. Δv_{\parallel} is measured according to Equation 5 in the main manuscript and discretized employing a bin width of 0.1 \AA and normalized. For reasons of visual appearance the histograms shown in the panels employ a bin width of 0.5 \AA .
2. The obtained histogram $p(\Delta v_{\parallel})$ is empirically fitted by a Gaussian function
$$g(x) = \tilde{a} \cdot \exp\left(\frac{(x - \tilde{\mu})^2}{2\tilde{\sigma}^2}\right)$$
 with the amplitude \tilde{a} , the expected value $\tilde{\mu}$ and variance $\tilde{\sigma}^2$.
3. Since anions naturally decouple from the lithium ion's dynamics upon detachment, it seems plausible that the distributions exhibit a skew towards negative Δv_{\parallel} values. We find that an increasing amount of initial lithium-anion pairs has separated over time and is reflected in a growing tail of $p(\Delta v_{\parallel})$. To separate the peak features belonging to

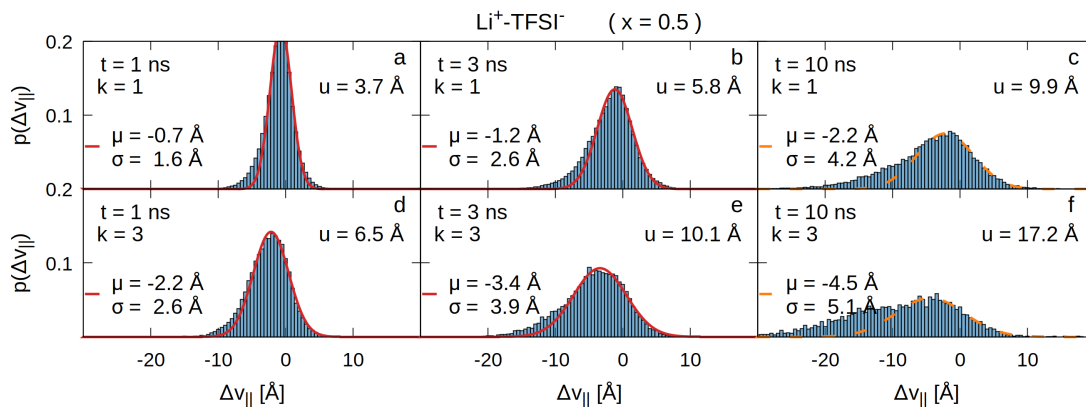
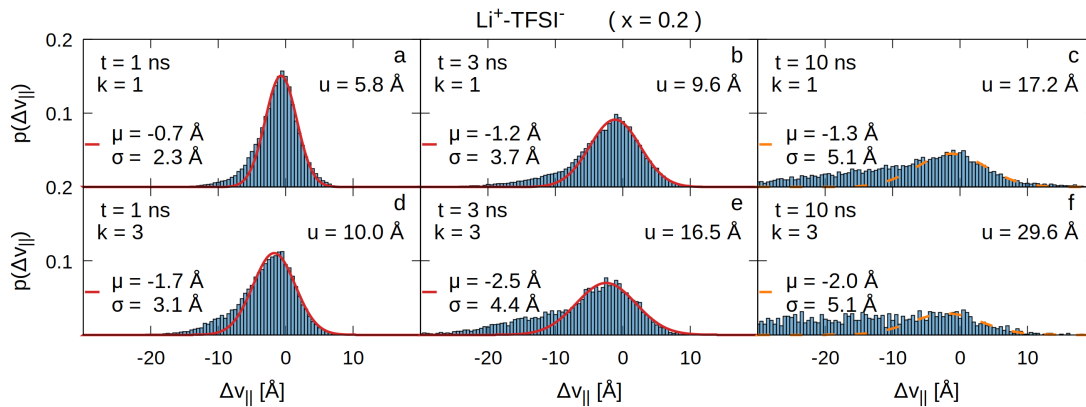
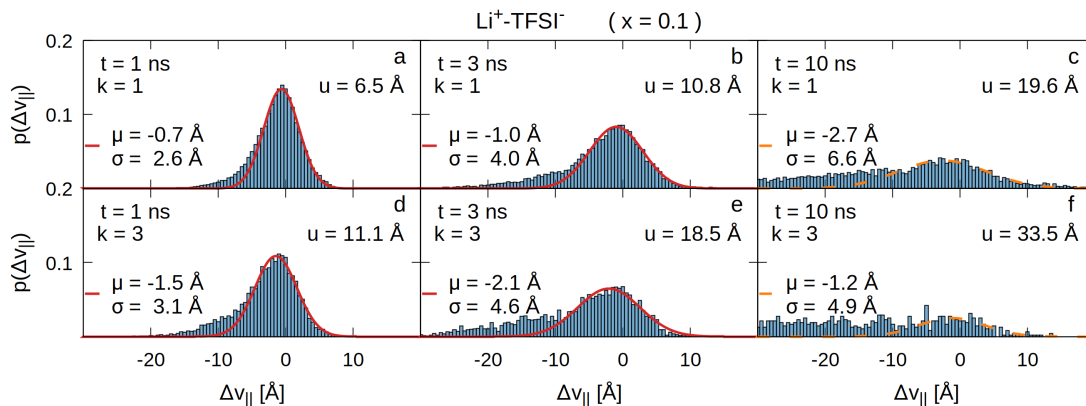
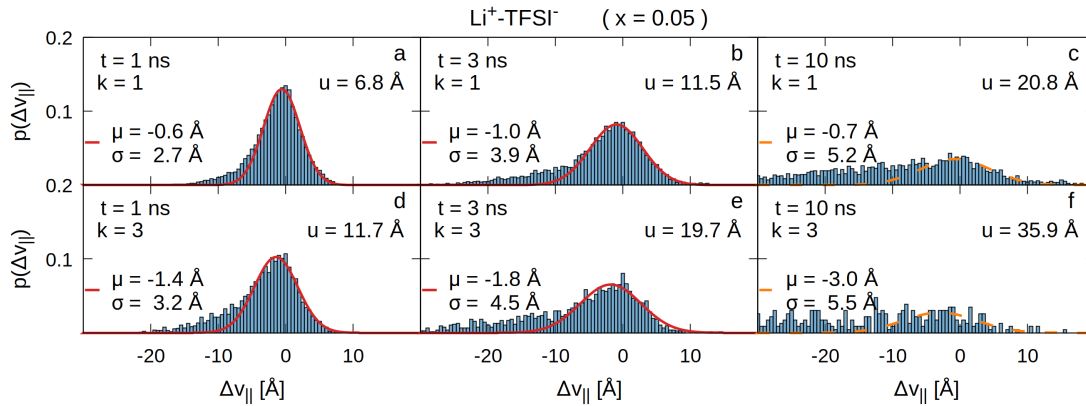
the coupled lithium-anion dynamics from the overlapping distribution of dissociating dynamics, we restrict the left-hand side of the fit interval to $[-\tilde{\sigma} + \tilde{\mu}, \infty)$. The peak is refitted by a Gaussian function (red) $g(x) = a \cdot \exp\left(\frac{(x - \mu)^2}{2\sigma^2}\right)$ with the amplitude a , the expected value μ and variance σ^2 .

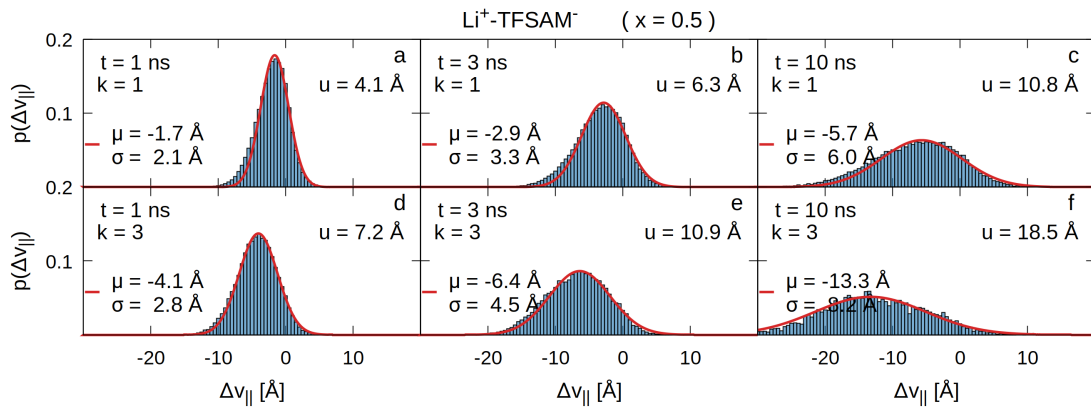
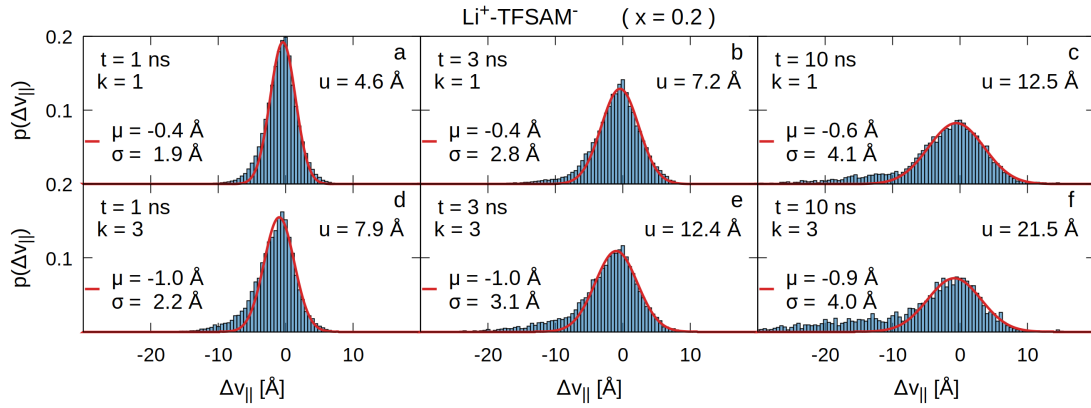
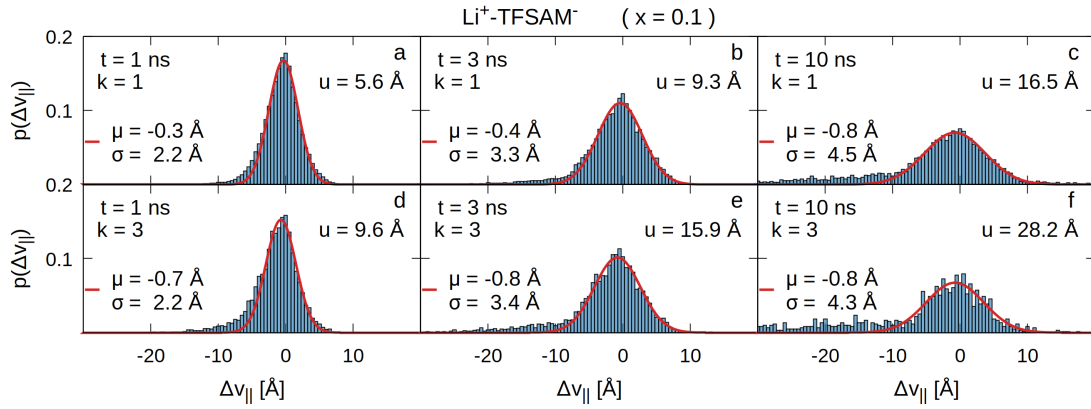
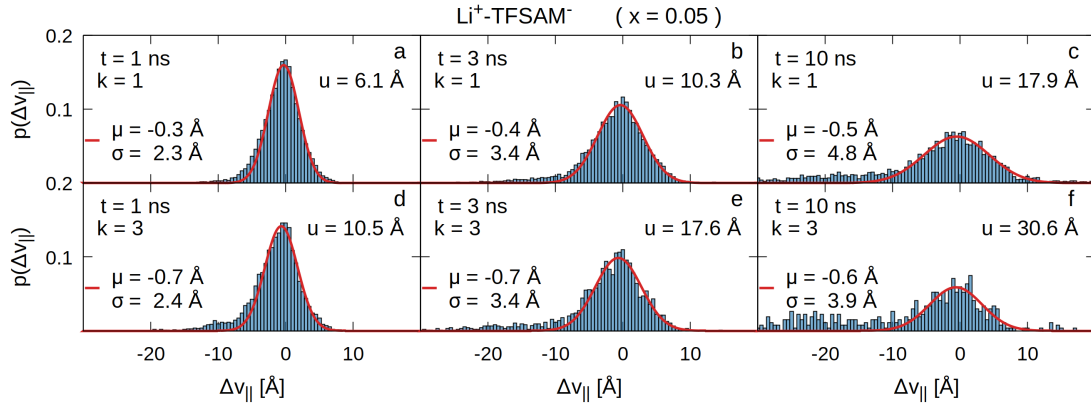
4. Due to the significantly shorter mean residence times $\tau_{\text{Li}^+ - \text{TFSI}^-}$ compared to $\tau_{\text{Li}^+ - \text{TFSAM}^-}$ as discussed in the main manuscript, $p(\Delta v_{\parallel})$ is more disintegrated for TFSI^- at the longest analysed lag time of $t = 10$ ns. Since the fit protocol step (3) fails to expose the peak originating from yet retained coupled dynamics, we fitted the peak manually (dashed orange).

Table S1: Overview of numerically determined lower boundaries u_1^2 for a given distance scaling factor k and upper tolerance thresholds u_r^2 of either 1.3 or 1.5, *i.e.*, 30 or 50 percent tolerance for lithium ions covering a squared distance larger than the target u^2 .

k	u^2	u_1^2	u_r^2
1	$1 \cdot \langle u^2 \rangle$	$u^2 / 1.33$	$u^2 \cdot 1.3$
3	$3 \cdot \langle u^2 \rangle$	$u^2 / 1.22$	$u^2 \cdot 1.3$
1	$1 \cdot \langle u^2 \rangle$	$u^2 / 1.58$	$u^2 \cdot 1.5$
3	$3 \cdot \langle u^2 \rangle$	$u^2 / 1.31$	$u^2 \cdot 1.5$

At the very bottom of Figure S9, $p(\Delta v_{\parallel})$ is additionally shown for the explicit lithium binding sites provided by the respective anion, *i.e.*, TFSI^- (O) and TFSAM^- (N_{out}) at $x = 0.1$.





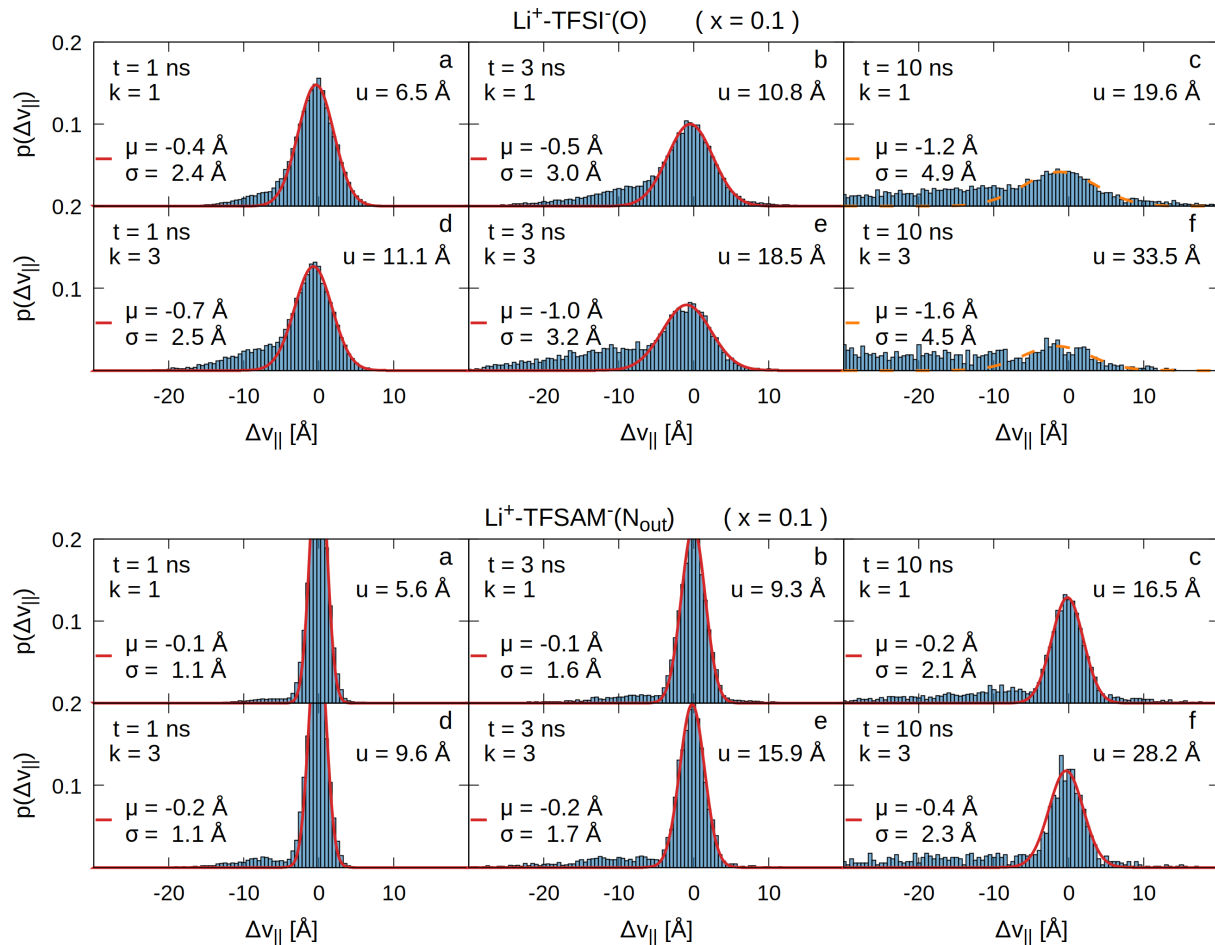


Figure S9: Distributions $p(\Delta v_{\parallel})$ of TFSI^- and TFSAM^- for the subensembles of $u^2 = k \cdot \langle u^2 \rangle$ with $k=1$ (a, b and c) and 3 (d, e and f) for various lag times t and salt concentrations x using an upper threshold tolerance $u_r^2 = 1.5 \cdot k \cdot \langle u^2 \rangle$.

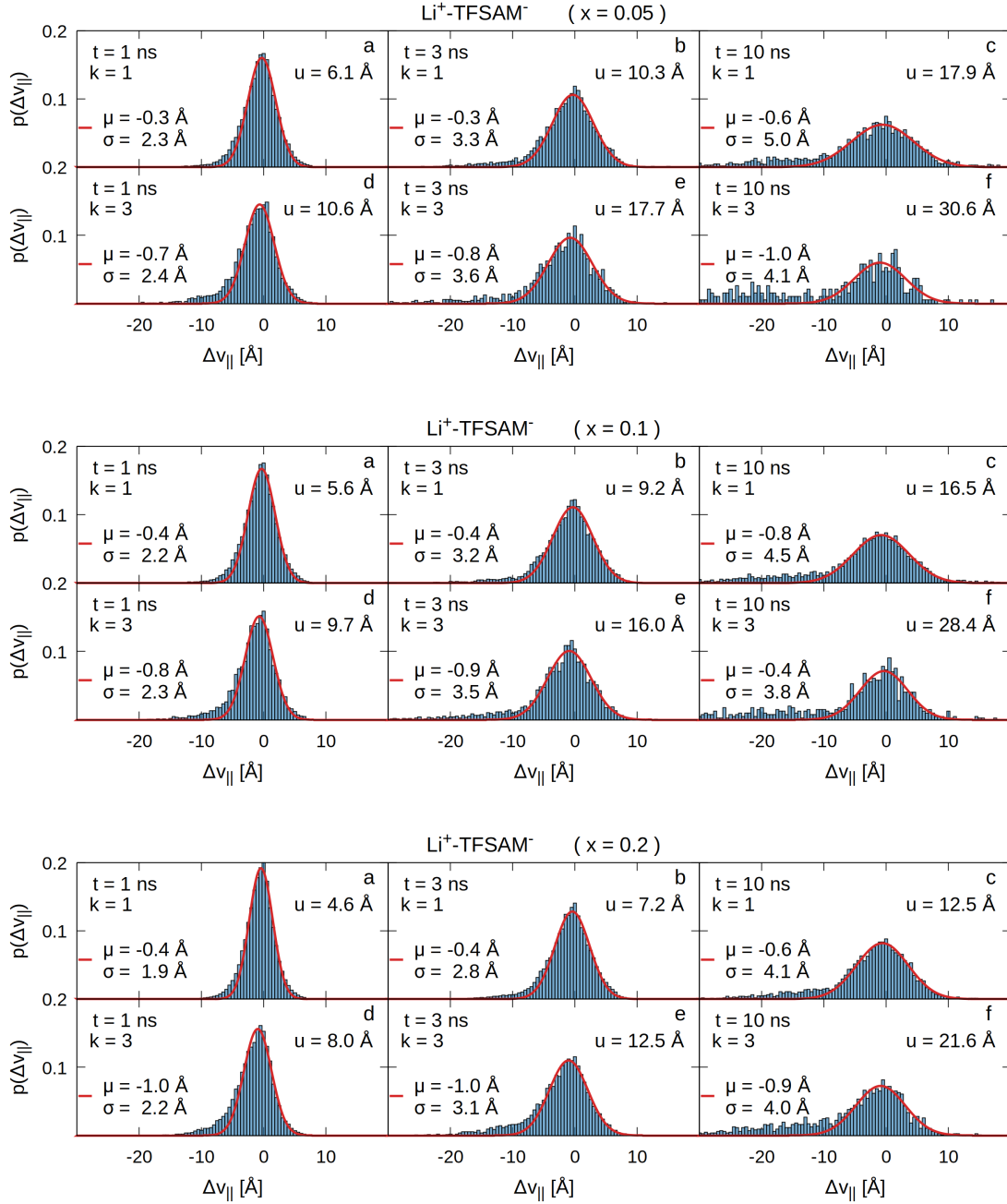


Figure S10: Distributions $p(\Delta v_{||})$ of TFSAM^- at a salt concentration $x=0.1$ for the subensembles of $u^2 = k \cdot \langle u^2 \rangle$ with $k=1$ (a, b and c) and 3 (d, e and f) using an upper threshold tolerance $u_c^2 = 1.3 \cdot k \cdot \langle u^2 \rangle$.

G: Relationship of Gaussian peak parameters μ and σ^2 : A particle-spring-model approach

With the aim to understand why the Gaussian peak centers μ are not positioned at $\Delta v_{\parallel} = 0 \text{ \AA}$ but increasingly shifted for a larger distance scaling factor k , we propose a simple thought experiment:

We idealize a lithium-anion-pair to behave like two particles that are coupled through a harmonic interaction, *i.e.*, connected by a spring. Since we analyse the anion dynamics in the reference frame of the lithium ion, the coupled dynamics reduce, firstly, to one spatial dimension and, secondly, can be conveniently expressed by the system's collective and relative displacements

$$\begin{aligned} X &= \frac{1}{2} \cdot (u + v_{\parallel}) \\ \Gamma &= \frac{1}{2} \cdot (u - v_{\parallel}). \end{aligned} \tag{5}$$

The collective coordinate X thus describes the diffusive motion of the coupled particles whereas the relative coordinate Γ measures the fluctuations of the particles' relative positions. Assuming a normal distribution for both, *i.e.*, $\mathcal{N}(\mu_X, \sigma_X^2)$ and $\mathcal{N}(\mu_{\Gamma}, \sigma_{\Gamma}^2)$, we can deduce the conditional probability distribution $P(v_{\parallel} - u|u)$ that we sampled in the histograms $p(\Delta v_{\parallel})$, starting with $P(v_{\parallel}|u) = P(u, v_{\parallel})/P(u)$:

$$\begin{aligned} P(u, v_{\parallel}) &\propto \mathcal{N}(\mu_X, \sigma_X^2) \cdot \mathcal{N}(\mu_{\Gamma}, \sigma_{\Gamma}^2) \\ &\propto \exp\left(-\frac{1}{2} \frac{(u + v_{\parallel})^2}{4\sigma_X^2}\right) \cdot \exp\left(-\frac{1}{2} \frac{(u - v_{\parallel})^2}{4\sigma_{\Gamma}^2}\right) \\ &\propto \exp\left(-\frac{1}{2} \cdot \frac{1}{4 \cdot AB/(A+B)^2} \left[v_{\parallel} - \underbrace{\frac{A-B}{A+B} \cdot u}_{\mu_{v_{\parallel}}} \right]^2\right) \cdot \exp(\dots) \quad \text{with } A = \sigma_X^2 \quad B = \sigma_{\Gamma}^2 \end{aligned} \tag{6}$$

Therefore, it holds for $\mu \doteq \mu_{\Delta v_{\parallel}}$:

$$\begin{aligned}
\mu &= \mu_{v_{\parallel}} - u \\
&= \frac{\sigma_X^2 - \sigma_{\Gamma}^2}{\sigma_X^2 + \sigma_{\Gamma}^2} \cdot u - u \\
&= -2 \cdot \frac{\sigma_{\Gamma}^2}{\sigma_{\Gamma}^2 + \sigma_X^2} \cdot u
\end{aligned} \tag{7}$$

The variances σ_X^2 and σ_{Γ}^2 are related to the observables $\langle u^2 \rangle$ and $\sigma^2 \doteq \sigma_{\Delta v_{\parallel}}^2$ which are accessible through our analysis:

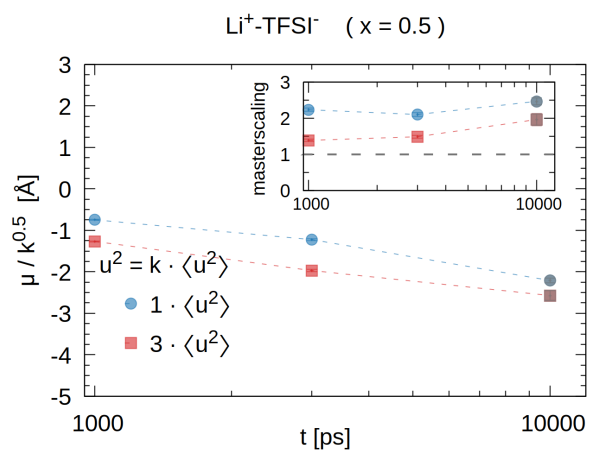
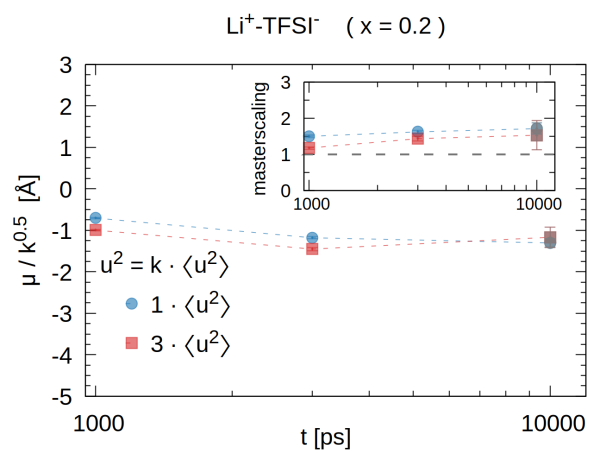
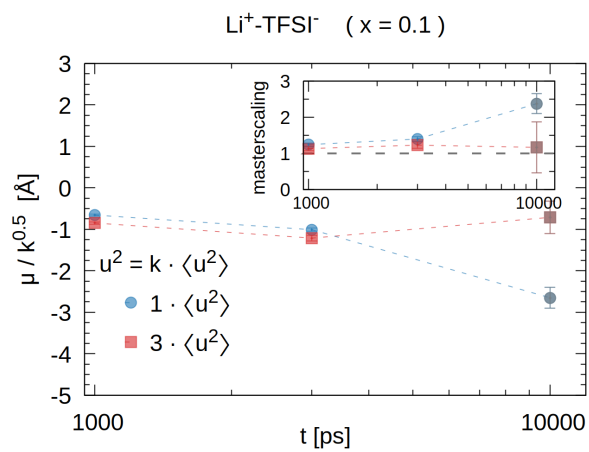
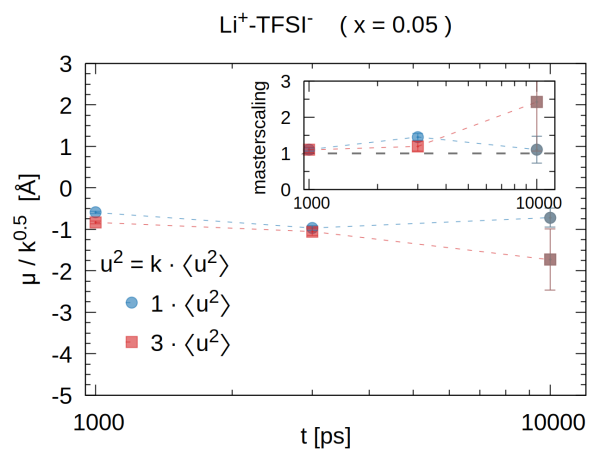
$$\sigma_u^2 = \langle u^2 \rangle - \underbrace{\langle u \rangle^2}_0 \doteq \sigma_X^2 + \sigma_{\Gamma}^2 \quad \wedge \quad \sigma_{\Gamma}^2 = \frac{1}{4} \sigma^2. \tag{8}$$

Consequently, we can rewrite Equation S7:

$$\begin{aligned}
\mu &= -\frac{u}{2} \cdot \frac{\sigma^2}{\langle u^2 \rangle} \\
&= -\frac{\sqrt{k}}{2} \cdot \frac{\sigma^2}{\sqrt{\langle u^2 \rangle}} \quad \text{for} \quad u^2 = k \cdot \langle u^2 \rangle.
\end{aligned} \tag{9}$$

The expression "masterscaling" in the main manuscript refers to a simple rearrangement of Equation S9 :

$$1 = -2 \cdot \frac{\mu \sqrt{\langle u^2 \rangle}}{\sqrt{k} \sigma^2}. \tag{10}$$



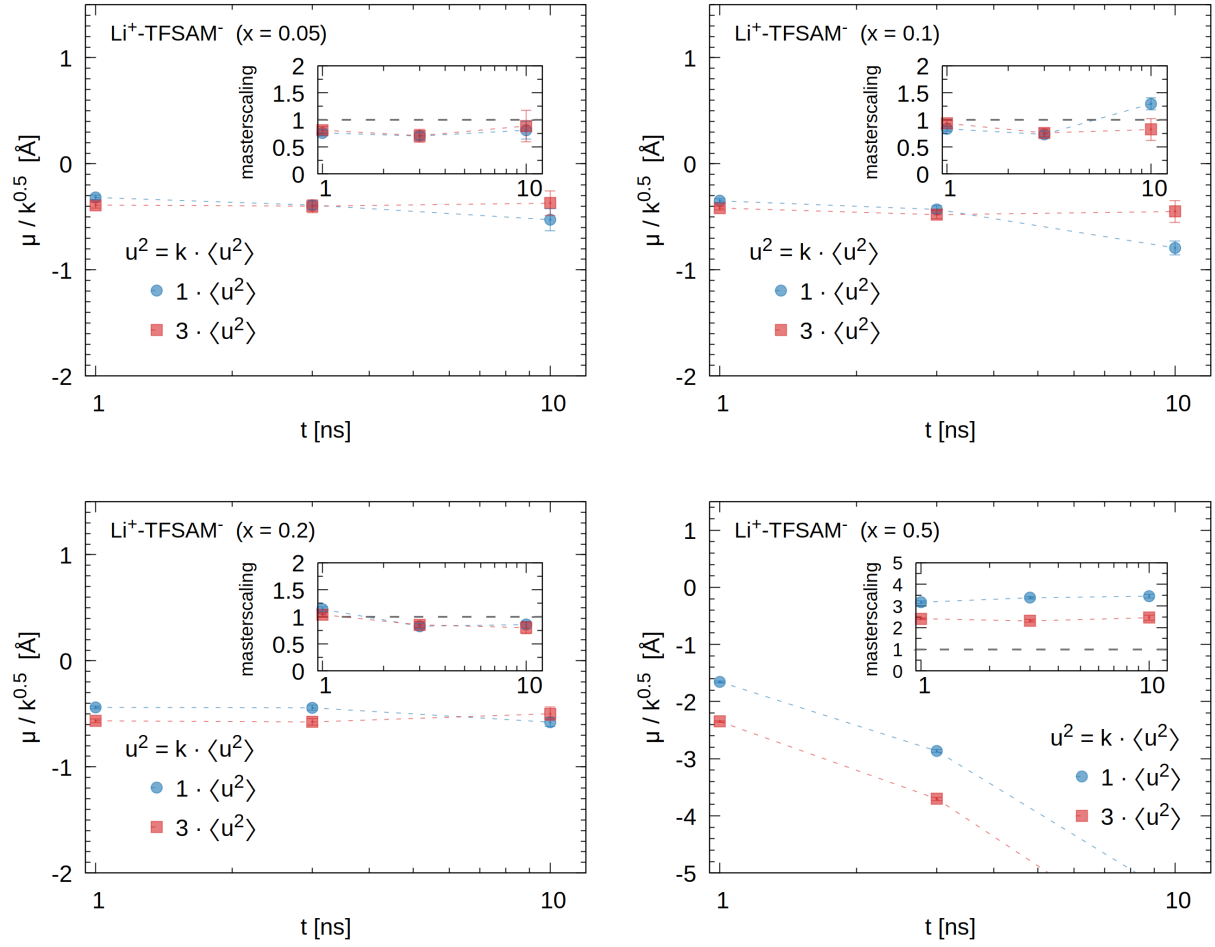


Figure S11: Gaussian peak positions $\mu(t)$ divided by the square root of the distance scaling factor k . Inset: Masterscaling of the Gaussian peak parameters μ and σ^2 to 1 according to Equation S10. The data points relying on the manually performed Gaussian fits are highlighted in grey. The data points are based on measurements employing an upper threshold tolerance $u_r^2 = 1.5 \cdot k \cdot \langle u^2 \rangle$.

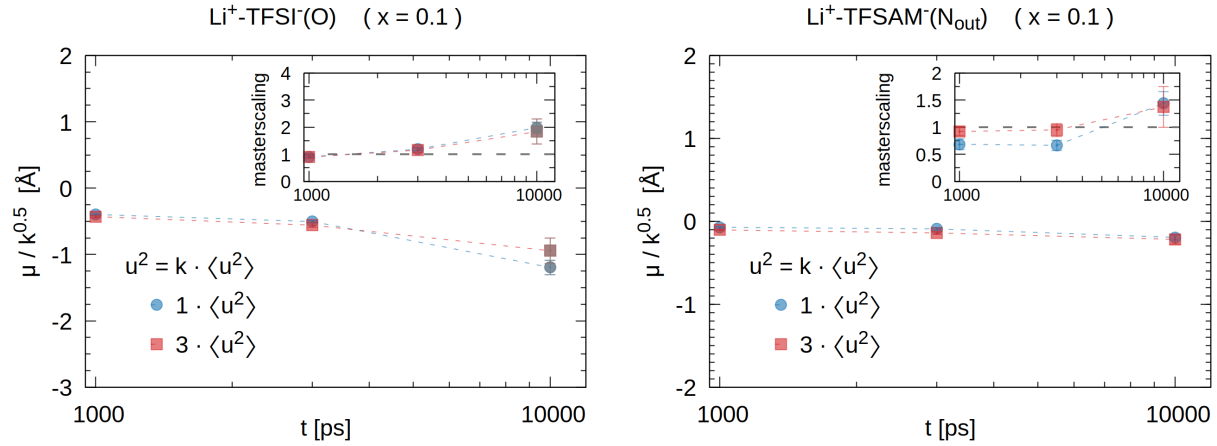


Figure S12: Scaling relations exemplary for the direct anion binding sites TFSI⁻(O) and TFSAM⁻(N_{mid}) at a low salt content of $x = 0.1$: Gaussian peak positions $\mu(t)$ divided by the square root of the distance scaling factor k . Inset: Masterscaling of the Gaussian peak parameters μ and σ^2 to 1 according to Equation S10. The data points relying on the manually performed Gaussian fits are highlighted in grey. The data points are measured using an upper threshold tolerance $u_r^2 = 1.5 \cdot k \cdot \langle u^2 \rangle$.

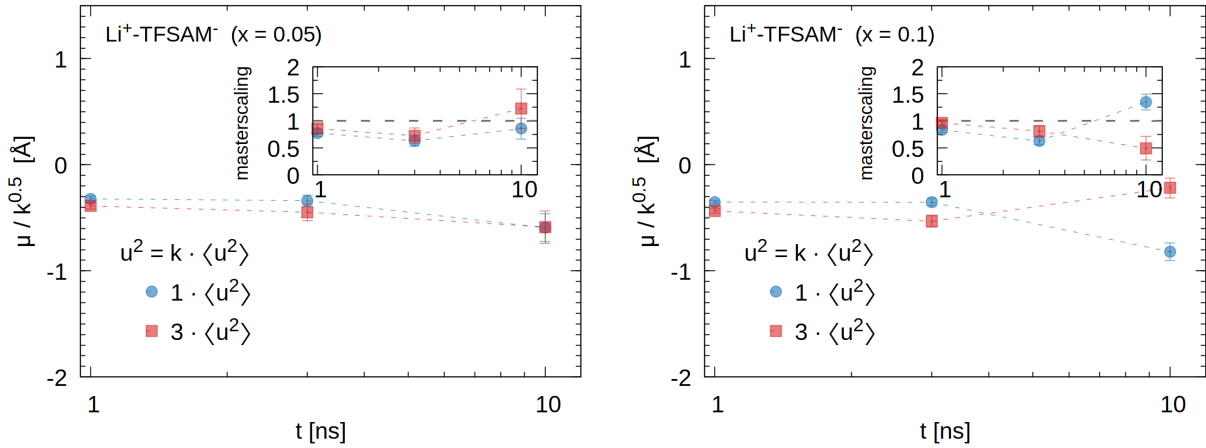
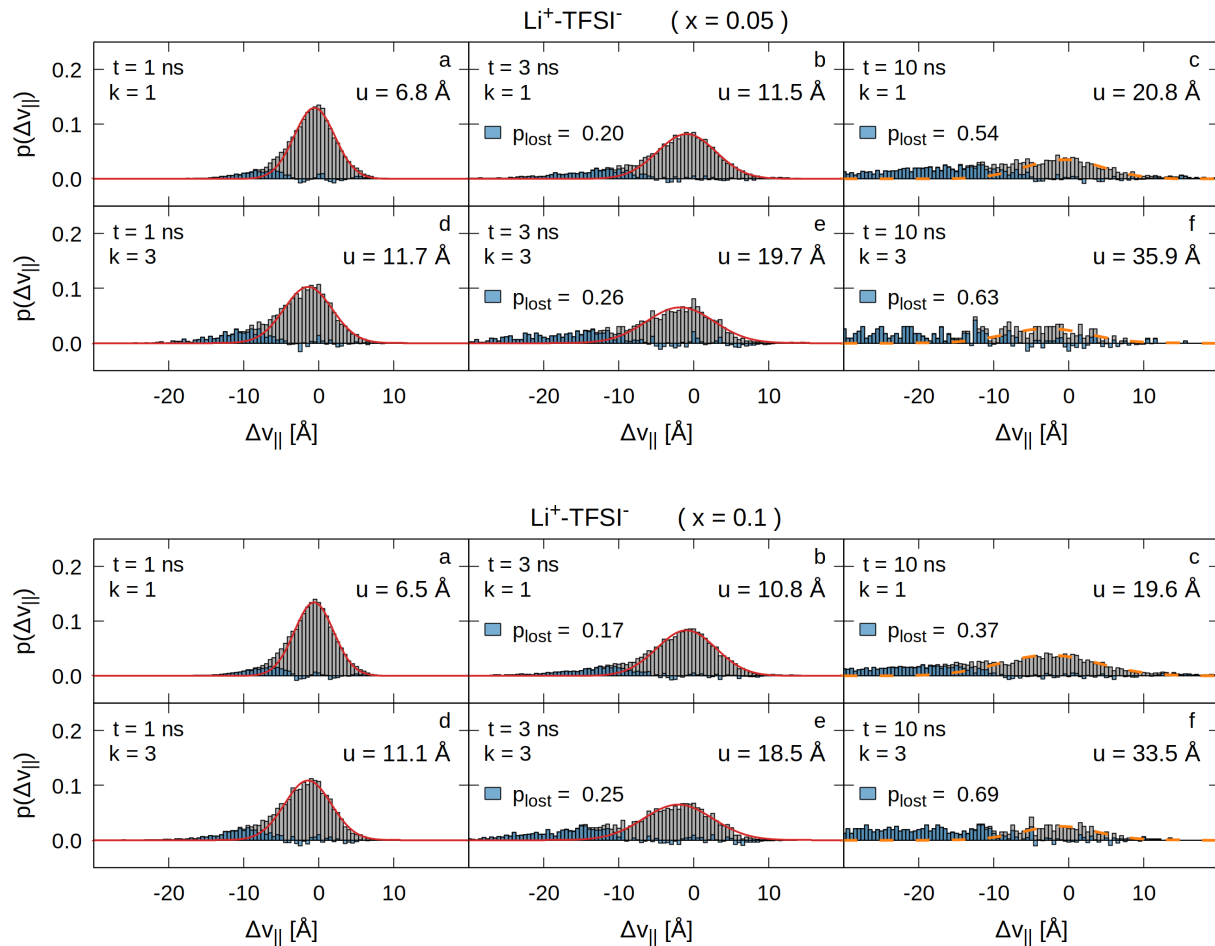


Figure S13: Scaling relations exemplary for the TFSAM⁻-based mixtures for $x = 0.05$ and 0.1 using an upper threshold tolerance $u_r^2 = 1.3 \cdot k \cdot \langle u^2 \rangle$.

H: Quantification of dynamically decoupled anions p_{lost}

The ratio of dynamically decoupled anions is estimated from the relative displacement distribution by subtracting the Gaussian peak fit $\mathcal{N}(\mu, \sigma^2)$ from the histogram data $p(\Delta v_{\parallel})$ and summing up the remaining counts: $\int d\Delta v_{\parallel} (p(\Delta v_{\parallel}) - \mathcal{N}(\mu, \sigma^2)) \doteq p_{\text{lost}}$. The part of the histogram which is attributed to p_{lost} is highlighted in blue.



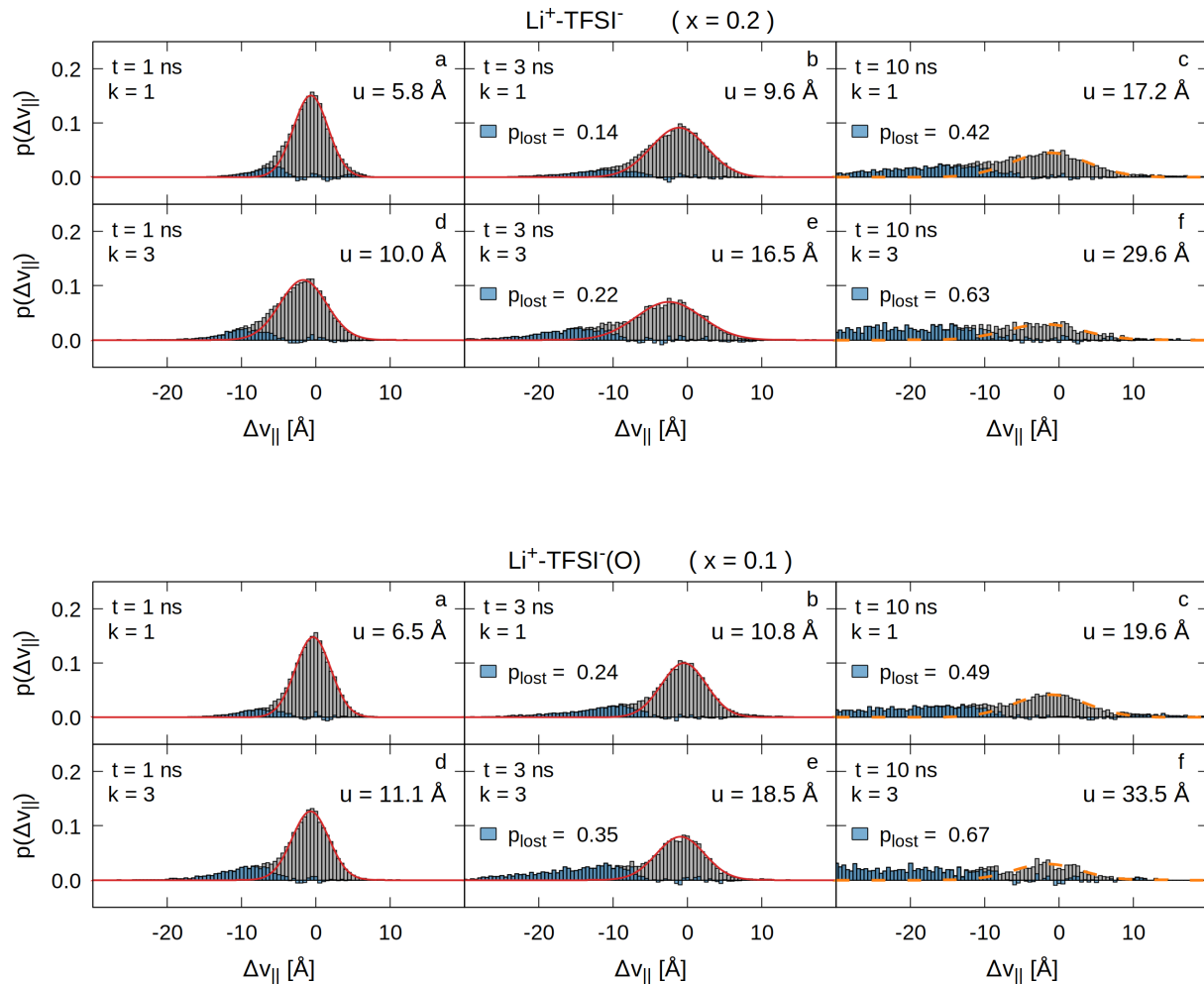
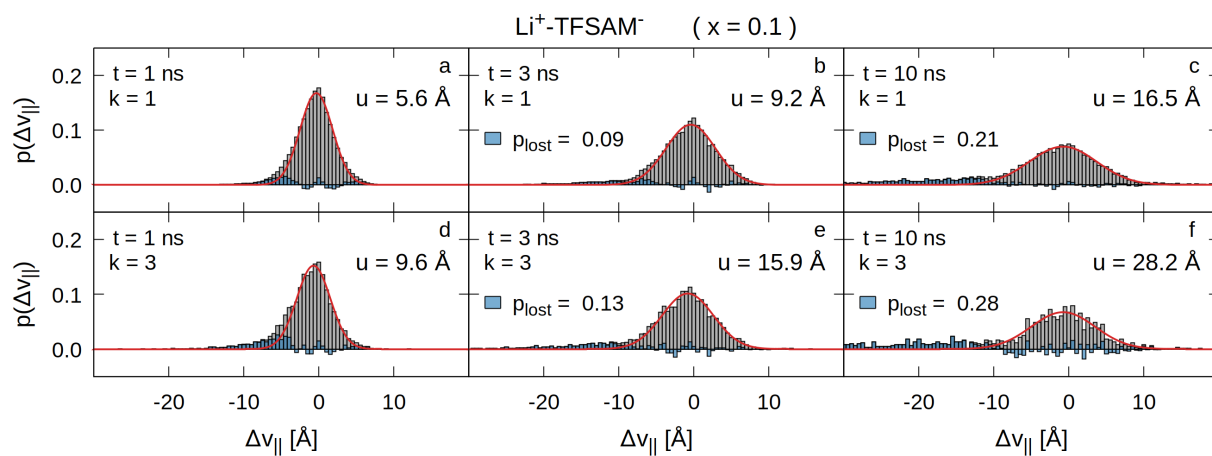
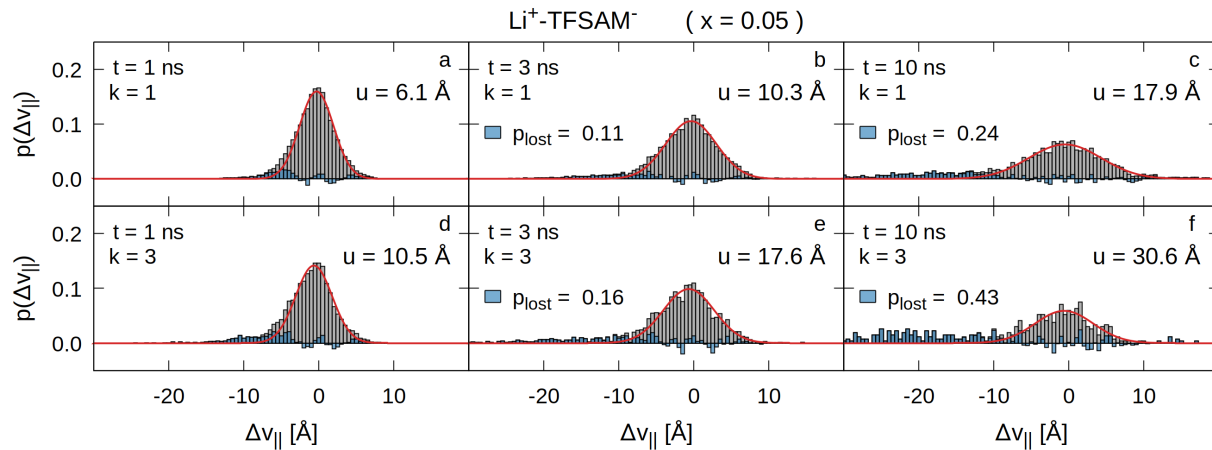


Figure S14: Estimation of the amount p_{lost} of dynamically decoupled TFSI⁻ shell anions at different lag times t , lithium squared displacements $k \cdot \langle u^2 \rangle$ and various salt contents x . Since the distributions of coupled (Gaussian peak) and decoupled (tail) dynamics overlap considerably at the shortest analysed lag time of $t = 1$ ns, a precise quantitative estimate of p_{lost} is not feasible through this procedure.



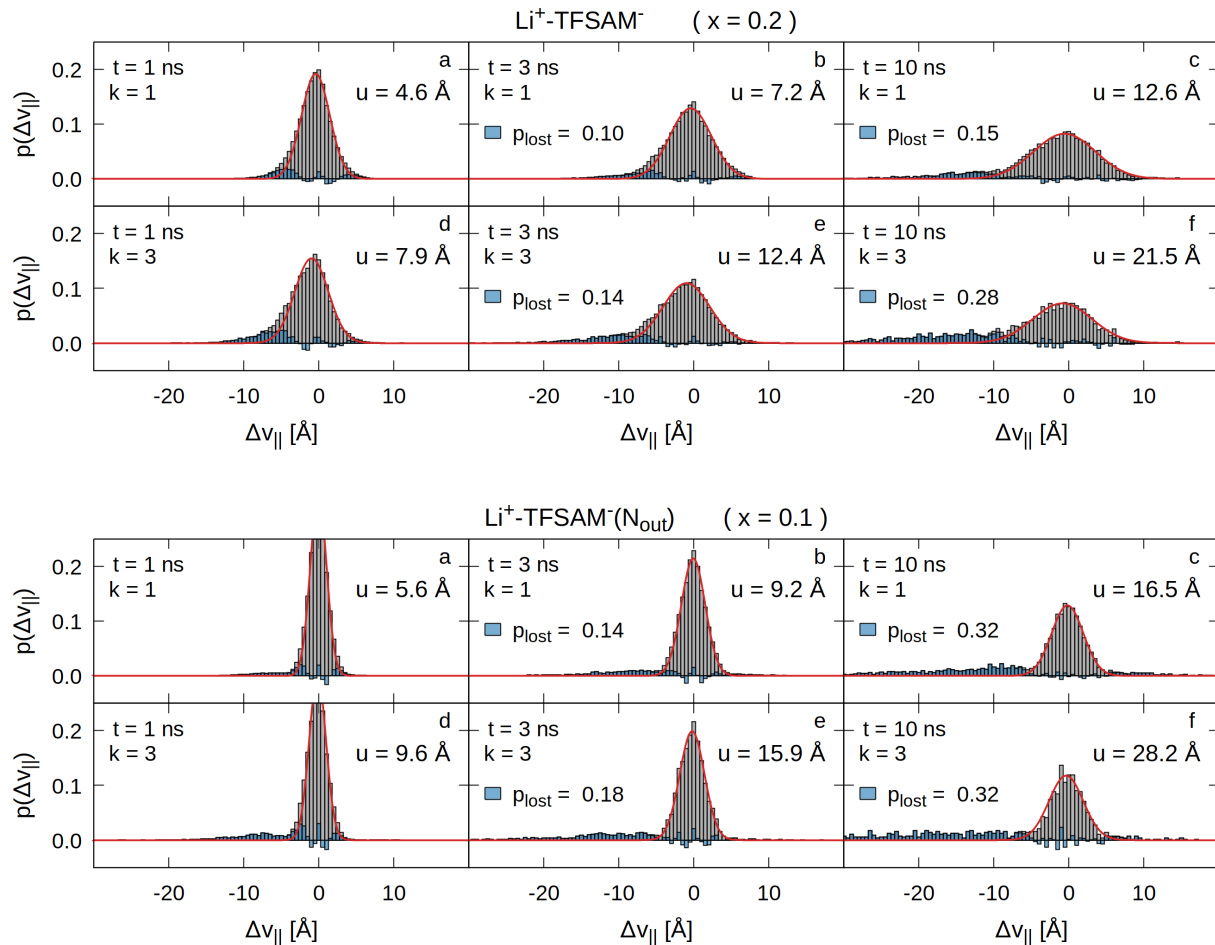


Figure S15: Estimation of the amount p_{lost} of dynamically decoupled TFSAM⁻ shell anions at different lag times t , lithium squared displacements $k \cdot \langle u^2 \rangle$ and various salt contents x . Since the distributions of coupled (Gaussian peak) and decoupled (tail) dynamics overlap considerably at the shortest analysed lag time of $t = 1$ ns, a precise quantitative estimate of p_{lost} is not feasible through this procedure.

I: LCF λ as a function of squared lithium displacement $u^2(t)$

The Li^+ coupling factor λ , which measures the extent to which an initially lithium-bound anion follows the dynamics of this very Li^+ , is binned according to the squared displacement u^2 of this Li^+ . The data sets are generated by averaging over multiple individual blocks, *e.g.*, the 400 ns trajectories are divided into 130 blocks to evaluate the lag time $t = 3$ ns.

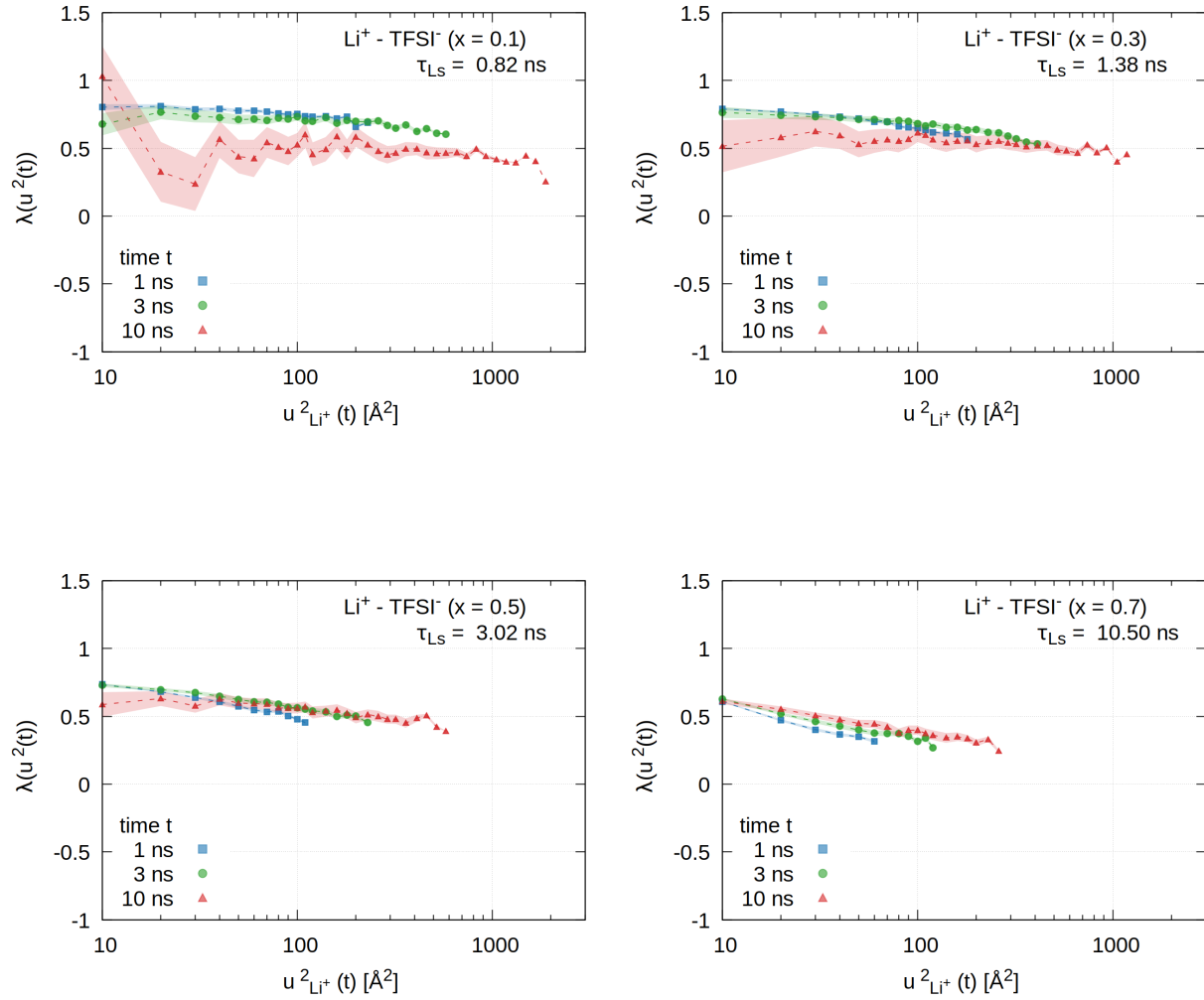


Figure S16: Coupling of anion motion to lithium dynamics measured via λ as a function of $u^2(t)_{\text{Li}^+}$ exemplary for the lithium salt fractions $x = 0.1, 0.3, 0.5$ and 0.7 in the TFSI⁻-containing mixtures.

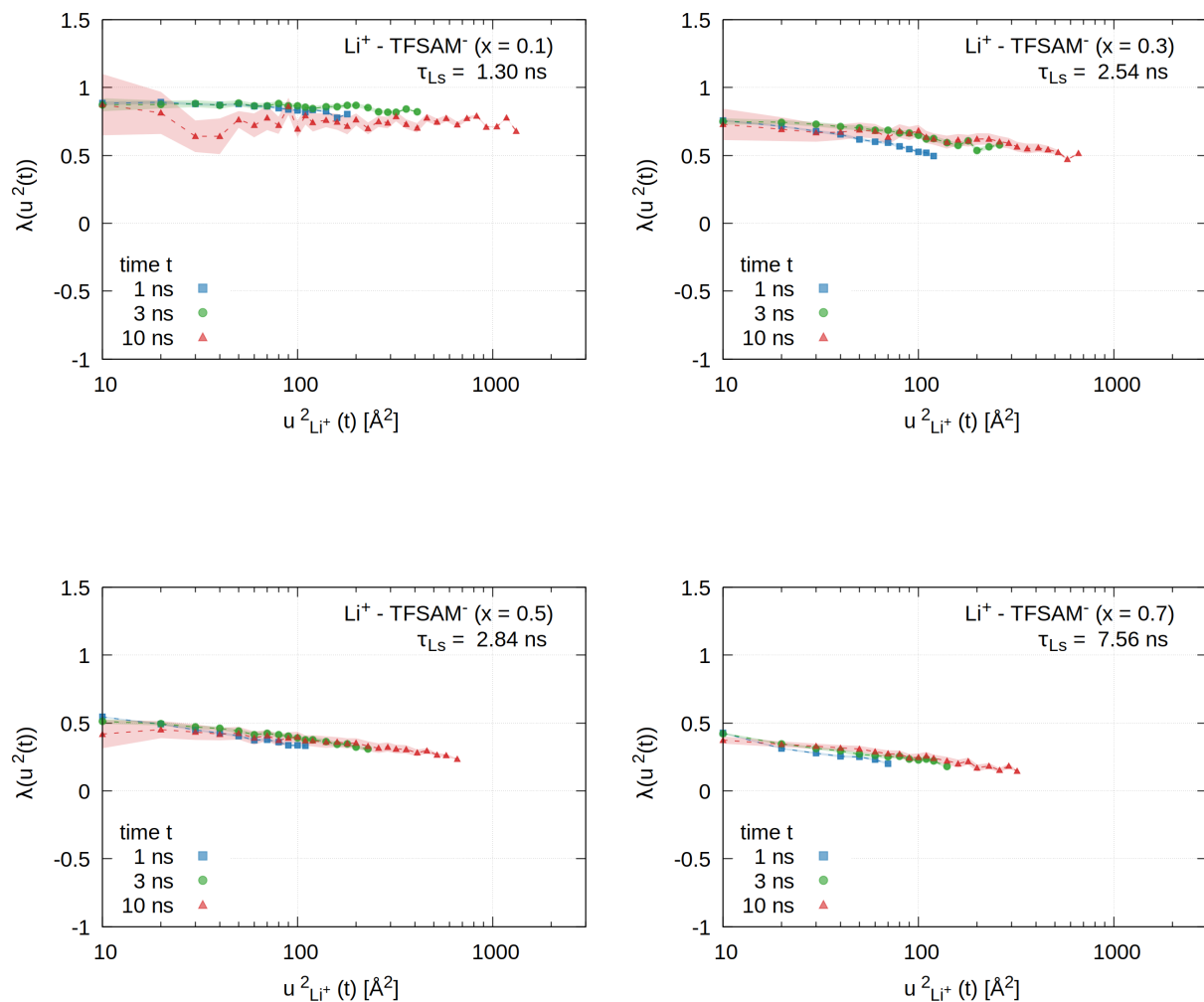


Figure S17: Coupling of anion motion to lithium dynamics measured via λ as a function of $u^2(t)_{\text{Li}^+}$ exemplary for the lithium salt fractions $x = 0.1, 0.3, 0.5$ and 0.7 in the TFSAM⁻-containing mixtures.

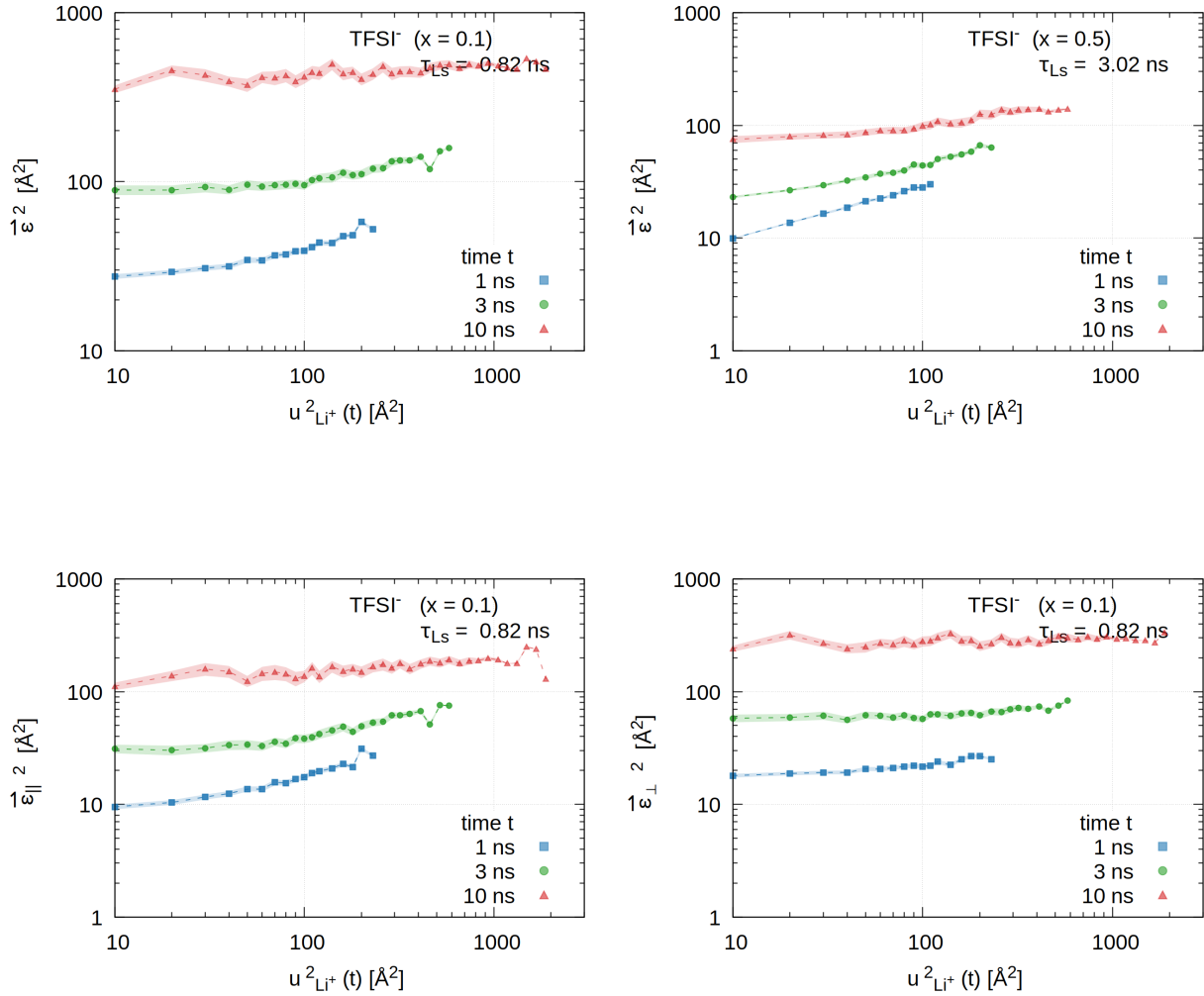
J: $\vec{\epsilon}^2$, $\vec{\epsilon}_{\parallel}^2$ and $\vec{\epsilon}_{\perp}^2$ as a function of squared lithium displacement $u^2(t)$

One may split the random motion $\vec{\epsilon}$ of an anion into contributions parallel and orthogonal to the lithium path direction $\hat{r} = \vec{u} / |\vec{u}|$, which can be computed as

$$\begin{aligned}\vec{\epsilon} &= \vec{v} - \lambda_{u^2} \cdot \vec{u} \\ \vec{\epsilon}_{\parallel} &= (\vec{\epsilon} \cdot \hat{r}) \cdot \hat{r} \\ \vec{\epsilon}_{\perp} &= \vec{\epsilon} - \vec{\epsilon}_{\parallel}.\end{aligned}\tag{11}$$

λ_{u^2} corresponds to the definition in Equation 7 in the main manuscript

$$\lambda(u^2, t) = \frac{\langle \vec{u}_i \cdot \vec{v}_j^i \rangle_{u^2, t}}{u^2} = \frac{\langle v_{\parallel} \rangle_{u^2, t}}{u}, \text{ i.e., the data shown in Figures S16 and S17.}$$



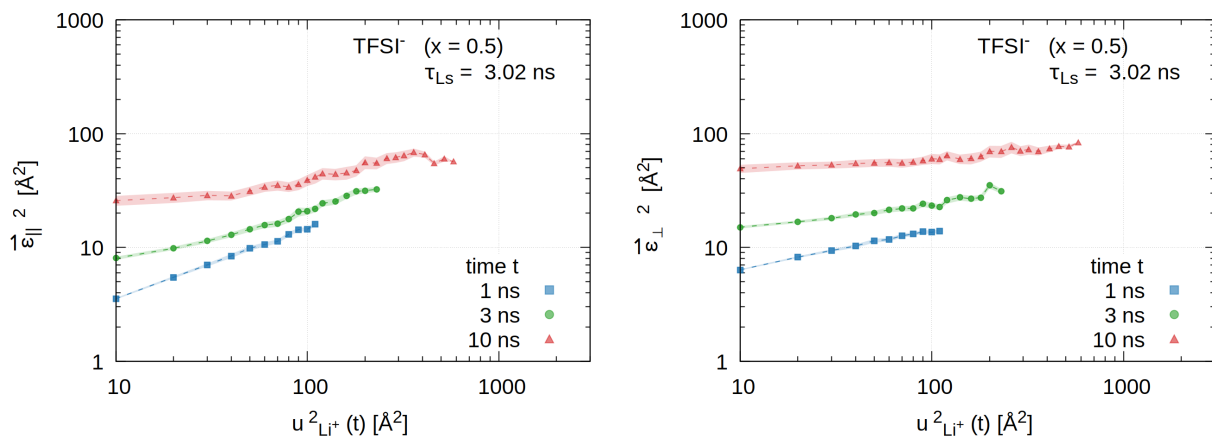
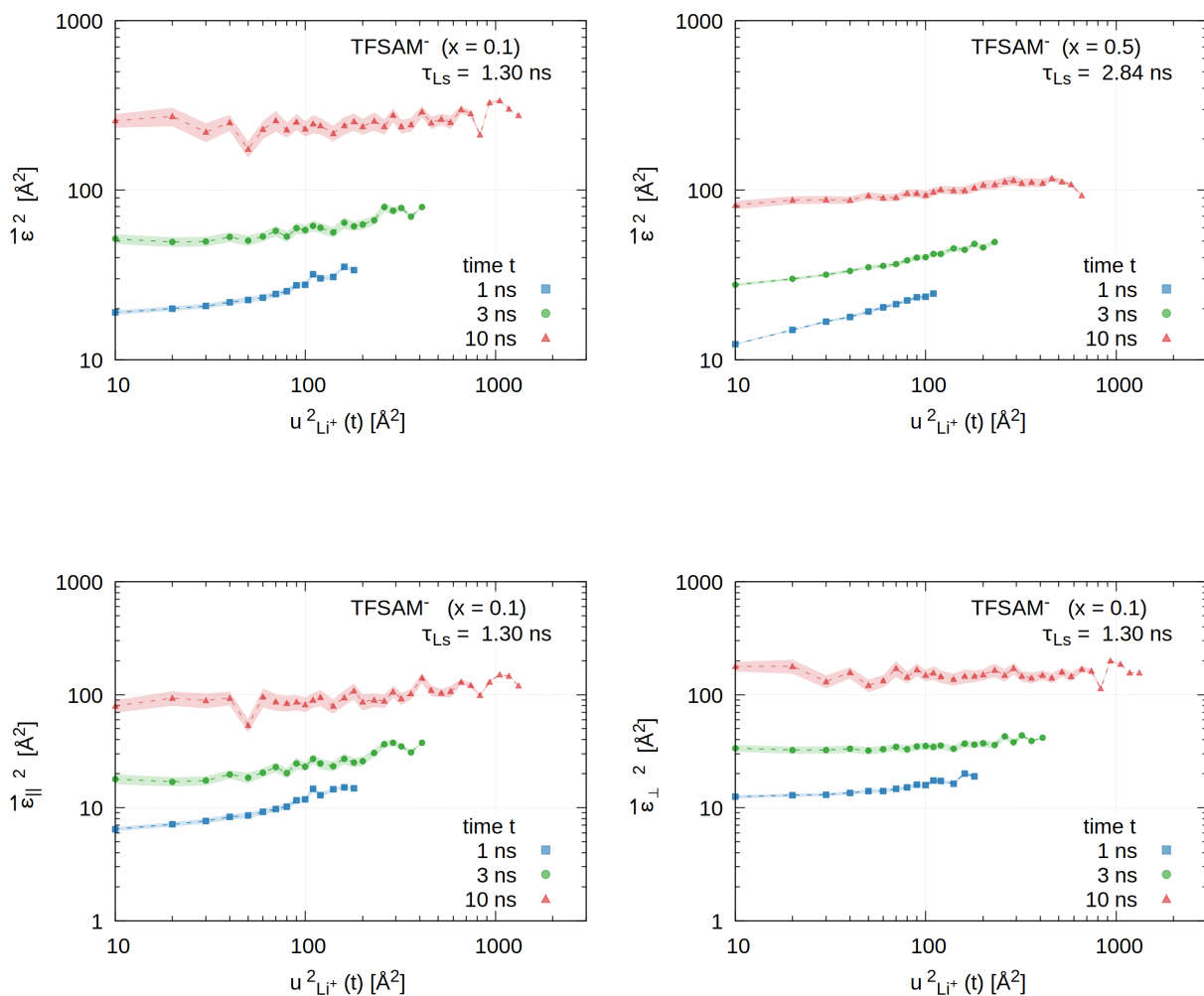


Figure S18: Variances $\bar{\epsilon}^2$, $\bar{\epsilon}_{\parallel}^2$ and $\bar{\epsilon}_{\perp}^2$ as a function of $u^2(t)_{Li^+}$ for TFSI⁻ exemplary for salt contents $x = 0.1$ and $x = 0.5$.



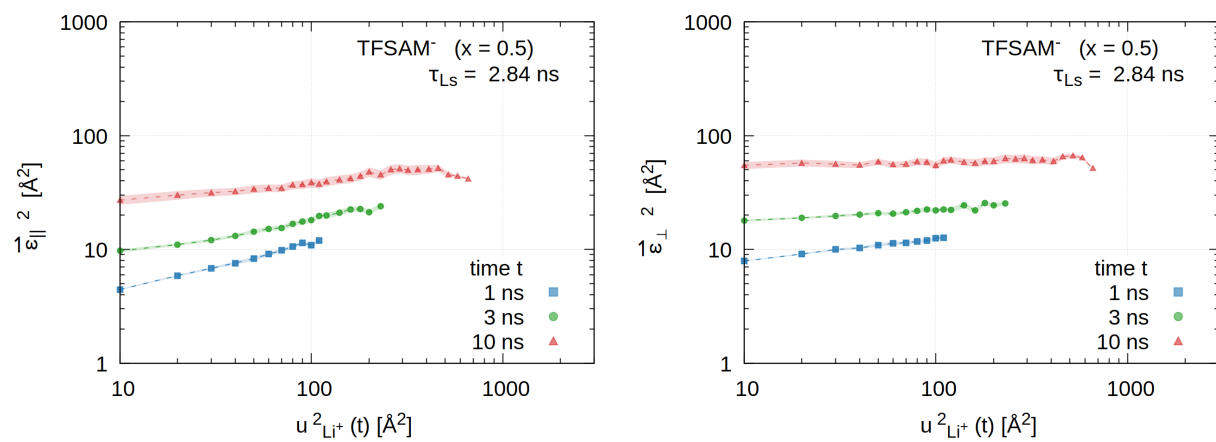
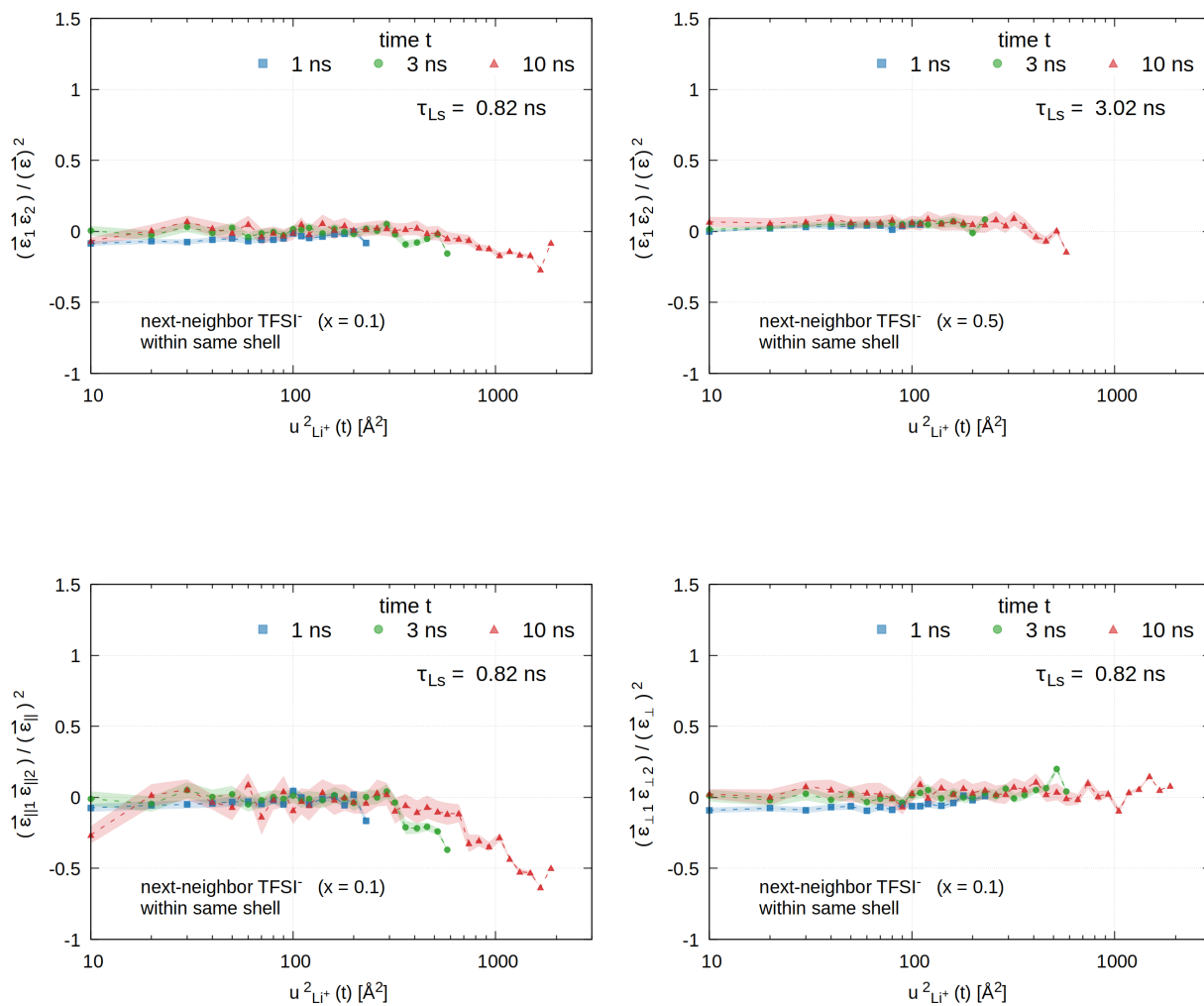


Figure S19: Variances $\bar{\epsilon}^2$, $\bar{\epsilon}_{||}^2$ and $\bar{\epsilon}_{\perp}^2$ as a function of $u^2(t)_{Li^+}$ for TFSAM⁻ exemplary for salt contents $x = 0.1$ and $x = 0.5$.

K: Correlation of the random motion of next-neighbor anions in a solvation shell

To investigate the interaction between two initially adjacent anions anion_1 and anion_2 in a lithium solvation shell, we compute the correlation $(\vec{\epsilon}_1 \cdot \vec{\epsilon}_2) / (\epsilon^2)$ as well as quantify the contributions parallel $(\vec{\epsilon}_{1,\parallel} \cdot \vec{\epsilon}_{2,\parallel}) / (\epsilon_{\parallel}^2)$ and orthogonal $(\vec{\epsilon}_{1,\perp} \cdot \vec{\epsilon}_{2,\perp}) / (\epsilon_{\perp}^2)$ to the lithium pathway.



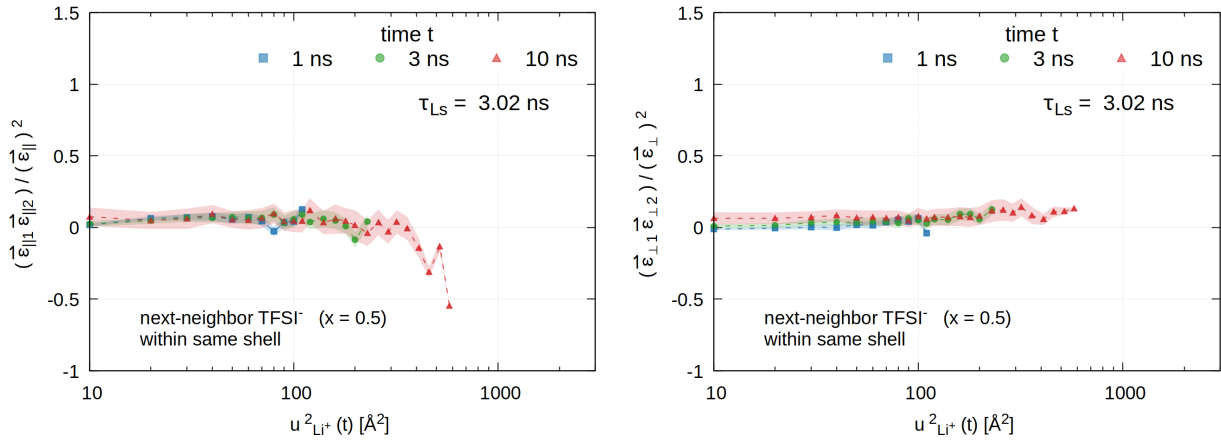
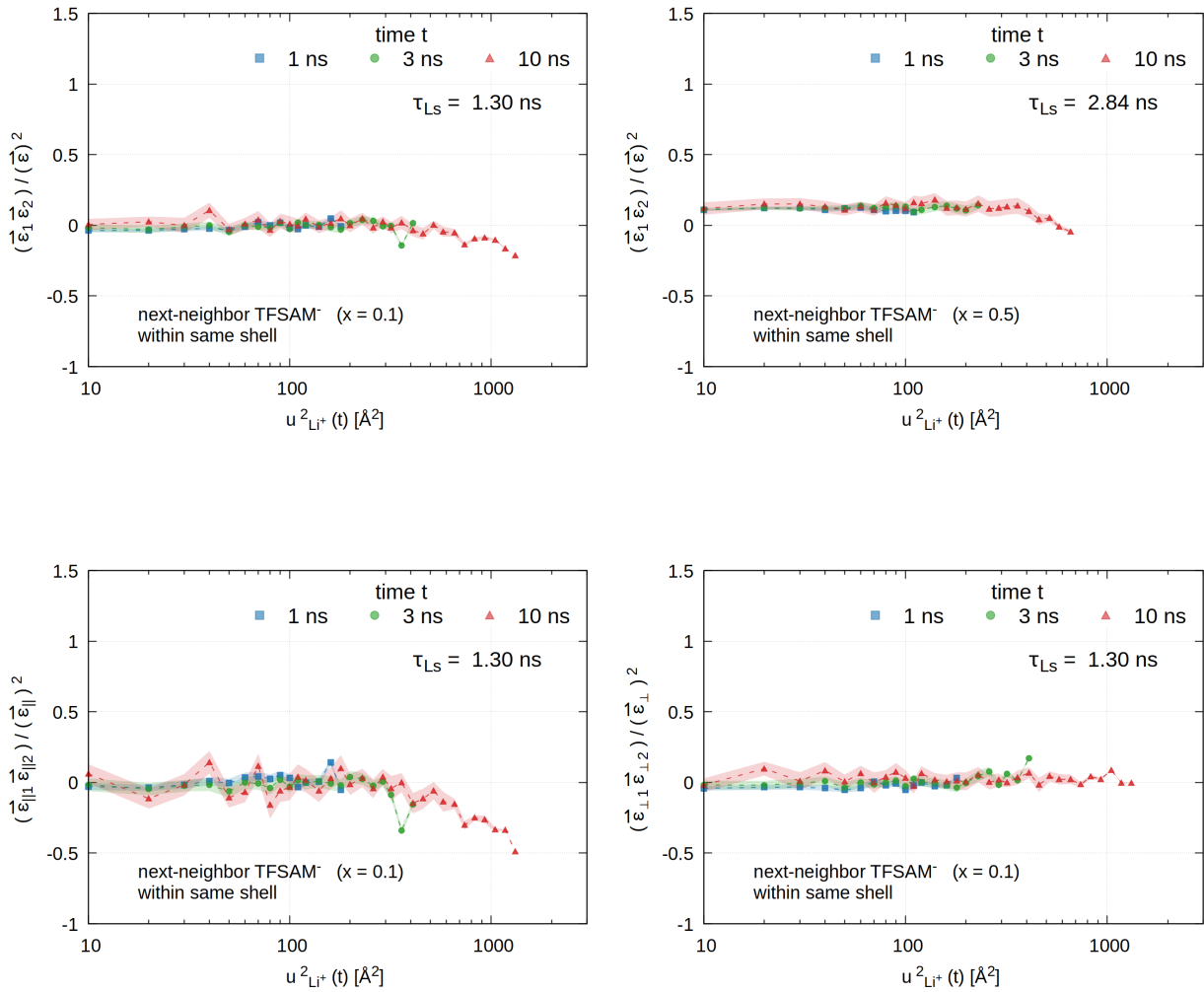


Figure S20: Correlations of initial next-neighbor shell anions TFSI_1^- and TFSI_2^- as a function of $u^2(t)_{\text{Li}^+}$ exemplary for salt contents $x=0.1$ and $x=0.5$.



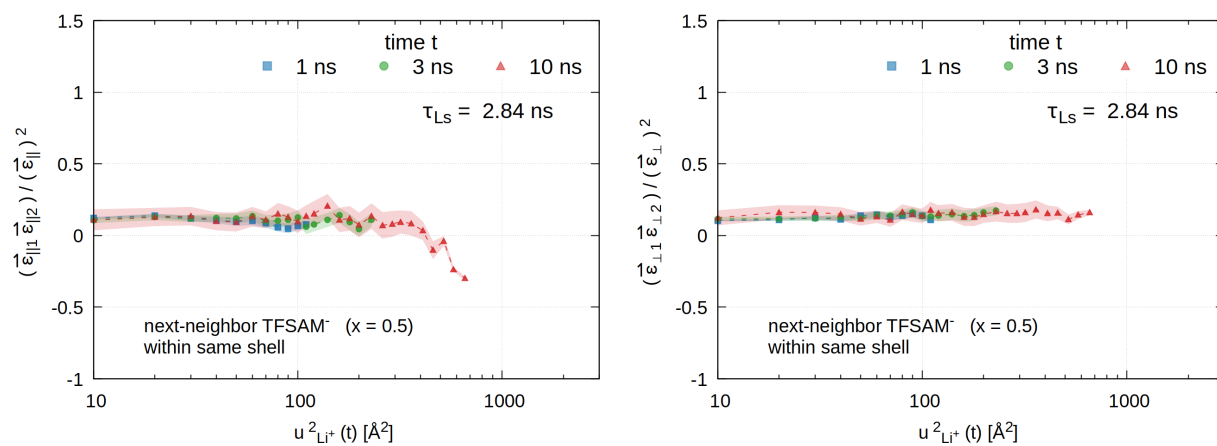


Figure S21: Correlations of initial next-neighbor shell anions TFSAM₁⁻ and TFSAM₂⁻ as a function of $u^2(t)_{Li^+}$ exemplary for salt contents $x = 0.1$ and $x = 0.5$.

L: LCF λ as a function of time t

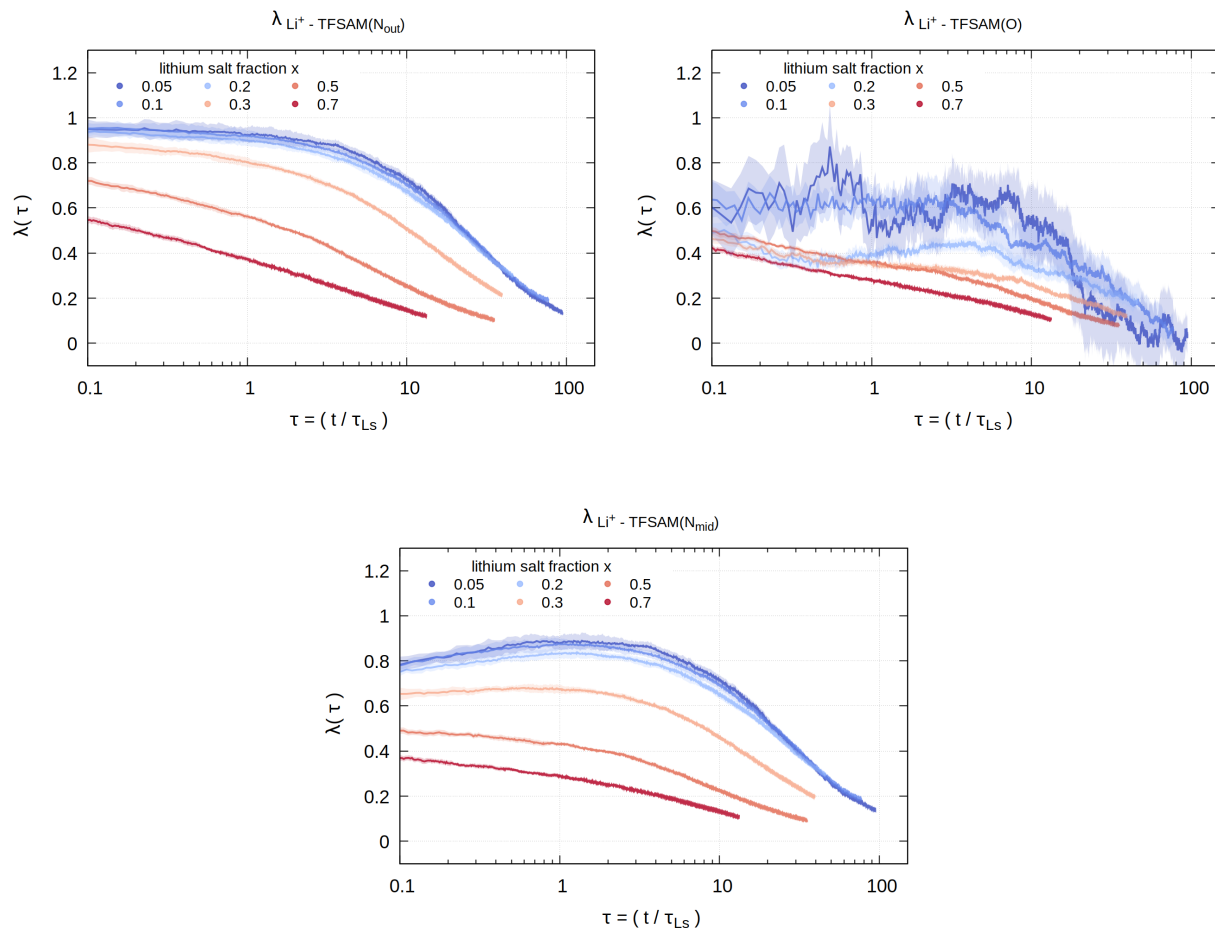


Figure S22: Time dependence of LCF λ for Li^+ to different binding sites provided by TFSAM^- , *i.e.*, the outer nitrogen atoms N_{out} (top left) or the oxygen atoms (top right). Using the second minimum position of $g_{\text{Li}^+-\text{N}_{\text{mid}}}$ as a cutoff distance to determine $\text{Li}^+ - \text{TFSAM}^-$ -binding as discussed in the manuscript, contains all possible coordination geometries. For a structurally equivalent comparison with TFSI^- , we analyse the LCF of Li^+ and the middle nitrogen atoms N_{mid} in the initial TFSAM^- solvation cage. To compare the time dependence of λ for different salt contents x , t is scaled by the characteristic self diffusion time τ_{LS} (see Figure 5B) of each electrolyte composition.

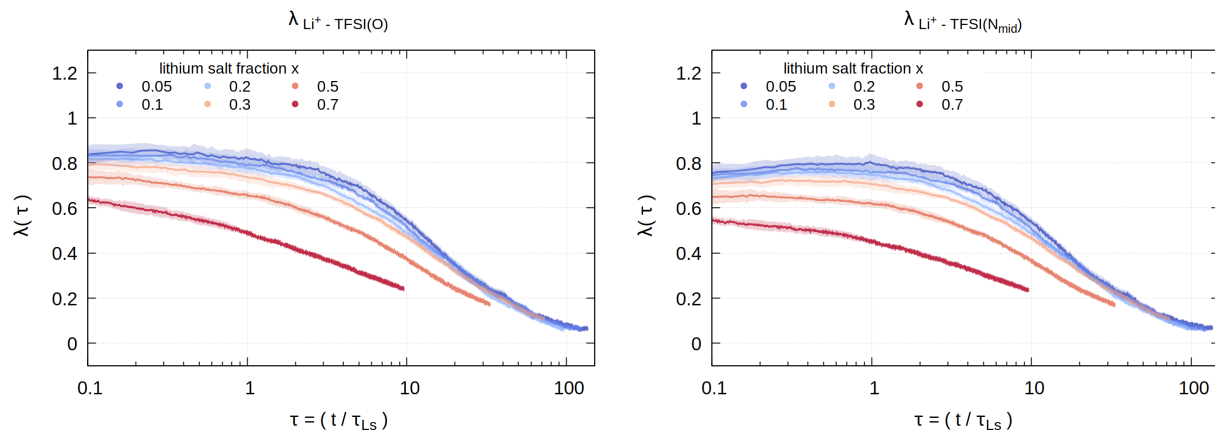


Figure S23: Time dependence of LCF λ for Li^+ to the oxygen atoms (top left) of TFSI^- . Employing the second minimum position of $g_{\text{Li}^+ - \text{N}_{\text{mid}}}$ as a cutoff distance to determine $\text{Li}^+ - \text{TFSI}^-$ -binding as discussed in the main manuscript allows for a structurally equivalent comparison with TFSAM^- . Thus, we analyse the LCF of Li^+ and the middle nitrogen atoms N_{mid} in the initial TFSI^- solvation cage. To compare the time dependence of λ for different salt contents x , t is scaled by the characteristic self diffusion time τ_{Ls} (see Figure 5A) of each electrolyte composition.

M: Comparison of λ , λ_1 , λ_2 and Λ_2 as a function of salt content x for characteristic times of $3 \cdot \tau_{Ls}$ and $5 \cdot \tau_{Ls}$

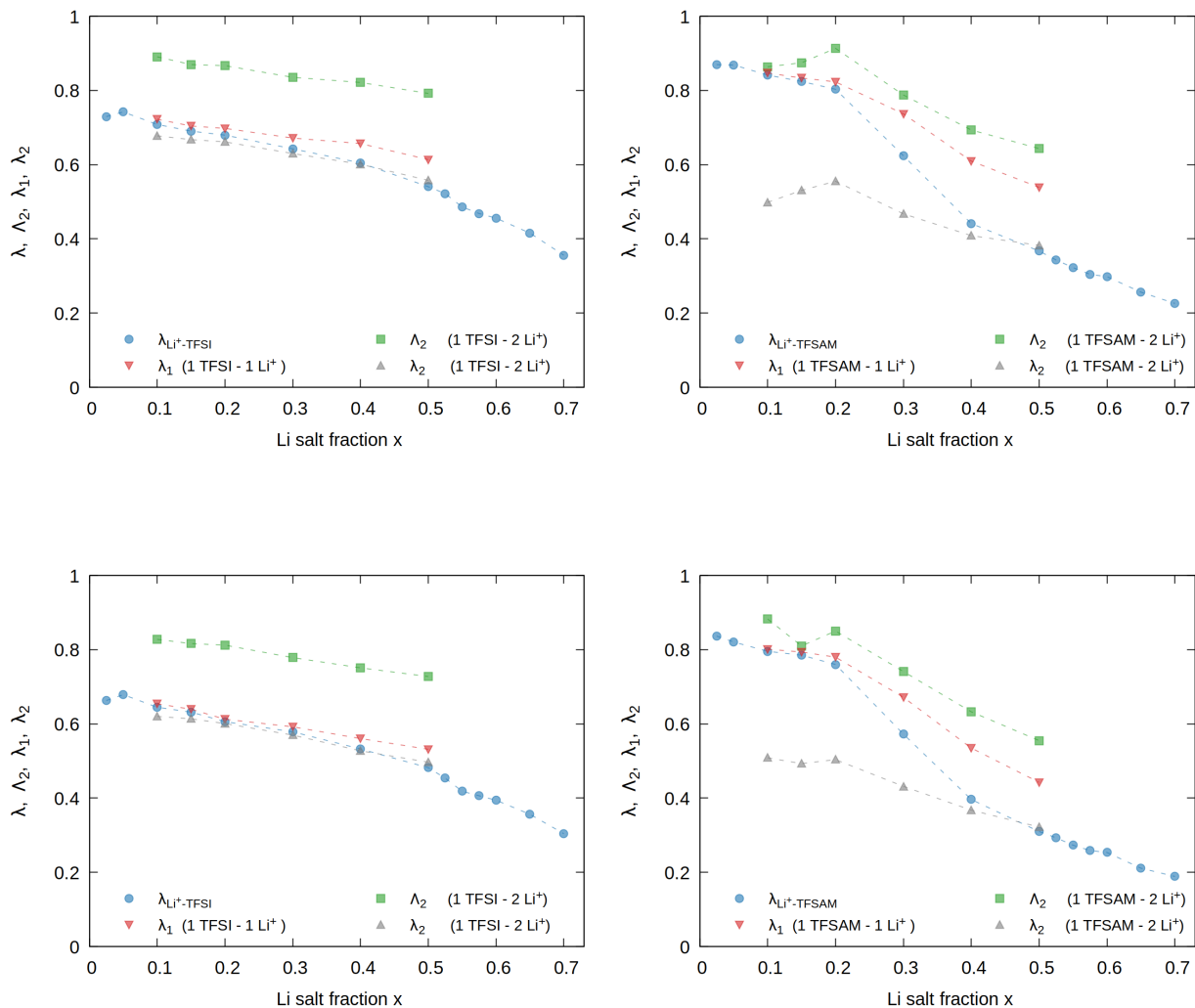


Figure S24: Comparison of lithium coupling factors (λ , λ_1 , λ_2 , Λ_2) as a function of salt content for both TFSI⁻ (left) and TFSAM⁻ (right) - based mixtures for characteristic times of $3 \cdot \tau_{Ls}$ (top) and $5 \cdot \tau_{Ls}$ (bottom).

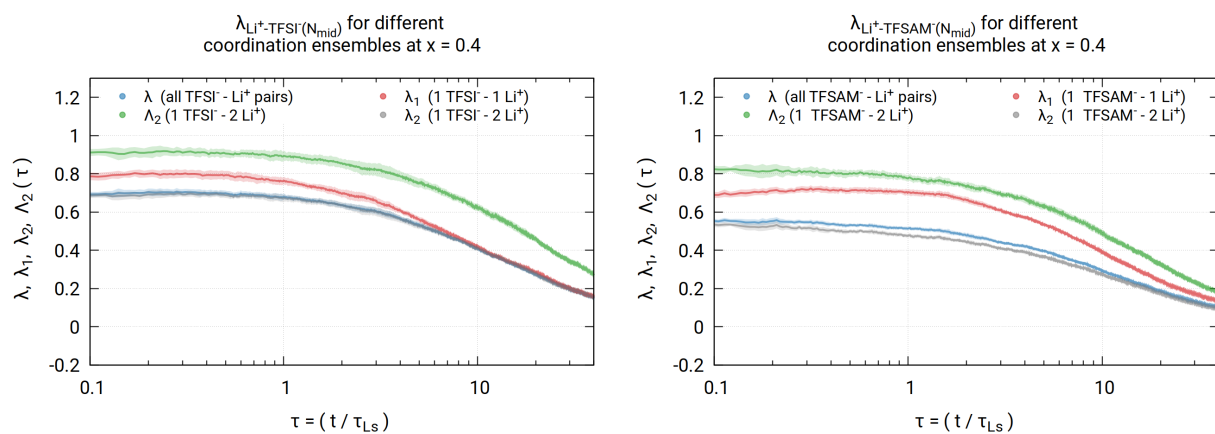


Figure S25: Time dependence of LCF λ , λ_1 , λ_2 and Λ_2 exemplary shown for the $x=0.4$ TFSI⁻- (left) and TFSAM⁻-based (right) electrolyte compositions.

N: Additional information for discussing $D_{\text{anion}}/D_{\text{Li}^+}$ as a function of salt content x

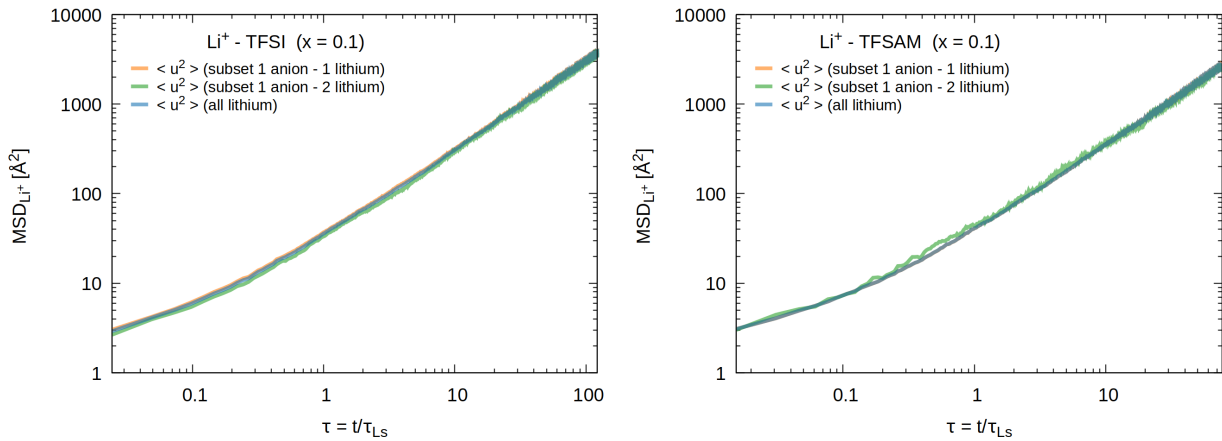
It can be easily shown that the line of argumentation for a decreasing ratio $\langle \vec{v} \rangle / \langle \vec{u} \rangle$ as a consequence of double Li^+ -anion coordination is applicable to higher Li^+ over-coordination of the anion. Assume the anion j is bound to n Li^+ and tries to couple with the strength Λ_n to the average Li^+ displacement $\vec{U}_i^j = \frac{1}{n} \cdot (\vec{u}_1 + \dots + \vec{u}_n)$:

$$\vec{v}_j = \Lambda_n \cdot \vec{U}_i^j + \vec{E}_j. \quad (12)$$

Squaring and rearranging yields for the ratio $\langle \vec{v} \rangle / \langle \vec{u} \rangle$:

$$\begin{aligned} \frac{\langle \vec{v}^2 \rangle}{\langle \vec{u}^2 \rangle} &= \Lambda_n^2 \cdot \frac{1}{n^2} \cdot \left(n + 2 \binom{n}{2} \frac{\langle \vec{u}_1 \vec{u}_2 \rangle}{\langle \vec{u} \rangle} \right) + \frac{\vec{E}^2}{\langle \vec{u} \rangle} \\ &= \Lambda_n^2 \cdot \frac{1}{n} \cdot \underbrace{\left(1 + (n-1) \frac{\langle \vec{u}_1 \vec{u}_2 \rangle}{\langle \vec{u} \rangle} \right)}_{<1} + \frac{\vec{E}^2}{\langle \vec{u} \rangle} \\ &\quad \rightarrow \frac{\langle \vec{u}_1 \vec{u}_2 \rangle}{\langle \vec{u} \rangle} \end{aligned} \quad (13)$$

If the remaining terms and factors do not change considerably, one can easily see that the ratio drops further with n -fold coordination.



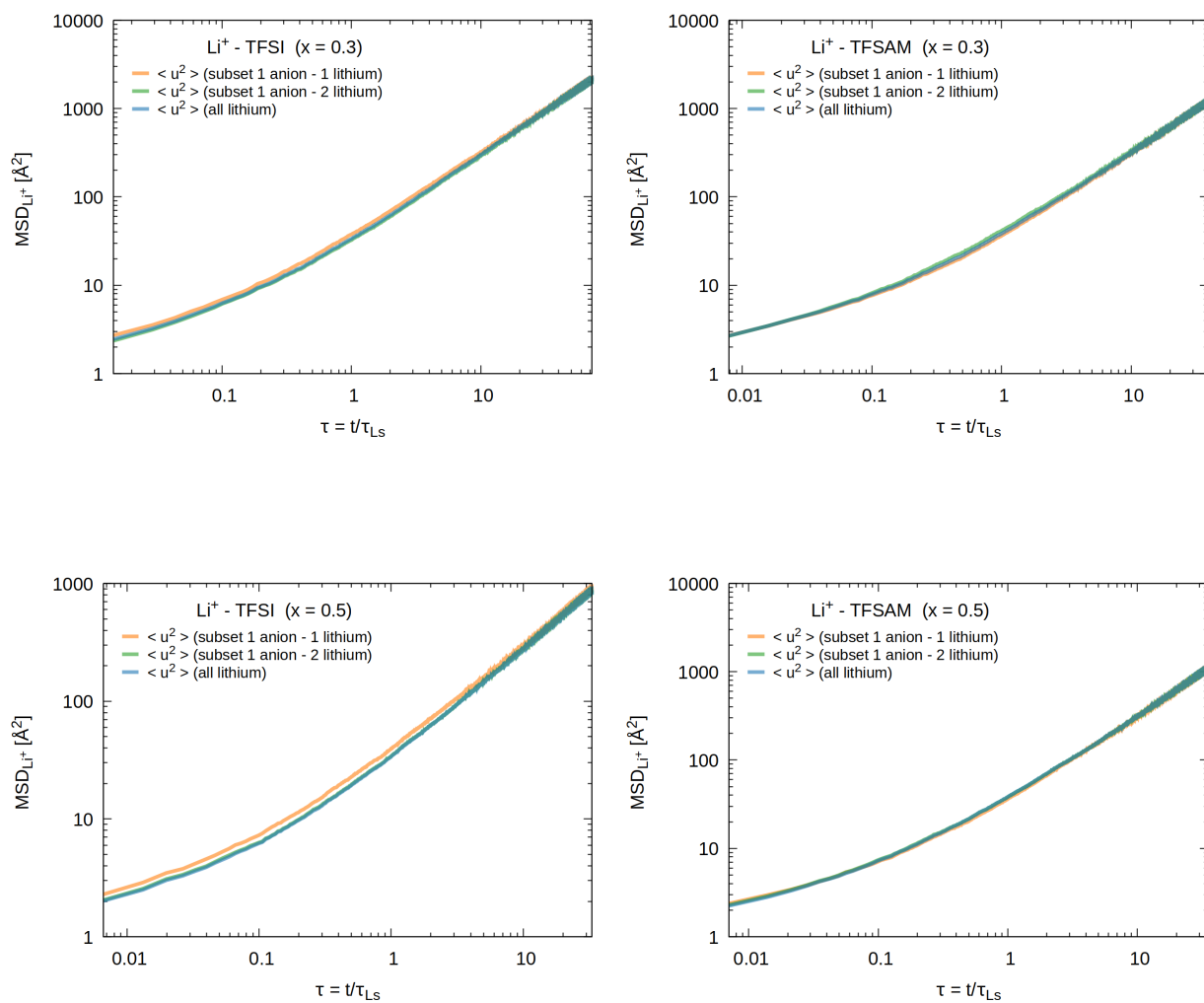


Figure S26: Comparison of lithium MSD to $\langle u^2 \rangle$ in the subensembles of λ_1 and λ_2/Λ_2 .

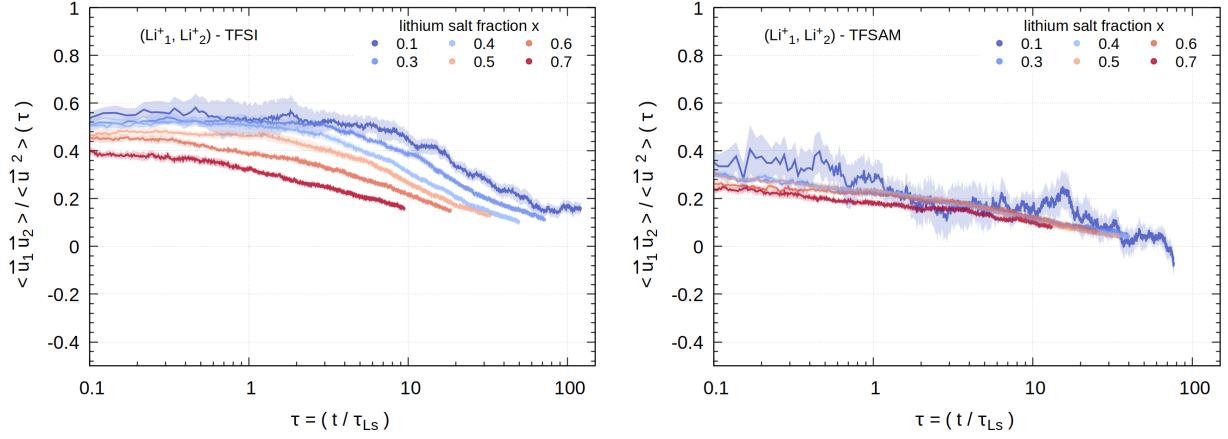


Figure S27: $\text{Li}^+ - \text{Li}^+$ - correlation $\langle \vec{u}_1 \cdot \vec{u}_2 \rangle / \langle \vec{u}^2 \rangle$ for lithium ions that are bound to the same anion at time $\tau = 0$.

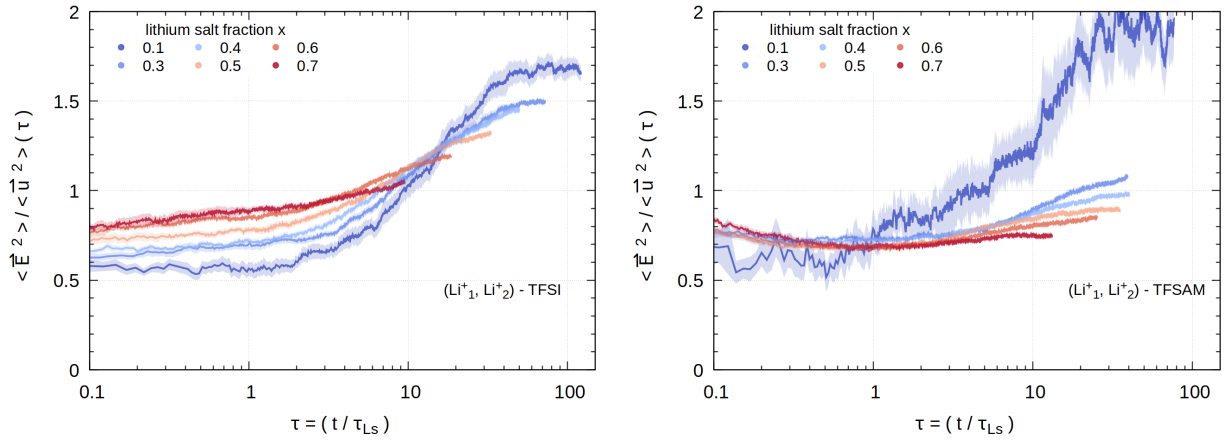


Figure S28: Random motion $\langle \vec{\mathcal{E}}^2 \rangle$ of anions, which have two Li^+ neighbours at time $\tau = 0$, scaled by the average squared lithium displacement $\langle \vec{u}^2 \rangle$. $\langle \dots \rangle$ denotes the ensemble average over the Li^+ that are involved in the double coordination of the anion at $\tau = 0$.

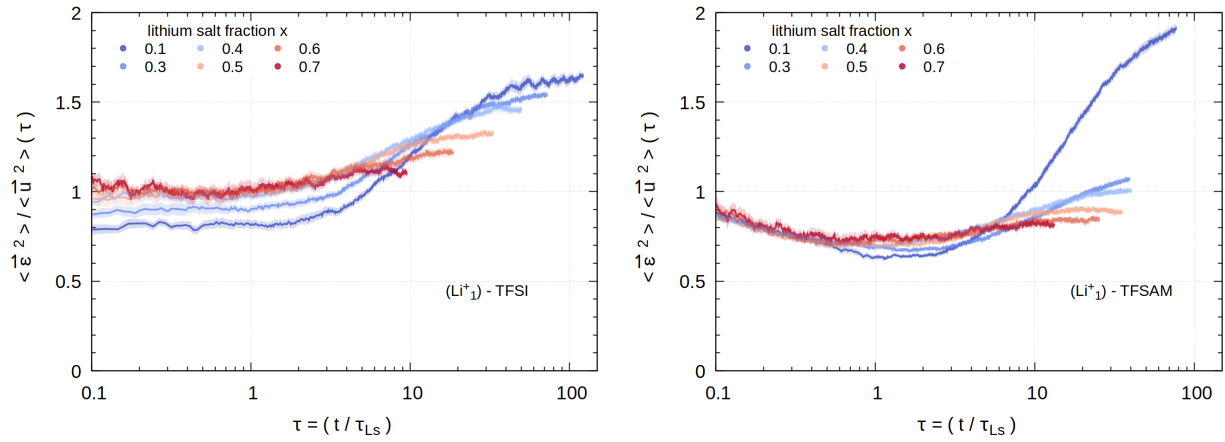


Figure S29: Random motion $\langle \vec{\epsilon}^2 \rangle$ of anions, which have only a single Li^+ neighbour at time $\tau = 0$, scaled by the average squared lithium displacement $\langle \vec{u}^2 \rangle$. $\langle \dots \rangle$ denotes the ensemble average over the Li^+ that are involved in the single coordination of the anion at $\tau = 0$.

O: Self van Hove function $G_s(r, \Delta t)$

The self van Hove function $G_s(r, \Delta t)$ describes the probability distribution that a particle has moved a distance r within a time lag Δt away from its original position:

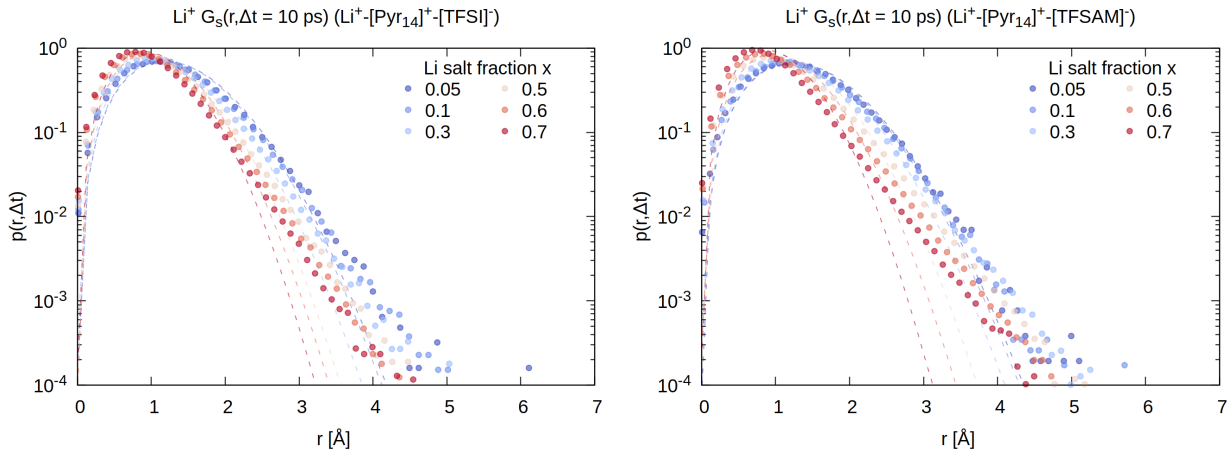
$$G_s(r, \Delta t) = \frac{1}{N} \left\langle \sum_{i=1}^N \delta(r - |\vec{r}_i(t + \Delta t) - \vec{r}_i(t)|) \right\rangle \quad (14)$$

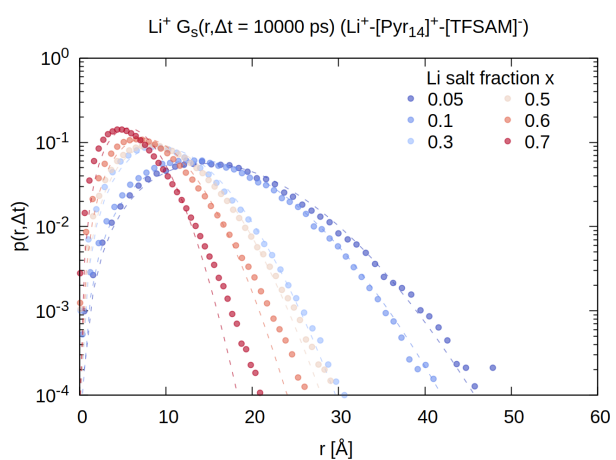
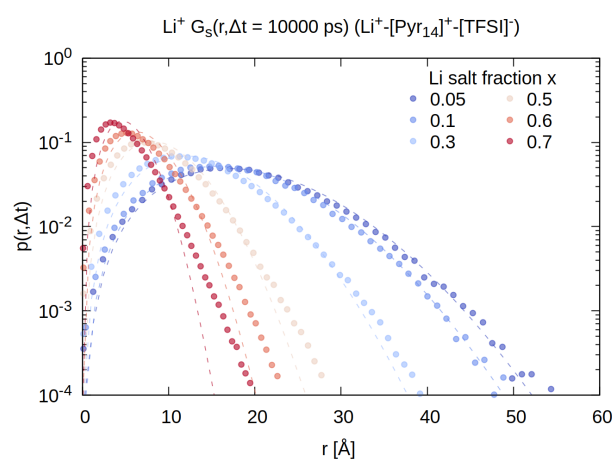
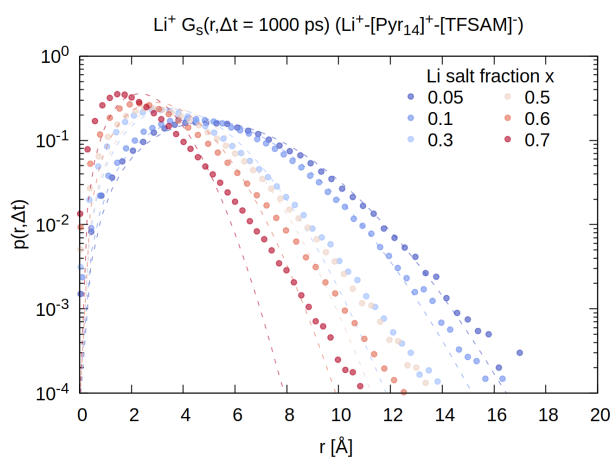
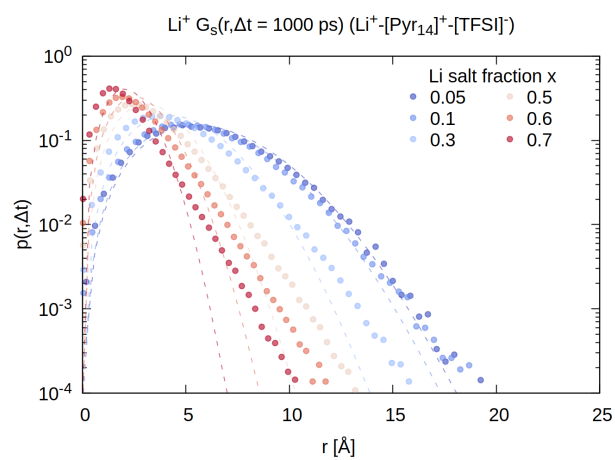
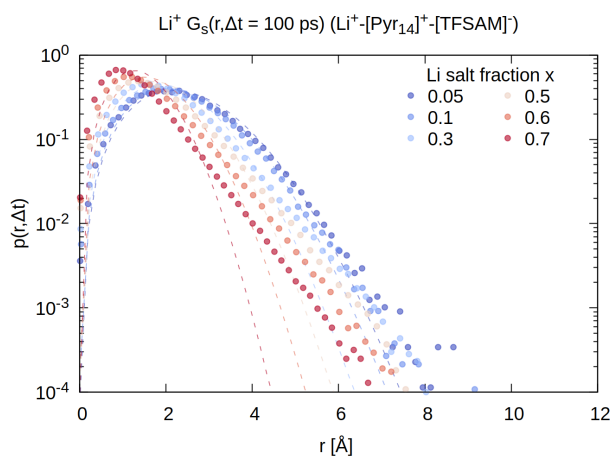
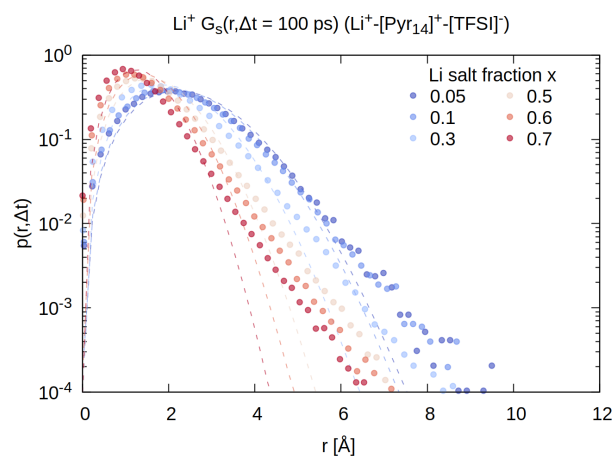
Figure S30 gives an overview of the displacement distributions $G_s(r, \Delta t)$ of the lithium ions at time lags $\Delta t = 10$ ps, 100 ps, 1 ns, 10 ns and 100 ns for the broad spectrum of lithium salt contents. The dashed lines represent the displacement distribution expected for an ideal diffusive motion that exhibits a Gaussian behavior

$G_{0,s}(r, \Delta t) = \left(\frac{3}{2\pi \cdot \langle r^2(\Delta t) \rangle} \right)^{3/2} \exp\left(-\frac{3}{2} \frac{r^2}{\langle r^2(\Delta t) \rangle}\right)$. Comparison of the probed displacement distribution $G_s(r, \Delta t)$ to $G_{0,s}(r, \Delta t)$ shows that the non-Gaussian characteristics of the lithium dynamics increase in both electrolyte series with increasing lithium salt content.

The tails of the distributions at high displacement distances r are indicative of a fraction of lithium ions that display a higher mobility.

We note that although no secondary peaks emerge in the distributions at elevated salt content, which would indicate that lithium transport is achieved through discrete "hopping" events, the pronounced tails of $G_s(r, \Delta t)$ might stem from lithium jumps.





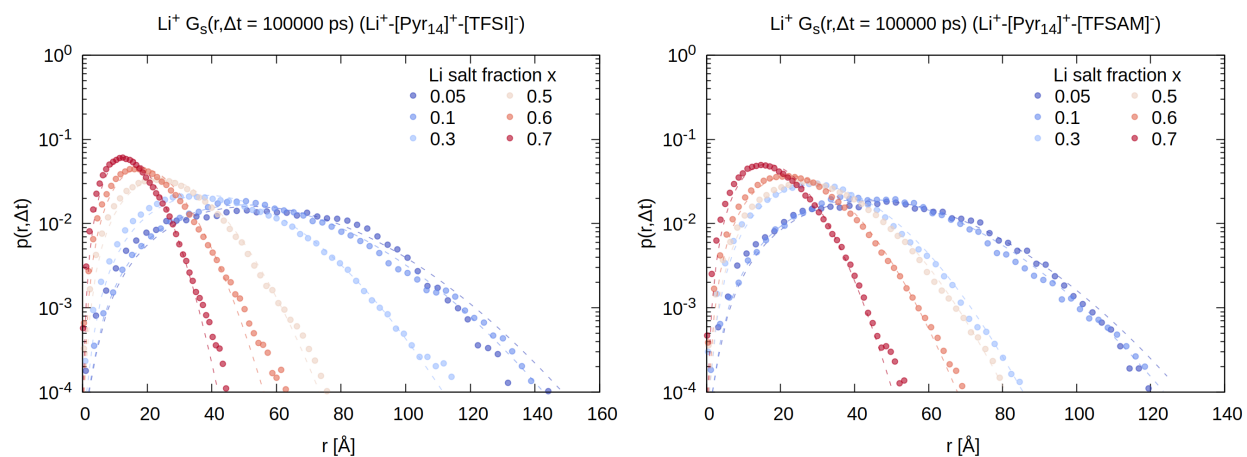


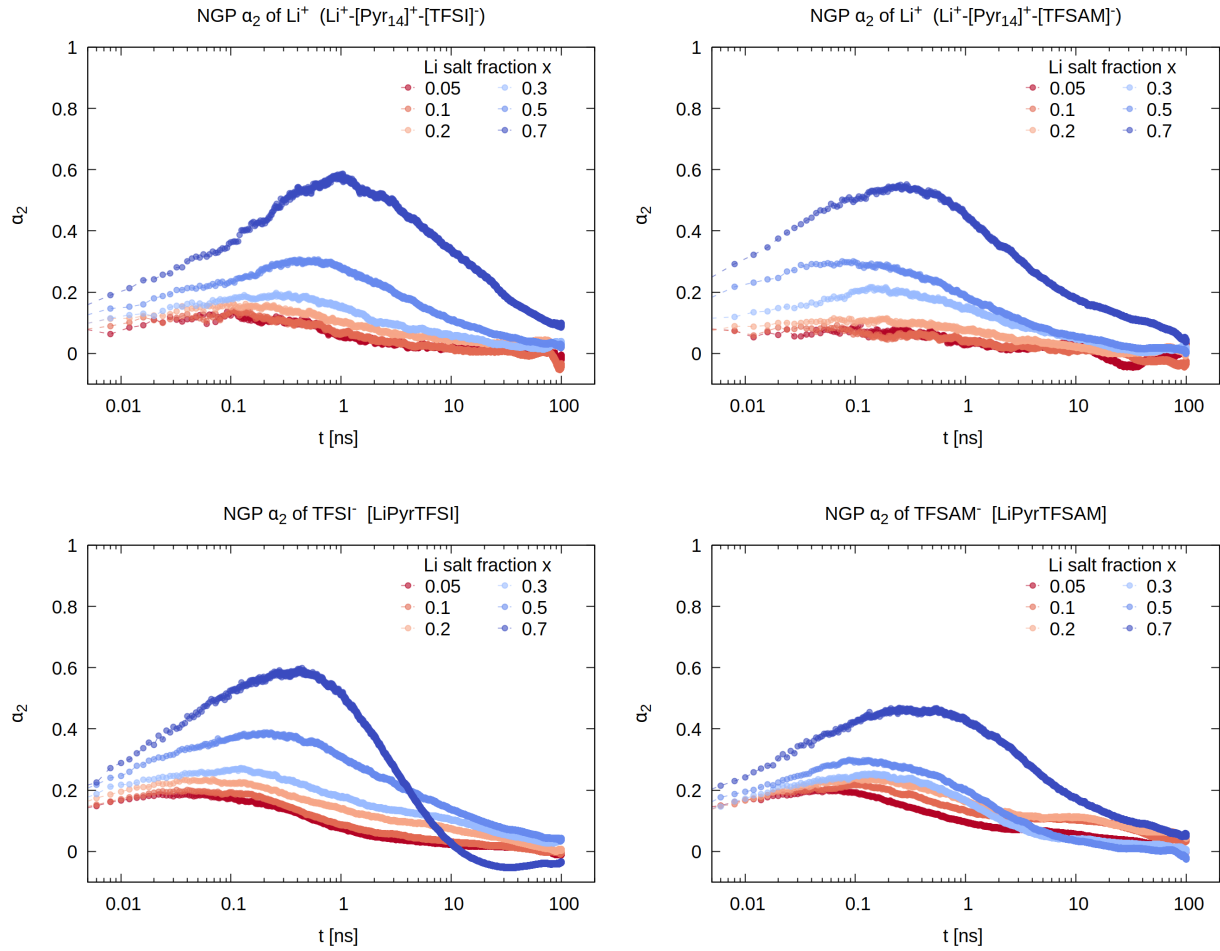
Figure S30: The self van Hove functions $G_s(r, \Delta t)$ of the lithium ions in TFSI⁻ (left) and TFSAM⁻ (right) containing electrolytes for the spectrum of investigated lithium salt concentrations x . $G_s(r, \Delta t)$ is compared to the corresponding ideal Gaussian distribution $G_{0,s}(r, \Delta t)$, which is depicted by the dashed lines.

P: Non-Gaussian parameter α_2

The non-Gaussian parameter (NGP) α_2 which probes the deviation from truly Gaussian dynamics, is extracted from the second and fourth moment of the particle displacements:

$$\alpha_2(t) = \frac{3}{5} \cdot \frac{\langle \Delta \vec{r}^4(t) \rangle}{\langle \Delta \vec{r}^2(t) \rangle^2} - 1, \quad (15)$$

where $\Delta \vec{r}(t) = (\vec{r}(t) - \vec{r}(0))$ denotes the particle displacement within the time t and the brackets $\langle .. \rangle$ indicate the ensemble average over all particles for the given time lag.



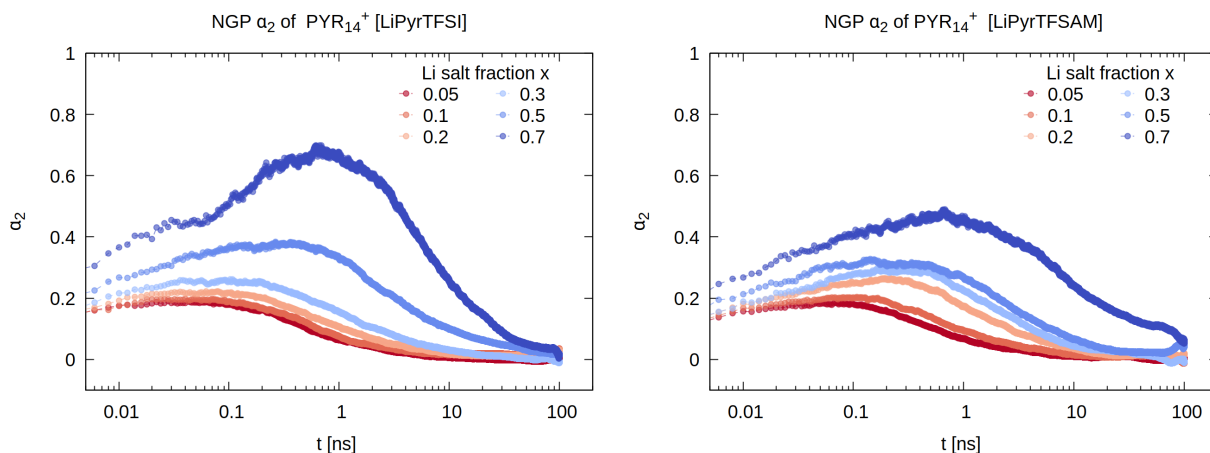


Figure S31: Non-gaussian parameters Li^+ (top), anions (middle) and Pyr_{14}^+ (bottom) dynamics in TFSI^- (left) and TFSAM^- (right) containing electrolytes for various lithium salt fractions x and averaging over 4 blocks of 100 ns duration each.

References

- (1) Van Der Spoel, D.; Lindahl, E.; Hess, B.; Groenhof, G.; Mark, A. E.; Berendsen, H. J. GROMACS: Fast, flexible, and free. *Journal of Computational Chemistry* **2005**, *26*, 1701–1718.
- (2) Páll, S.; Abraham, M. J.; Kutzner, C.; Hess, B.; Lindahl, E. Tackling Exascale Software Challenges in Molecular Dynamics Simulations with GROMACS. Solving Software Challenges for Exascale. Cham, 2015; pp 3–27.
- (3) Abraham, M. J.; Murtola, T.; Schulz, R.; Páll, S.; Smith, J. C.; Hess, B.; Lindahl, E. Gromacs: High performance molecular simulations through multi-level parallelism from laptops to supercomputers. *SoftwareX* **2015**, *1-2*, 19–25.
- (4) Berendsen, H. J.; van der Spoel, D.; van Drunen, R. GROMACS: A message-passing parallel molecular dynamics implementation. *Computer Physics Communications* **1995**, *91*, 43–56.

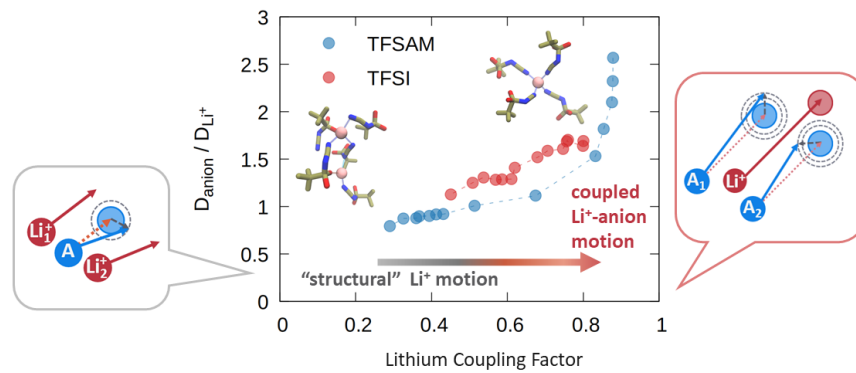
- (5) Jorgensen, W. L.; Maxwell, D. S.; Tirado-Rives, J. Development and testing of the OPLS all-atom force field on conformational energetics and properties of organic liquids. *Journal of the American Chemical Society* **1996**, *118*, 11225–11236.
- (6) Gouveia, A. S.; Bernardes, C. E.; Tomé, L. C.; Lozinskaya, E. I.; Vygodskii, Y. S.; Shaplov, A. S.; Lopes, J. N. C.; Marrucho, I. M. Ionic liquids with anions based on fluorosulfonyl derivatives: from asymmetrical substitutions to a consistent force field model. *Physical Chemistry Chemical Physics* **2017**, *19*, 29617–29624.
- (7) Canongia Lopes, J. N.; Pádua, A. A. CL&P: A generic and systematic force field for ionic liquids modeling. *Theoretical Chemistry Accounts* **2012**, *131*, 1–11.
- (8) Canongia Lopes, J. N.; Deschamps, J.; Pádua, A. A. H. Modeling Ionic Liquids Using a Systematic All-Atom Force Field. *The Journal of Physical Chemistry B* **2004**, *108*, 2038–2047.
- (9) Lopes, J. N.; Pádua, A. A. Molecular force field for ionic liquids composed of triflate or bistriflylimide anions. *Journal of Physical Chemistry B* **2004**, *108*, 16893–16898.
- (10) Shimizu, K.; Almantariotis, D.; Costa Gomes, M. F.; Pádua, A. A.; Canongia Lopes, J. N. Molecular force field for ionic liquids V: Hydroxyethylimidazolium, dimethoxy-2methylimidazolium, and fluoroalkylimidazolium cations and Bis(fluorosulfonyl)amide, perfluoroalkanesulfonylamide, and fluoroalkylfluorophosphate anions. *Journal of Physical Chemistry B* **2010**, *114*, 3592–3600.
- (11) Doherty, B.; Zhong, X.; Gathiaka, S.; Li, B.; Acevedo, O. Revisiting OPLS force field parameters for ionic liquid simulations. *Journal of chemical theory and computation* **2017**, *13*, 6131–6145.
- (12) Bhargava, B. L.; Balasubramanian, S. Refined potential model for atomistic simulations of ionic liquid [bmim][PF6]. *The Journal of Chemical Physics* **2007**, *127*, 114510.

- (13) Chaban, V. V.; Voroshylova, I. V.; Kalugin, O. N. A new force field model for the simulation of transport properties of imidazolium-based ionic liquids. *Physical Chemistry Chemical Physics* **2011**, *13*, 7910.
- (14) Self, J.; Fong, K. D.; Persson, K. A. Transport in superconcentrated LiPF₆ and LiBF₄/propylene carbonate electrolytes. *ACS Energy Letters* **2019**, *4*, 2843–2849.
- (15) Fong, K. D.; Self, J.; Diederichsen, K. M.; Wood, B. M.; McCloskey, B. D.; Persson, K. A. Ion transport and the true transference number in nonaqueous polyelectrolyte solutions for lithium ion batteries. *ACS central science* **2019**, *5*, 1250–1260.
- (16) Molinari, N.; Mailoa, J. P.; Craig, N.; Christensen, J.; Kozinsky, B. Transport anomalies emerging from strong correlation in ionic liquid electrolytes. *Journal of Power Sources* **2019**, *428*, 27–36.
- (17) Molinari, N.; Mailoa, J. P.; Kozinsky, B. General trend of a negative Li effective charge in ionic liquid electrolytes. *The journal of physical chemistry letters* **2019**, *10*, 2313–2319.
- (18) Molinari, N.; Kozinsky, B. Chelation-Induced Reversal of Negative Cation Transference Number in Ionic Liquid Electrolytes. *The Journal of Physical Chemistry B* **2020**, *124*, 2676–2684.
- (19) Huang, Q.; Lourenço, T. C.; Costa, L. T.; Zhang, Y.; Maginn, E. J.; Gurkan, B. Solvation Structure and Dynamics of Li⁺ in Ternary Ionic Liquid–Lithium Salt Electrolytes. *The Journal of Physical Chemistry B* **2018**, *123*, 516–527.
- (20) Thum, A.; Heuer, A.; Shimizu, K.; Lopes, J. N. C. Solvate ionic liquids based on lithium bis (trifluoromethanesulfonyl) imide–glyme systems: coordination in MD simulations with scaled charges. *Physical Chemistry Chemical Physics* **2020**, *22*, 525–535.

- (21) Lemkul, J. A.; Huang, J.; Roux, B.; MacKerell Jr, A. D. An empirical polarizable force field based on the classical drude oscillator model: development history and recent applications. *Chemical reviews* **2016**, *116*, 4983–5013.
- (22) Salomon-Ferrer, R.; Case, D. A.; Walker, R. C. An overview of the Amber biomolecular simulation package. *Wiley Interdisciplinary Reviews: Computational Molecular Science* **2013**, *3*, 198–210.
- (23) Li, Z.; Bouchal, R.; Mendez-Morales, T.; Rollet, A.-L.; Rizzi, C.; Le Vot, S.; Favier, F.; Rotenberg, B.; Borodin, O.; Fontaine, O. Transport Properties of Li-TFSI Water-in-Salt Electrolytes. *The Journal of Physical Chemistry B* **2019**, *123*, 10514–10521.
- (24) Nürnberg, P.; Lozinskaya, E. I.; Shaplov, A. S.; Schönhoff, M. Li Coordination of a Novel Asymmetric Anion in Ionic Liquid-in-Li Salt Electrolytes. *The Journal of Physical Chemistry B* **2020**, *124*, 861–870.
- (25) Martinez, L.; Andrade, R.; Birgin, E. G.; Martínez, J. M. PACKMOL: A package for building initial configurations for molecular dynamics simulations. *Journal of Computational Chemistry* **2009**, *30*, 2157–2164.
- (26) Berendsen, H. J. C.; Postma, J. P. M.; van Gunsteren, W. F.; DiNola, A.; Haak, J. R. Molecular dynamics with coupling to an external bath. *The Journal of Chemical Physics* **1984**, *81*, 3684–3690.
- (27) Bussi, G.; Donadio, D.; Parrinello, M. Canonical sampling through velocity rescaling. *The Journal of Chemical Physics* **2007**, *126*, 014101.
- (28) Parrinello, M.; Rahman, A. Polymorphic transitions in single crystals: A new molecular dynamics method. *Journal of Applied Physics* **1981**, *52*, 7182–7190.
- (29) Nosé, S.; Klein, M. Constant pressure molecular dynamics for molecular systems. *Molecular Physics* **1983**, *50*, 1055–1076.

- (30) Nosé, S. A molecular dynamics method for simulations in the canonical ensemble. *Molecular Physics* **1984**, *52*, 255–268.
- (31) Hoover, W. G. Canonical dynamics: Equilibrium phase-space distributions. *Physical Review A* **1985**, *31*, 1695–1697.
- (32) Hess, B.; Bekker, H.; Berendsen, H. J. C.; Fraaije, J. G. E. M. LINCS: A linear constraint solver for molecular simulations. *Journal of Computational Chemistry* **1997**, *18*, 1463–1472.
- (33) Hess, B. P LINCS:A Parallel Linear Constraint Solver for Molecular Simulation. **2007**,
- (34) Michaud-Agrawal, N.; Denning, E. J.; Woolf, T. B.; Beckstein, O. MDAAnalysis: a toolkit for the analysis of molecular dynamics simulations. *Journal of computational chemistry* **2011**, *32*, 2319–2327.
- (35) Gowers, R. J.; Linke, M.; Barnoud, J.; Reddy, T. J. E.; Melo, M. N.; Seyler, S. L.; Domanski, J.; Dotson, D. L.; Buchoux, S.; Kenney, I. M. *MDAnalysis: a Python package for the rapid analysis of molecular dynamics simulations*; 2019.
- (36) Zhang, Z.; Nasrabadi, A. T.; Aryal, D.; Ganesan, V. Mechanisms of Ion Transport in Lithium Salt-Doped Polymeric Ionic Liquid Electrolytes. *Macromolecules* **2020**, *53*, 6995–7008.

TOC graphic:



Increased information content of the LCF λ compared to $D_{\text{anion}}/D_{\text{Li}^+}$ and subsequently derived Li^+ transport principles in ionic liquid electrolytes.